

Enhanced thermoelectric performance of Half Heusler and Silicon Germanium via
nanostructuring

Di Wu

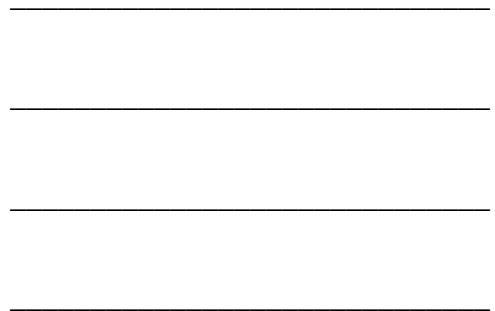
B.S., University of Science and Technology of China, P.R.China

A Dissertation presented to the Graduate Faculty
of the University of Virginia in Candidacy for the Degree of
Doctor of Philosophy

Department of Physics

University of Virginia

August 2013



Abstract

Nanostructured Half Heusler alloys $MNiSn$, $MCoSb$ ($M=Hf, Zr$ and Ti) and $SiGe$ nanocomposites were synthesized with high energy vibrational ball mill, followed by spark plasma sintering (SPS) consolidation. The thermoelectric properties were measured from room temperature to 1100K, the dependence of thermoelectric properties on consolidation parameters and microstructures were investigated. A differential effective medium (DEM) model was also developed to evaluate the lattice thermal conductivity in heterogeneous two-phase systems.

In the case of N-type $Hf_{0.75}Zr_{0.25}NiSn$ Half Heusler alloys, 0.25%, 0.5% and 1% V were doped into Hf site; up to 40% thermopower enhancements were observed from 300K to 600K, meanwhile, no obviously change of electrical conductivities were detected, indicating that the enhancement of thermopower came from localized density of states (DOS) enhancement at the Fermi level. The enhancement of thermopower was discussed within Mott expression and this conclusion was further supported by low temperature specific heat measurements, which clearly showed the DOS at the Fermi level was increased by 88% after 1% V was doped into Hf site. Nanostructuring technique was also performed to achieve better ZT performance. N-type $Hf_{0.6}Zr_{0.4}NiSn_{0.995}Sb_{0.005}$ nanocomposites were synthesized via mechanical alloys and SPS consolidation, thermopower got enhanced and lattice thermal conductivity was suppressed, compared with the corresponding bulk form; furthermore, 10% Hf atoms being replaced by Ti atoms was proved to further reduce the lattice thermal conductivity, eventually

leading to a dimensionless figure of merit ZT as high as 1.0 at 823K. Second-phase ZrO_2 nanoparticles being introduced into P-type $Hf_{0.3}Zr_{0.7}CoSn_{0.3}Sb_{0.7}$ matrix was also proved to effectively increase photon scattering intensity and result in an enhanced figure of merit $ZT=0.85$ at 1050K.

In the case of SiGe nanocomposites, the dependence of thermoelectric properties on SPS consolidation parameters was investigated, it was concluded that sufficient sintering temperature and holding time were necessary to obtain nonporous nanocomposites. It was also found that severe grain growth took place during SPS consolidation, probably due to the relatively small mismatching potentials at the boundaries of coherent nanocrystals. Second-phase nanoinclusions and core-shell structures were proved to effectively impede the grain growth; moreover, the incoherent interfaces introduced by nanoinclusions also increased phonon scattering intensity and brought energy filtering effect, resulting in reduction in lattice thermal conductivity and enhancement in thermopower. $ZT\sim 1.2$ at 1123K was achieved in nanostructured N-type $Si_{80}Ge_{20}P_2$, while $ZT\sim 0.75$ at 1123K was achieved in P-type counterpart $Si_{80}Ge_{20}P_2$.

At the end, to evaluate the lattice thermal conductivity in a heterogeneous two-phase system, the differential effective medium (DEM) model was developed based on conventional average T-matrix approximation (ATA). The advantage of DEM over ATA is that DEM not only expands the applicability of effective medium approach from small volume fractions to the whole range of volume fraction from 0 to 1, but also inherently includes the multiple scattering which dominates at high volume fractions but wasn't well considered in ATA with single particle scattering approximation. A revised effective scattering cross section, together with the grain size dispersion, demonstrated a further reduction in lattice thermal conductivity.

Table of contents

Abstract.....	II
Table of contents.....	IV
List of figures.....	VIII
List of tables.....	XIII
1. Background of thermoelectricity.....	1
1-1. Discovery of thermoelectric effects.....	1
1-2. Figure of merit ZT and efficiency of thermoelectrics.....	8
1-3. Semiconductors as optimal thermoelectric materials.....	14
1-4. State-of-the-art TE materials.....	17
1-5. Motivation.....	22
2. Sample synthesis and characterization.....	25
2-1. Sample synthesis.....	25
2-1-1. Arc melting.....	25
2-1-2. Annealing.....	26
2-1-3. Introduction melting.....	27
2-1-4. Solid state reaction.....	27

2-1-5. Melting spinning.....	29
2-1-6. Ball milling.....	30
2-1-7. Spark plasma sintering.....	31
2-1-8. Sample preparation for SEM.....	33
2-1-9. Sample preparation for TEM.....	34
2-2. Sample characterization.....	35
2-2-1. X-Ray Diffraction.....	35
2-2-2. Atomic Force Microscopy.....	36
2-2-3. “homemade” high temperature probe.....	37
2-2-4. ZEM-3.....	40
2-2-5. Thermal conductivity.....	41
2-2-6. Hall effect.....	43
3. Thermoelectric properties improvement on Half Heusler alloys via nanostructuring	45
3-1. Introduction of Half Heusler (HH).....	46
3-2. Resonant states.....	48
3-2-1. Background.....	48
3-2-2. Experiments.....	50
3-2-3. Discussion.....	52
3-2-4. Conclusions of resonant states.....	58
3-3. Nanostructuring.....	59
3-3-1. Exploring for proper ball mill vessel.....	60
3-4. Efforts on thermopower enhancement via energy filtering.....	62
3-4-1. Monolithic N-type HH nanocomposite.....	66
3-4-2. Nanoparticles embedded P-type bulk HH.....	71
3-5. Reduction on thermal conductivity.....	77

3-5-1. Monolithic nanocomposite.....	78
3-5-2. Nanoparticles embedded in bulk.....	79
3-6. Mass fluctuation effect on lattice thermal conductivity.....	81
3-7. Conclusions.....	84
4. Nanostructured Silicon Germanide as prospective thermoelectrics.....	86
4-1. Sample synthesis.....	87
4-2. Grain size vs. BM time.....	88
4-3. Porosity vs. sintering temperature.....	89
4-4. Grain growth in SPS consolidation process.....	91
4-5. Heterogeneous nanophase.....	97
4-6. Core-shell structure.....	102
4-7. Conclusions and future work.....	111
5. Effective Medium Theory (EMT).....	113
5-1. Average T-matrix Approximation (ATA) and Coherent Potential Approximation (CPA)	114
5-1-1 ATA.....	114
5-1-2 CPA.....	116
5-2. Differential Effective Medium (DEM) approach.....	117
5-3. Comparison of DEM and ATA.....	120
5-4. DEM with inherently implemented multiple scattering.....	127
5-5. Effective scattering cross-section.....	135
5-5-1. Scattering cross-section.....	136
5-5-2. Grain size dispersion.....	138
5-5-3. Validation of effective scattering cross section treatment in DEM.....	141
5-5-4. Comparison with PbS-PbSe nanocomposite.....	143

5-5-5. Prediction on ZrNi ₂ Sn/ZrNiSn Full Heusler-Half Heusler nanocomposite.....	146
5-5-6. Conclusions.....	148
5-6. Summary and future work of DEM approach.....	149
6. Conclusions.....	151
7. Acknowledgements.....	154
Reference.....	155

List of figures

Figure 1-1 The Seebeck effect.....	2
Figure 1-2 The Peltier effect.....	3
Figure 1-3 The Thomson effect.....	6
Figure 1-4 A typical thermoelectric module.....	8
Figure 1-5 The dependence of normalized efficiency of TE engine on figure of merit ZT ...13	
Figure 1-6 The dependence of TE properties on carrier concentrations.....	15
Figure 1-7 State-of-the-art N-type bulk TE materials	18
Figure 1-8 State-of-the-art P-type bulk TE materials	18
Figure 1-9 A typical energy path in gasoline fueled internal combustion engine vehicle.....	23
Figure 2-1 A schematic “homemade” high temperature thermoelectric probe	37
Figure 2-2 ZEM-3 system made by ULVAC-RIKO Inc.....	40
Figure 3-1 Crystal structure of $MNiSn$ ($M=Hf, Zr, Ti$) Half Heusler.....	46
Figure 3-2 Localized resonant states over a narrow energy range E_R at Fermi level.....	49
Figure 3-3 (a) Powder XRD scan (b) SEM image of surface micrograph and (c) EDS line scan of $(Hf_{0.75}Zr_{0.25})_{0.99}V_{0.01}NiSn$ along the yellow arrow in (b).....	51
Figure 3-4 Thermopower in the range of (a) 300K to 1100K (b) 300K to 700K, and (c) electrical resistivity (d) power factor for V doped HH $(Hf_{0.75}Zr_{0.25})_{1-x}V_xNiSn$, with $x=0\%$ (open square), 0.24% (gray circle), 0.63% (gray triangle) and 0.78% (black pentagon).....	52
Figure 3-5 Plots of $2k_B \ln(\rho)$ vs. $1/T$, with slopes representing width of band gaps. From top to bottom, the plots are: 0.63% (dark grey triangle), 0.24% (light grey circle), 0.78% (black pentagon) and 0% (open square) V- doped $Hf_{0.75}Zr_{0.25}NiSn$ separately.....	53

- Figure 3-6 The dependence of carrier concentration n , carrier mobility μ , Seebeck coefficient S and carrier effective mass m^* on V doping level in intrinsic $\text{Hf}_{0.75}\text{Zr}_{0.25}\text{NiSn}$ alloys.....56
- Figure 3-7 The dependence of heat capacity C_p on temperature at temperatures ranging from 1.8K to 5.0K in V doped $\text{Hf}_{0.75}\text{Zr}_{0.25}\text{NiSn}$ alloys, the inset shows that dependence of the Seebeck coefficient at room temperature and density of state at the Fermi level on V doping level.58
- Figure 3-8 X-Ray Diffraction patterns of as-cast Half Heusler $\text{Hf}_{0.6}\text{Zr}_{0.4}\text{NiSn}_{0.995}\text{Sb}_{0.005}$ (black) and corresponding powders that were ball milled in normal iron vial set (blue) and that in ZrO_2 vial set (red) respectively.....62
- Figure 3-9 The preferential scattering mechanism of charge carriers in conduction band through grain boundary of barrier height ϵ_b 65
- Figure 3-10 X-Ray Diffraction patterns of (a) N-type $\text{Hf}_{0.6}\text{Zr}_{0.4}\text{NiSn}_{1-x}\text{Sb}_x$ ($x=0.005, 0.02$) and (b) P-type $\text{Hf}_{0.3}\text{Zr}_{0.7}\text{CoSn}_{0.3}\text{Sb}_{0.7}$ with ZrO_2 impurities.....67
- Figure 3-11 (a)(b) SEM scanning, (c)(d) TEM scanning and (e) Selected Area Diffraction pattern on 15hrs Ball Milled N-type $\text{Hf}_{0.6}\text{Zr}_{0.4}\text{NiSn}_{0.995}\text{Sb}_{0.005}$ alloy.....68
- Figure 3-12 Measured electrical resistivity ($\text{Ohm}\cdot\text{m}$) and thermopower S (V/K) of N-type Half Heusler $\text{Hf}_{0.6}\text{Zr}_{0.4}\text{NiSn}_{0.995}\text{Sb}_{0.005}$ which was SPS at 1000°C after 15 hours' BM (red square), the comparison with its analogue composite without BM was presented in black square.....70
- Figure 3-13 Power factor S^2T/ρ dependent on temperature in monolithic nanostructured $\text{Hf}_{0.6}\text{Zr}_{0.4}\text{NiSn}_{0.995}\text{Sb}_{0.005}$70
- Figure 3-14 (a) Microstructure of P-type HH $\text{Hf}_{0.3}\text{Zr}_{0.7}\text{CoSn}_{0.3}\text{Sb}_{0.7}$ under TEM, and selected area diffraction as well as EDS at (b) grain area B (c) matrix area E.....73
- Figure 3-15 (a)(b) SEM scanning of fractured P-type $\text{Hf}_{0.3}\text{Zr}_{0.7}\text{CoSn}_{0.3}\text{Sb}_{0.7}$, and (c) Energy Dispersive Spectroscopy line scan across the path shown in (b).....74
- Figure 3-16 (a) Thermopower S ($\mu\text{V}/\text{K}$) and (b) Electrical resistivity ρ ($\mu\Omega\cdot\text{cm}$) of P-type $\text{Hf}_{0.3}\text{Zr}_{0.7}\text{CoSn}_{0.3}\text{Sb}_{0.7}$ with 0% (black square), 1% (blue triangle) and 2% (red star) ZrO_2 nanoparticles.....75
- Figure 3-17 Seebeck coefficient and electrical resistivity of nominal 1%, 2% and 4% ZrO_2 dispersed P-type HH $\text{Hf}_{0.3}\text{Zr}_{0.7}\text{CoSn}_{0.3}\text{Sb}_{0.7}$76
- Figure 3-18 (a) Total thermal conductivity (solid lines) and lattice thermal conductivity (solid squares) (b) figure of merit ZT of N-type HH $\text{Hf}_{0.6}\text{Zr}_{0.4}\text{NiSn}_{0.995}\text{Sb}_{0.005}$ with 0hr (black), 10hrs (blue) and 15hrs (red) Ball Milling time79

Figure 3-19 Lattice thermal conductivity of P-type HH $\text{Hf}_{0.3}\text{Zr}_{0.7}\text{CoSn}_{0.3}\text{Sb}_{0.7}$ bulk (grey) and corresponding nanocomposites with 1% (blue), 2% (black) and 4% (red) ZrO_2 nanoparticles.	80
Figure 3-20 The dependence of figure of merit ZT on temperature in 1%, 2% and 4% ZrO_2 dispersed $\text{Hf}_{0.3}\text{Zr}_{0.7}\text{CoSn}_{0.3}\text{Sb}_{0.7}$.	81
Figure 3-21 Lattice thermal conductivity of $\text{Hf}_{0.6}\text{Zr}_{0.4}\text{NiSn}_{0.995}\text{Sb}_{0.005}$ with 0%, 10%, and 20% Hf atoms replaced by smaller Ti atoms.	83
Figure 3-22 Figure of merit ZT achieved of Half Heusler alloys (a) N-type: ZT=1.0 at 850K in monolithic $\text{Ti}_{0.1}\text{Hf}_{0.5}\text{Zr}_{0.4}\text{NiSn}_{0.995}\text{Sb}_{0.005}$ (b) P-type: ZT=0.85 at 1050K in 2% ZrO_2 nanoparticles dispersed $\text{Hf}_{0.3}\text{Zr}_{0.7}\text{CoSn}_{0.3}\text{Sb}_{0.7}$.	85
Figure 4-1 TEM images of nanoscaled aggregates under different magnifications for $\text{Si}_{80}\text{Ge}_{20}\text{P}_2$ ball milled 5 hours.	89
Figure 4-2 TEM images of nanoscale aggregates under different magnifications for $\text{Si}_{80}\text{Ge}_{20}\text{P}_2$ ball milled 15 hours.	89
Figure 4-3 Electrical resistivity (a), Seebeck coefficient (b) and Power Factor (c) of $\text{Si}_{80}\text{Ge}_{20}\text{P}_2$ sintered at 900 °C, 1000 °C and 1100 °C separately.	91
Figure 4-4 XRD pattern of SGP-T1-05 and SGP-T1-15, the inset shows corresponding peaks at (111).	92
Figure 4-5 Lattice thermal conductivity of SGP-T1-05 and SGP-T1-15.	93
Figure 4-6 XRD pattern of $\text{Si}_{80}\text{Ge}_{20}\text{P}_2$ nanopowders (black) after 15 hours BM and its solidified bulk (blue) analogue, the inset provides enlarge comparison of diffraction peaks at (111).	94
Figure 4-7 Grains of SPS consolidated $\text{Si}_{80}\text{Ge}_{20}\text{P}_2$ with 5 hours BM time under JOEL 2000FX showing the huge majority grains in (a)(b), and HRTEM Titan showing the existence of small minority grains in (c)(d).	95
Figure 4-8 Comparison of lattice thermal conductivity and ZT between our samples with significant grain growth (black squares) and Boston College without grain growth (black curve)	96
Figure 4-9 $\text{Si}_{80}\text{Ge}_{20}\text{P}_2$ nanocomposites with 15 hours ball mill time examined under JEOL 2000FX.	97
Figure 4-10 TEM image of Ytria Stabilized Zirconia (YSZ) nanopowders.	98

Figure 4-11 TEM images of SPS condensed $\text{Si}_{80}\text{Ge}_{20}\text{P}_2$ nanocomposites (BM for 5hours) with 0% YSZ (a)(b), 5% YSZ (c)(d) and 10%YSZ (e)(f) nanoparticles.....	99
Figure 4-12 EDS scanning over light smaller and dense light grains for 5% YSZ dispersed $\text{Si}_{80}\text{Ge}_{20}\text{P}_2$, indicating the fact that light grains are YSZ, dense grains $\text{Si}_{80}\text{Ge}_{20}\text{P}_2$	101
Figure 4-13 Thermal conductivity, power factor and figure of merit of 0%, 2%, 5% and 10% YSZ nanoparticles dispersed $\text{Si}_{80}\text{Ge}_{20}\text{P}_2$	102
Figure 4-14 A enlarged band gap E_g of a quantum dot due to size effect, compared with its bulk counterpart and single molecule with LUMO-HOMO gap.....	104
Figure 4-15 Core-shell structures of 3 different types classified by the relative position of conduction and valence band of the core and the shell, with blue and red blocks represent core and shell band structures individually.....	105
Figure 4-16 (a)The Type I CdSe/CdS core/shell structure and (b) the Type II CdSe/CdTe core-shell structure.....	106
Figure 4-17 The pseudo core (red circle)/shell (green circle) structure of $\text{Si}_{80}\text{Ge}_{20}\text{B}_{1.7}/\text{YSZ}$ nanocomposite.....	107
Figure 4-18 Comparison of thermoelectric properties for $\text{Si}_{80}\text{Ge}_{20}\text{B}_{1.7}/\text{SiO}_2$ (blue square) and $\text{Si}_{80}\text{Ge}_{20}\text{B}_{1.7}/\text{TiO}_2$ (red square) core-shell structures with sole $\text{Si}_{80}\text{Ge}_{20}\text{B}_{1.7}$ nanocomposite (black square).....	108
Figure 4-19 Conduction and valence band edges alignment of SiGe core and $\text{SiO}_2/\text{TiO}_2/\text{YSZ}$ shell.....	109
Figure 4-20 Figure of merit ZT in $\text{Si}_{80}\text{Ge}_{20}\text{B}_{1.7}/\text{SiO}_2$ and $\text{Si}_{80}\text{Ge}_{20}\text{B}_{1.7}/\text{TiO}_2$	110
Figure 5-1 Configuration of adding $d\phi$ of second phase in DEM regime.....	118
Figure 5-2 Dependence of lattice thermal conductivity κ_{ph} in YSZ/ CoSb_3 nanoparticle/matrix system on volume fraction ϕ at 300K, with DEM (solid lines) and ATA (dash lines) calculations; the grain size of YSZ nanoparticles are set to be 50, 20, 20, 5 nm separately.....	123
Figure 5-3 Dependence of lattice thermal conductivity κ_{ph} in $\text{CoSb}_3/\text{CoSb}_3$ nanoparticle/matrix system on volume fraction ϕ at 300K, with DEM (solid lines) and ATA (dash lines) calculations; the grain size of YSZ nanoparticles are set to be 50, 20, 20, 5 nm separately.....	124

Figure 5-4 Lattice thermal conductivity dependence on interface density Φ , in YSZ/CoSb₃ nanocomposite, for grain size is equal to 50,20,10 and 5 nm separately.....126

Figure 5-5 Independent-particle scattering in low volume fractions vs. multiple scattering in high volume fractions.....127

Figure 5-6 Comparison between multiple scattering and independent-particle scattering $3\phi/2$129

Figure 5-7 DEM Calculated lattice thermal conductivity $k^*(\phi)$ DEM with $F(\phi)$ in Eqn (5-16)-multiple scattering and $F(\phi)=3\phi/2$ -independent particle scattering in core-shell structure of Si/ZrO₂ at grain size $d=50, 20, 10$ and 5 nm.....132

Figure 5-8 DEM Calculated lattice thermal conductivity $k^*(\phi)$ DEM with $F(\phi)$ in Eqn (5-16)-multiple scattering and $F(\phi)=3\phi/2$ -independent particle scattering in core-shell structure of Si₈₀Ge₂₀/YSZ at grain size $d=50, 20, 10$ and 5 nm.....133

Figure 5-9 Lattice thermal conductivity κ_{ph} of Si/Ge nanocomposite dependence on Si nanoparticles' volume fraction ϕ at 300K, with an average grain size of $d_0=10$ nm. DEM simulations with different grain size dispersions (blue-fixed grain size $d=d_0$, green-standard deviation of $0.289d_0$ and red-standard deviation of $0.577d_0$) are compared with Nan's EMA (triangles), Minnich's EMA (black solid line) and Jeng's MC simulation (asterisks).....143

Figure 5-10 Lattice thermal conductivity κ_{ph} of PbS/PbSe nanocomposite dependence on PbS nanoparticles' volume fraction ϕ at 300K, the comparisons are performed among experimental data (black asterisks), KD theory for solid solutions (black line) and DEM simulations with grain size distribution function $F_5(x)$ (red line).....145

Figure 5-11 Figure 5-11 Dependence of lattice thermal conductivity κ_{ph} of ZrNi₂Sn/ZrNiSn nanocomposite on ZrNi₂Sn nano phase's volume fraction ϕ at 300K. Two series of plots are presented corresponding to average grain size $d_0=5$ nm and 10 nm individually, DEM simulations for different grain size dispersions are distinguished by colors (blue-fixed grain size, green-standard deviation of $0.289d_0$ and red-standard deviation of $0.577d_0$).....147

List of tables

Table 1-1 Thermoelectric properties of nanostructured materials at optimal operation temperatures, values in the parentheses correspond to their normal bulk types.....	19
Table 3-1 Thermoelectric properties of V-doped $\text{Hf}_{0.75}\text{Zr}_{0.25}\text{NiSn}$	55
Table 5-1 The parameters used in nanocomposite calculations for DEM and ATA.....	122
Table 5-2 Parameter used in the core-shell systems of Si/ZrO_2 and $\text{Si}_{80}\text{Ge}_{20}/\text{YSZ}$, at $T = 1100\text{K}$	131
Table 5-3 Spherical nanoparticles size dispersion functions dependence effective scattering cross section for $\text{ErAs}/\text{In}_{0.53}\text{Ga}_{0.47}\text{As}$ nanocomposite with $d_0=10\text{nm}$	139
Table 5-4 - Parameters of different composites used in this work, at room temperature $T=300\text{K}$	142

1. Background of thermoelectricity

Thermoelectricity is a bidirectional process that can be understood as follows: the temperature difference across a piece of material produces a potential difference or, vice versa, an electrical potential difference applied on the material produces a temperature difference. The materials capable of conducting heat-electricity energy conversion are thus named thermoelectric materials or thermoelectrics. Thermoelectric materials can be utilized to build thermoelectric generators or thermoelectric coolers, depending on whether the process is heat-electricity conversion or the reverse.

1-1 Discovery of thermoelectric effects

In 1821, Thomas Johann Seebeck reported some experiments to the Prussian Academy of Science that showed he had made the first observations of thermoelectric effects. He had produced potential differences by heating the junctions between dissimilar conductors, as shown in Figure 1-1. In spite of the fact that he didn't fully understand the meaning of his results, Seebeck was able to arrange his conductors in more or less the same thermoelectric series that is recognized today.

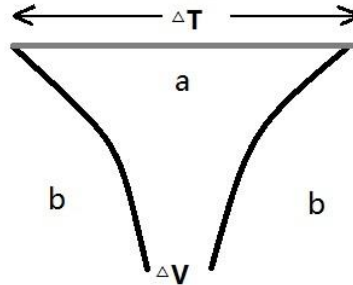


Figure 1-1 The Seebeck effect.

Thirteen years later, in 1834, Jean Charles Athanase Peltier, a French watchmaker, published some results that showed that he had discovered a second thermoelectric effect. Specifically, when a current was passed through a junction between two different conductors, heat was absorbed or generated depending on the direction of the current, as shown as Figure 1-2. This effect is superimposed upon, but quite distinct from, the Joule resistance, heating effect of which usually associates with the passage of an electric current. Like Seebeck, Peltier did not understand the true significance of his result. Independently, in 1838, Lenz demonstrated that water could be frozen at a Bi-Sb junction by the passage of a current; when the current was reversed, the ice could be melted.

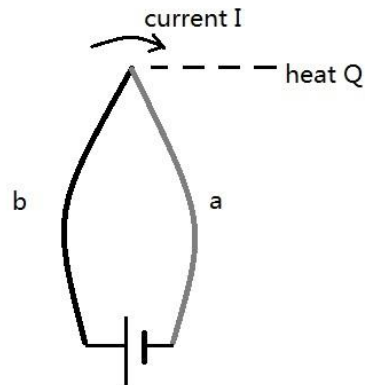


Figure 1-2 The Peltier effect.

As we now know, the Seebeck effect can be explained in terms of charge-carrier diffusion: an applied temperature gradient causes an overall charge carrier diffusion from the hot side to the cold side, and the net current flow (if any) leads to a voltage gradient across hot and cold endings. This can be described in a simple formula:

$$S_{ab} = -\frac{\Delta V_{ab}}{\Delta T_{ab}} \text{ or } V_{ab} = \int_{T_a}^{T_b} (S_b - S_a) dT \quad (1-1)$$

Where ΔV , ΔT are the electric potential and temperature difference across the junction, and S (Seebeck coefficient or thermopower) measures the magnitude of the induced thermoelectric voltage in response to a temperature difference across that material or the entropy per charge carrier in the material.[1]

Accordingly, the Peltier effect can be formulated as:

$$\dot{Q} = \pi_{ab}I = (\pi_b - \pi_a)I \quad (1-2)$$

Where π_{ab} is the Peltier coefficient for the thermocouple composed of materials a and b, I is the current flow in this Peltier circuit, and \dot{Q} is the rate of heat dissipation or absorption (depending on the direction of current flow) at the junction. The Peltier coefficient represents how much heat the current is carrying per unit charge through a given material. Since the current must be continuous across a junction, the associated heat flow will develop a discontinuity if π_a and π_b are different. Depending on the direction of the current, heat must accumulate or dissipate at the junction due to a non-zero divergence that occurs there; this divergence is physically due to the carriers attempting to return to the equilibrium before the current was applied by transferring energy from one connector to another.

It is necessary to distinguish the Peltier effect from Joule heating, which is known to be caused by interactions between moving charge carriers and atomic ions that make up the body of a conductor. Charged carriers in an electric circuit are accelerated by an electric field but give up some of their kinetic energies due to inelastic collisions with ions; in turn, the energy gained by these ions manifests as vibration and leads to an increase in the temperature in the conductor. Joule heating is described by Joule's first law, $\dot{Q} = I^2R$. Due to its quadratic dependence on current I, Joule heating always behaves in the form of heat dissipation, unlike the Peltier effect, which depends on I linearly and can dissipate or absorb heat depending on the direction of the current flow.

After analyzing both the Seebeck and the Peltier effect, Lord Kelvin realized that a relation should exist between them; thus, he proceeded to derive this relation from thermodynamic arguments. This led him to the conclusion that a third thermoelectric effect must exist. This effect, now called the Thomson effect, is a heating or cooling effect in a homogeneous conductor when an electric current passes in the direction of a temperature gradient (Figure 1-3). The Thomson coefficient γ is defined by:

$$\gamma = \lim_{\Delta T \rightarrow 0} \frac{\Delta \dot{Q}}{I \Delta T} \quad (1-3)$$

When a current with density J is passing through a homogeneous conductor, the heat production per unit volume is as follows:

$$\dot{Q} = \rho J^2 - \gamma J \frac{dT}{dl} \quad (1-4)$$

Where ρ is the electrical resistivity, and $\frac{dT}{dl}$ is the temperature gradient along the conductor. The first term represents nothing but Joule heating, while the second term refers to Thomson heating, which can change sign if the direction of J is reversed.

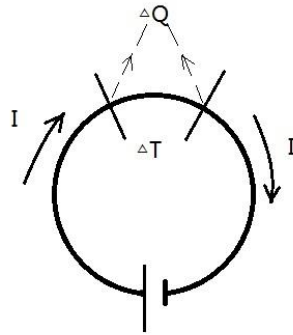


Figure 1-3 The Thomson Effect.

From the aspect of energy conservation, the heat generated must be equal to the electrical energy consumed. If J is sufficiently small, Joule heating which quadratically depends on J can be ignored. In light of all three thermoelectric effects, the Kelvin relations can be derived as follows:[2]

$$S = \frac{\pi}{T} \quad (1-5)$$

$$\frac{dS}{dT} = \frac{\gamma}{T} \quad (1-6)$$

Kelvin relations not only tie the three thermoelectric phenomena together, but also have other useful applications. For instance, absolute Seebeck coefficient can be calculated by integration over T in Eqn (1-6), provided Thomson heat is measurable:

$$S(T) - S(0) = \int_0^T \frac{\gamma}{T} dT \quad (1-7)$$

Where $S(0)=0$, representing the zero Seebeck coefficient at absolute zero temperature according to the third law of thermodynamics.[3] Alternately, one can calculate S by comparing with a known superconductor whose S is also equal to 0,[4] or with any material with a well-known Seebeck coefficient. A more rigorous approach to derive Kelvin relations can be conducted based on modern solid state physics.[2], [5]

Despite the fact that thermoelectric effects have been known for such a long time, until recently the only devices based upon them and widely employed are thermocouples for temperature measurement and thermopiles for radiant energy detection; both applications utilize the Seebeck effect (i.e., energy conversion from heat to electricity). The basic theories of thermoelectric generators and refrigerators were first derived by Altenkirch as early as in 1909[6] and 1911[7] respectively. He showed that, for both applications, materials were required to be of high Seebeck coefficients, high electrical conductivities to minimize Joule heating, and low thermal conductivities to reduce heat loss during transportation. However, simply knowing the favorable properties was quite a different matter from obtaining materials embodying them; thus, as long as metallic thermocouples were employed, no real progress had actually been made for a long time. Thermoelectric generators and refrigerators with reasonable efficiencies have become possible only since semiconductors have been adopted; the advantage of semiconductors over metals will be discussed later in chapter 1-3.

1-2 Figure of merit ZT and efficiency of thermoelectrics

As mentioned in chapter 1-1, thermoelectric effects can be utilized for both electricity generation and refrigeration. Presented here is a general method to evaluate the energy conversion efficiency of a thermoelectric module. Figure 1-4 shows a thermocouple composed of two branches/legs (N and P types) of thermoelectric pieces; one end of the thermocouple is attached to a high temperature sink (T_h) while the other end is attached to a low temperature sink (T_c); the cross-sections of the N- and P- type legs are A_n and A_p , respectively, and the length in z direction is referred as L in both legs without losing generality.

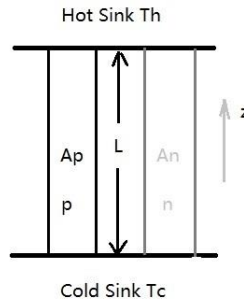


Figure 1-4 A typical thermoelectric module.

The rate of heat generation/dissipation across each branch is the sum of the Peltier heating in Eqn (1-2) and the heat conduction term due to temperature gradient dT/dz , explicitly expressed as:

$$\begin{cases} \dot{Q}_p = \pi_p I - \lambda_p A_p \frac{dT}{dz} \\ \dot{Q}_n = \pi_n I - \lambda_n A_n \frac{dT}{dz} \end{cases} \quad (1-8)$$

With Kelvin relation Eqn (1-5), Eqn (1-8) can then be rewritten as:

$$\begin{cases} \dot{Q}_p = S_p T I - \lambda_p A_p \frac{dT}{dz} \\ \dot{Q}_n = S_n T I - \lambda_n A_n \frac{dT}{dz} \end{cases} \quad (1-9)$$

Where λ_p and λ_n represent corresponding thermal conductivities for P and N type branches respectively. Since current I flows all the way through the module, the Joule heating cannot be neglected; actually half of the overall Joule heating finds its way to each N-P junction. Here, taking the cold end for instance, the rate of cooling is composed of the Peltier cooling in both N-type and P-type legs as in Eqn (1-9), as well as the halved total Joule heating at N-P junction. This can be explicitly stated as:

$$\dot{Q}_c = (\dot{Q}_p + \dot{Q}_n)|_c - \frac{1}{2} I^2 R \quad (1-10)$$

Where \dot{Q}_p and \dot{Q}_n can be substituted with Eqn (1-9), with boundary condition $T(z=0)=T_c$, $T(z=L)=T_h$, Eqn (1-10) can be rewritten as:

$$\dot{Q}_c = (S_p - S_n) T_c I - K(T_h - T_c) - \frac{1}{2} I^2 R \quad (1-11)$$

Where thermal conductance and electrical resistance are:

$$\begin{cases} K = \frac{\lambda_p A_p}{L} + \frac{\lambda_n A_n}{L} \\ R = \frac{L}{A_p \sigma_p} + \frac{L}{A_n \sigma_n} \end{cases} \quad (1-12)$$

Thus far, the effective power used to cool the cold sink has been calculated; what follows will be the total power supplied. Through the whole circuit, part of the potential difference applied to the module is employed in overcoming the electrical resistances, while the rest is used to balance the Seebeck voltage resulting from the temperature difference between the junctions. Thus, the external power supplied W shall be:

$$W = (S_p - S_n)(T_h - T_c)I + I^2 R \quad (1-13)$$

Based on Eqn (1-11) and Eqn (1-13), the efficiency of this module shall be:

$$\eta = \frac{\dot{Q}_c}{W} = \frac{(S_p - S_n)T_c I - \left(\frac{\lambda_p A_p}{L} + \frac{\lambda_n A_n}{L}\right)(T_h - T_c) - \frac{1}{2}I^2 R}{(S_p - S_n)(T_h - T_c)I + I^2 R} \quad (1-14)$$

The efficiency η as shown depends on the thermoelectric and geometric properties of the two legs, the temperature difference between two sinks, and the current flow I . As argued by Altenkirch,[6] η reaches a maximal value when the dimensions of the two legs satisfy the following rule:

$$\frac{A_p}{A_n} = \left(\frac{\sigma_p \lambda_p}{\sigma_n \lambda_n}\right)^{\frac{1}{2}} \quad (1-15)$$

Then:

$$\eta = \frac{\dot{Q}_c}{W} = \frac{S_{pn}T_c(IR) - \left(\left(\frac{\lambda_p}{\sigma_p}\right)^{1/2} + \left(\frac{\lambda_n}{\sigma_n}\right)^{1/2}\right)^2 (T_h - T_c) - \frac{1}{2}(IR)^2}{S_{pn}(T_h - T_c)IR + (IR)^2} \quad (1-16)$$

At this point, it is time to find the optimal IR to maximize efficiency η . IR depends on the electrical resistance ratio of external loads and the two legs. Letting $\frac{\partial \eta}{\partial (IR)} = 0$, one can find:

$$(IR)_{opt} = \frac{S_{pn}(T_h - T_c)}{\sqrt{1 + ZT_M - 1}} \quad (1-17)$$

Where $T_M = (T_h + T_c)/2$, and

$$Z = \frac{S_{pn}^2}{\left(\left(\frac{\lambda_p}{\sigma_p}\right)^{1/2} + \left(\frac{\lambda_n}{\sigma_n}\right)^{1/2}\right)^2} \quad (1-18)$$

Z refers to the figure of merit for a certain material or a thermoelectric junction. It should be noted that, when referring to a thermoelectric material other than a thermocouple or junction, the figure of merit Z can be rewritten as:

$$Z = \frac{S^2 \sigma}{\lambda} \quad (1-19)$$

Where the thermal conductivity λ consists of electrical (λ_e) and phonon (lattice) contribution (λ_l). In most materials, electrical contribution λ_e is directly related to the electrical resistivity according to the Wiedemann-Franz relation:

$$\lambda_e = L_0 \sigma T \quad (1-20)$$

L_0 is the Lorentz number, which is approximately $2.45 \times 10^{-8} \text{ W}\Omega/\text{K}^2$ for metals and degenerated semiconductors. Meanwhile, the lattice part is:

$$\lambda_l \approx \frac{1}{3} C v_s l_{ph} \quad (1-21)$$

C is the specific heat, v_s is the sound velocity and l_{ph} is the phonon mean free path. Above Debye temperature, both C and v_s are approximately independent of temperature.

Figure of merit Z depends on three parameters – S , σ and λ , all of which are dependent on temperature and interrelated; thus, it is difficult to optimize all three parameters simultaneously to reach a maximal Z . In the following chapters, trials of decoupling the interrelation will be introduced as effective means to improve Z .

Finally, substitute $(IR)_{opt}$ into Eqn (1-16), the relationship between device efficiency η and figure of merit Z can then be reached:[8]

$$\eta = \frac{T_h}{T_h - T_c} \frac{\sqrt{1 + ZT_M} - 1}{\sqrt{1 + ZT_M} + \frac{T_c}{T_h}} \quad (1-22)$$

It is clear that the efficiency η is simply a multiplication of ideal Carnot engine efficiency by a Z dependent factor (<1); as Z approaches infinity, η draws near to the performance of the ideal thermodynamic machine.

Presented in Figure 1-5 is the dependence of normalized efficiency η_{TE}/η_{Carnot} of an TE engine on dimensionless figure of merit ZT ; not until ZT reaches 3.0~4.0 can the TE engine perform around 50% as efficiently as the Carnot Engine, which is the typical efficiency of a conventional engine widely used nowadays. In all of the state-of-the-art TE materials known so far, only the ZT of PbTe series [9][10][11] and Bi_2Te_3 series [12][13] have been reported to be above 1.5, resulting an approximately 35% normalized efficiency.

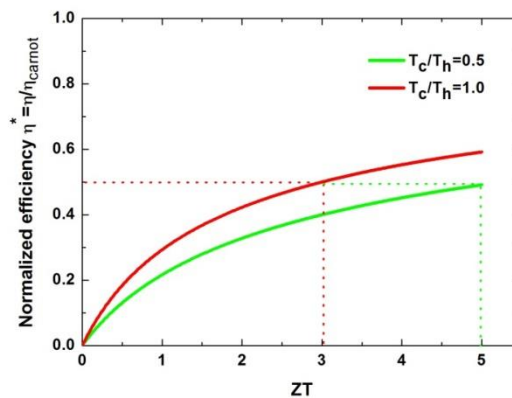


Figure 1-5 The dependence of normalized efficiency of TE engine on figure of merit ZT .

1-3 Semiconductors as optimal thermoelectric materials

As discussed in last section, the efficiency of a TE device is determined mainly by the figure of merit Z , which is defined as $S^2\sigma/\lambda$; hence, an ideal TE material would possess the properties of high Seebeck coefficient, high electrical conductivity, and low thermal conductivity in the temperature range of interest. However, these optimal conditions cannot all be met simultaneously, as the enhancement of one property will always contradict one or both of the others' benefits. Metals, for example, have half full conduction bands, no band gaps between conduction and valence bands; these features make metals ideal charge conductors; unfortunately, metals are also good heat conductors with tremendous thermal conductivity λ . In addition, in a typical metal, there is no obvious difference in concentration or mobility between N-type electrons and P-type holes; thus, the heat difference induced currents by N and P type carriers contradict each other, leading to a very low Seebeck coefficient if any. On the contrary, undoped semiconductors and insulators have ideal high Seebeck coefficients and low heat conductivity; however, they are really poor electrical conductors, due to their extremely low carrier concentrations. As shown in Figure 1-6, the best TE materials are semiconductors doped to certain carrier concentrations, typically $10^{19}\sim 10^{21}/\text{cm}^3$ [14], depending on the operating temperature.

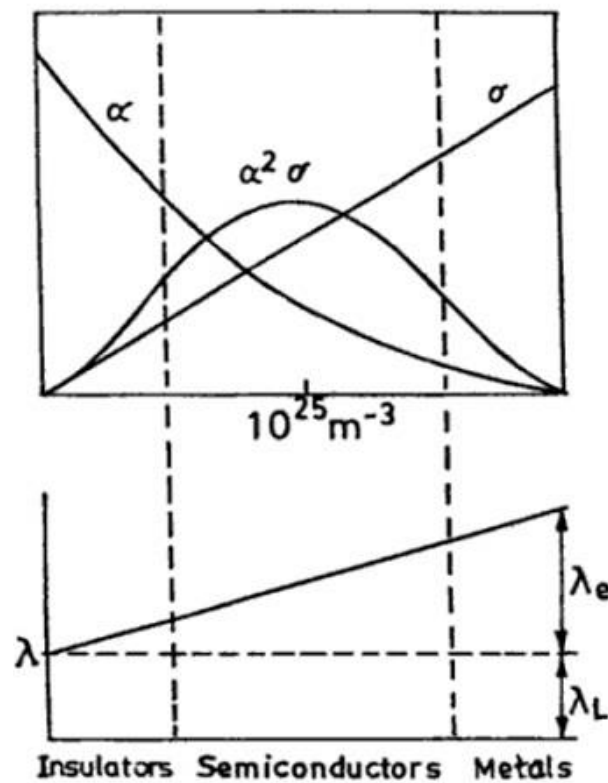


Figure 1-6 The dependence of TE properties on carrier concentrations.

For most semiconductors that are not heavily doped, the carrier concentrations are not high enough to form highly degenerated energy states; at this point, it is convenient to treat them in a non-degenerate regime with the single band approximation.[15] Also, it should be noted that most good TE materials are not metallic, rendering it reasonable for us to consider only the majority carrier, either N-type electron or P-type hole, without worrying about dipolar effects.

Within the single band model, the Seebeck coefficient of a non-degenerate semiconductor is:[15]

$$S = \pm \frac{k_B}{e} \left[\eta - \left(r + \frac{5}{2} \right) \right] \quad (1-23)$$

Where $\eta = E_F/k_B T$ is the reduced Fermi energy, and r represents carriers' scattering mechanism which is defined as:

$$\tau_e = \tau_0 E^r \quad (1-24)$$

Here, τ_e is the energy dependent relaxation time, τ_0 is the carrier's relaxation time in complete acoustic lattice scattering case, and E is the carrier energy. The most important scattering in typical semiconductors are ionized impurity scattering with $r=2$ and acoustic lattice scattering with $r=0$.

Assuming the electrical thermal conductivity $\lambda_e \ll \lambda_l$ (the lattice thermal conductivity) in a broad-band semiconductor, the optimal figure of merit Z can be reached [14] when carrier concentration satisfies:

$$n_{opt} = N(E_F) E^r \quad (1-25)$$

Where $N(E_F)$ is carrier's density of state at Fermi level E_F .

To evaluate the optimal carrier concentration in non-degenerate semiconductors, some simplified calculations can be performed: (1) Assuming the carrier's effective mass $m^* \approx m_e$, corresponding to acoustic lattice scattering with $r=0$ at $T=300\text{K}$, Eqn (1-25) yields $n_{opt} \sim 3 \times 10^{19}/\text{cm}^3$; while for ionized impurity scattering with $r=2$, Eqn (1-25) yields $n_{opt} \sim 2 \times 10^{20}/\text{cm}^3$ at the same temperature. (2) At a higher

temperature (e.g., 1273K), however, $N(E_F)$ varies with temperature as $\sim T^{1.5}$, acoustic lattice scattering with $r=0$ gives $n_{\text{opt}} \sim 2 \times 10^{20}/\text{cm}^3$,³ and ionized impurity scattering with $r=2$ gives $n_{\text{opt}} \sim 2 \times 10^{21}/\text{cm}^3$. Although the prerequisite of non-degenerate assumption is no longer satisfied at such high carrier concentrations, the calculations above still provides a simple and straightforward idea what magnitudes of carrier concentrations are needed to optimize ZT.

The non-degenerate treatment is based on classical free electron theory, which assumes the free electron gas distributes around the lattice ions and follows the Maxwell-Boltzmann statistics. This theory has been successfully applied to explain Ohm's law and have obtained the right order of the magnitude in electrical resistivity. Nevertheless, the failure for this non-degenerate model to explain electrical thermal conductivity and other transport properties eventually leads to the development of degenerate Fermi-Dirac statistics, yielding a dimensionless parameter β , which increases monotonically with ZT :[16]

$$ZT \propto \beta = 8.952 \times 10^{-6} \left(\frac{\mu}{\kappa_l}\right) \left(\frac{T}{300}\right)^{\frac{5}{2}} (m^*)^{\frac{3}{2}} \quad (1-26)$$

Where μ is carrier mobility, κ_l the lattice thermal conductivity, m^* carrier's effective mass. The dependence of ZT on μ , κ_l and m^* strongly suggests materials like “phonon-glass electron-crystal” (low lattice thermal conductivity κ_l , high carrier mobility μ) as ideal TE materials.

1-4 State-of- the-art TE materials

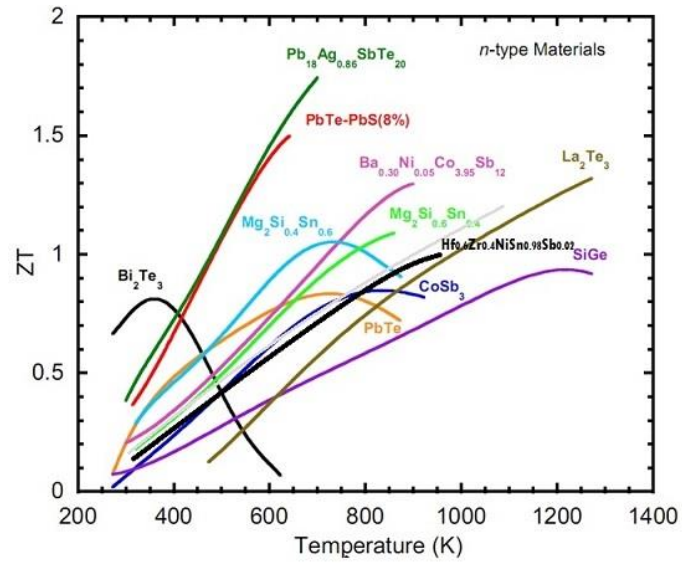


Figure 1-7 State-of-the-art N-type thermoelectric materials.

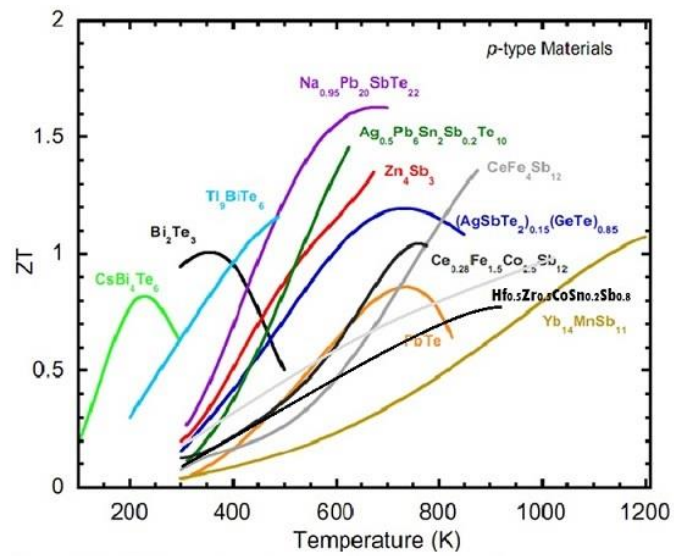


Figure 1-8 State-of-the-art P-type thermoelectric materials.

In Figure 1-7 and Figure 1-8, the dimensionless figure of merit ZT of both N-type and P-type state-of-the-art bulk thermoelectric materials are presented. To fabricate thermoelectric devices, different TE materials are utilized at different operating temperatures in order to achieve decent energy conversion performance over a wide temperature range.

In the past decade, nanostructure engineering has been introduced to fabricate TE materials and has then become one of most effective methods to enhance the TE properties. Many traditional state-of-the-art TE materials with nanostructured features have been reported to achieve significant ZT improvements in comparison with their bulk forms.[12], [17], [18] Nanostructures introduced into bulk TE materials not only serve as phonon-particle scattering centers but are also capable of inducing the so-called energy filtering effect,[19][20] both of which help to decouple the firmly interrelated thermal and electrical transport properties, eventually making it possible to suppress the lattice thermal conductivity and enhance the power factor ($PF=S^2/\rho$) simultaneously. Table 1-1 shows direct comparisons of ZT and thermal conductivities between nanostructured TE materials and their traditional bulk counterparts.

Table 1-1 Thermoelectric properties of nanostructured materials at optimal operation temperatures, values in the parentheses correspond to their conventional bulk types.

composites	carrier type	thermal conductivity(W/m/K)	ZT	Ref.
$\text{Si}_{80}\text{Ge}_{20}\text{B}_x$	<i>p</i>	2.5(5.0)	0.95(0.5) at 800-900°C	[21]
$\text{Si}_{80}\text{Ge}_{20}\text{P}_2$	<i>n</i>	2.5(4.6)	1.3(0.93) at 900°C	[17]
$(\text{Bi,Sb})_2\text{Te}_3$	<i>p</i>	1.1(1.4)	1.4(1.0) at 100°C	[12]
$(\text{Bi,Sb})_2\text{Te}_3$	<i>p</i>	1.25(1.4)	1.3(1.0) at 75-100°C	[22]
$(\text{Bi,Sb})_2(\text{Te,Se})_3$	<i>p</i>	1.1 – 1.5	0.7-0.9 at RT	[23]
$\text{Bi}_2(\text{Te,Se})_3$	<i>n</i>	1.0	0.5 at RT	[24]
$\text{Co}_4\text{Sb}_{12}$	<i>p</i>	2.9(4.3)	0.05 at RT	[25]
$\text{Yb}_{0.35}\text{Co}_4\text{Sb}_{12}$	<i>n</i>	1.52	1.2 at 550°C	[24]
$(\text{Ni}_{0.09}\text{Co}_{0.91})_4\text{Sb}_{12}$	<i>n</i>	3	0.75 at RT	[26]
$\text{Mg}_2\text{Si}_{0.4}\text{Sn}_{0.6}$	—	2.1	0.13 at 653K	[27]
$\text{Mg}_2\text{Si}_{0.6}\text{Ge}_{0.4}$	<i>p</i>	4.3	0.21 at 610K	[28]

$\text{Hf}_{0.6}\text{Zr}_{0.4}\text{NiSn}_{0.995}\text{Sb}_{0.005}$	<i>n</i>	3.25(3.8)	1.0(0.8) at 850K	-
$\text{Hf}_{0.6}\text{Zr}_{0.4}\text{NiSn}_{0.99}\text{Sb}_{0.01}$	<i>n</i>	4.4(5.8)	1.0(0.75) at 600°C	[29]
$\text{Hf}_{0.5}\text{Zr}_{0.5}\text{CoSn}_{0.2}\text{Sb}_{0.8}$	<i>p</i>	3.25(4.85)	0.8(0.5) at 700°C	[18]
2atm% $\text{ZrO}_2+\text{Hf}_{0.3}\text{Zr}_{0.7}\text{CoSn}_{0.3}\text{Sb}_{0.7}$	<i>p</i>	3.3(3.6)	0.8(0.65) at 700°C	[30]

As discussed in chapter 1-3, a good candidate for thermoelectric applications should have a low lattice thermal conductivity, a high carrier mobility, and a large carrier effective mass. Normally, a broad-band semiconductor own a high Seebeck coefficient at high temperatures, complex unit cell and heavy atoms always assure low lattice thermal conductivities. Meanwhile, the candidate has to be susceptible to proper carrier doping to reach the optimal carrier concentration. Moreover, a highly symmetric lattice structure indicates a greater degeneracy of energy states and thus helps to improve the Seebeck coefficient.

Other than thermoelectric performance, to be qualified in device fabrication and future commercial promotion, a thermoelectric candidate also has to be:

(1) Thermally stable at the operating temperatures, which limits the applications of Sb-rich skutterudites.

(2) Non-toxic, unlike arsenides, tellurides and selenides.

(3) Susceptible to both N-type and P-type doping, with comparable thermoelectric performance.

(4) Low-cost.

Half Heusler alloys and Silicon Gemernides, as will be discussed in later chapters, are decent candidates that satisfy most of the requirements mentioned above.

1-5 Motivation

As the conflict between the growing demands for energy and the limited reserves of non-renewable fossil fuels (e.g., oil, natural gas, coal) has grown more severe over the years, meanwhile, the environmental impact of global climate change due to the combustion of fossil fuels is becoming increasingly alarming, therefore, research into alternative and renewable energy has become a key priority. One way to improve the sustainability of electricity bases is by recycling waste heat with thermoelectric generators. Many kinds of heat are wasted in our everyday life, among them, wasted heat from automobiles is especially representative, as shown in Figure 1-9. It is surprising that only 25% of the energy from fuel goes into the useful portion as vehicle's kinetic energy, while around 75% is discharged as waste heat, either by heating up coolant or through exhaust gas. TE generators can make

use of the waste heat by converting it into electricity, which is then transferred either directly to the engine or into batteries for other usage.

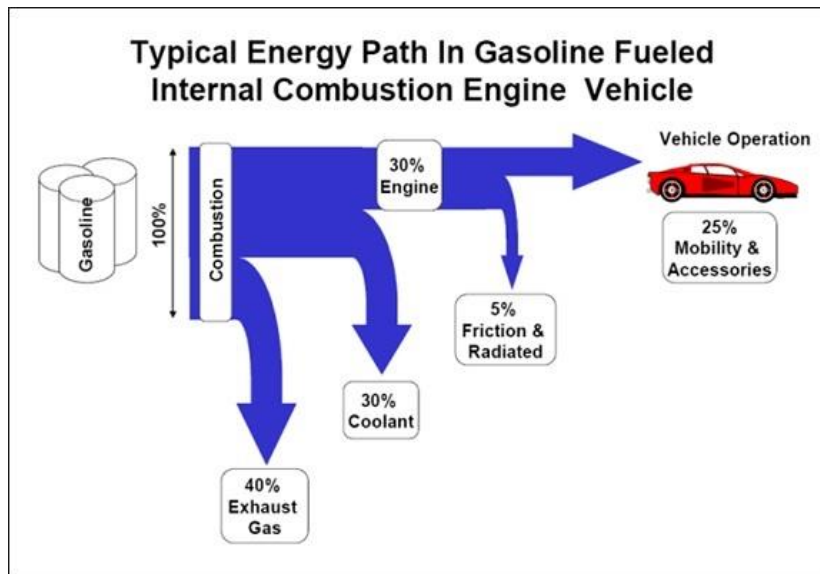


Figure 1-9 A typical energy path in gasoline fueled internal combustion engine vehicle.

As the counterpart of the Seebeck effect, the Peltier effect can be utilized to build TE refrigerators. The advantages of TE refrigerators over traditional ones are: (1) no need for complex electrical circuits and moving parts –TE refrigerators can be built tiny enough for localized cooling; (2) no need for refrigerants utilized in traditional refrigerators, which contain freon, a substance that, when discharged into atmosphere, reacts with the Earth’s ozone layer which protects living beings on the Earth from ultraviolet radiation, thereby increasing the likelihood of skin cancers; and (3) the fact that theoretically TE refrigerators can produce temperatures with no lower limits.

To date, the most effective TE devices can generate electric power or absorb heat at 10% of the Carnot efficiency, whereas traditional refrigerators generally operate between 30% and 90% of the Carnot efficiency for most consumer appliances and large-scale industrial machinery respectively. The substantial drawback of this lack of efficiency has limited the world market for thermoelectric devices to about \$80-160 million annually, notwithstanding their low cost and high reliability.[31] Today, most of these devices are used to cool laser diodes or are sold as novelty consumer appliances. Despite the somewhat disappointing performance of current thermoelectric technologies, in general the efficiency of these TE devices has no known limit short of the Carnot efficiency,[14] which warrants further research in this field.

2. Sample synthesis and characterization

2-1 Sample synthesis

2-1-1 Arc melting

Arc melting is a widely used method to synthesize bulk composites with high melting points. High purity element pieces are melted together under argon atmosphere into button-shaped bulk ingots by induced high power electric arc. Most of the elements used in our alloy synthesis are ordered from Alfa Aesar and Sigma Aldrich; normally, a purity of 99.5% or higher is required to minimize impurities. The arc melting chamber is pumped down to 30 mTorr, and backfilled with argon to ambient pressure; the argon is used to provide a protecting atmosphere during arc melting process. A water-cooled thoriated tungsten electrode is typically used for high voltage arcing generation. During the melting process, a piece of Zirconium is first melted to exhaust residual oxygen before intended compositions are to be alloyed. It should be noted that the raw ingot obtained after first melt needs to be flipped and melted a couple of more times to allow for thorough alloying and to minimize inhomogeneity.

Two noteworthy techniques to arc melt Half Heusler alloys are as follows:

(1) Sb (antimony) is a metalloid with a low sublimation point. To count for the sublimation/loss of Sb during arc melting, additional 5% antimony is strongly suggested when synthesizing Sb rich alloys $XCoSb$ ($X=Hf, Zr, Ti$). This method is proven to be necessary to obtain the intended composites.

(2) A tiny amount of Sb is typically added into $XNiSn$ ($X=Hf, Zr, Ti$) as an N-type dopant; however, due to the low sublimation point of Sb element, any slight Sb loss during melting would lead to a significant deviation of carrier concentration from nominal composite. One technique to solve this problem is to make a Sn-Sb precursor with a MAPP gas torch, since the Sn-Sb solid solution has a much higher sublimation point than Sb. To do so, Sn and Sb pieces with a 10:1 atomic ratio are loaded into a quartz tube, which is then evacuated down to 10 mTorr with a two-phase pumping system (a roughing pump plus a diffusion pump). Sn-Sb pieces are then sealed in the quartz tube with a Hydrogen-Oxygen torch. Thereafter, a MAPP gas torch is used to melt Sn and Sb together homogeneously. It is worth pointing out that MAPP gas is used due to its mild flame temperature, which is incapable of melting quartz but high enough to melt Sn and Sb.

2-1-2 Annealing

Arc melted ingots are water-cooled from above 2000°C down to room temperature in around 10 seconds, this fast cooling process normally results in residual stresses, inhomogeneity, impurity phases and crystal defects, all of which can significantly affect TE materials' performance; hence, post annealing is necessary to obtain a TE ingot that is homogeneous and has a stable TE performance for extended time at elevated temperatures. To prepare for annealing, a TE ingot is wrapped with a piece of tantalum foil and loaded into a piece of quartz tube. The quartz tube is then evacuated down to 10 mTorr and sealed with a Hydrogen-Oxygen torch. The sealed quartz tube is then heat treated in a high temperature furnace following a specific recipe. Taking a N-type Half Heusler alloy for example, the sealed quartz tube normally sits at 900°C for one day to obtain homogeneity, and then at 800°C for 7 to

10 days for phase stabilization. The quartz tube is then quenched in water to retain the sample's high temperature phase.

2-1-3 Induction melting

Metallic alloys can also be synthesized through induction melting by induced Eddy currents; for materials that are too resistive to generate Eddy currents, conductive graphite crucibles are normally used for assistance. With the metallic sample or subsidiary graphite crucible being seat in the middle of a piece of copper coils, a high frequency AC then runs through the copper coils, inducing an high frequency alternating electric-magnetic field, which then induces an alternating electric field in either the sample or the graphite crucible; the electric filed induced Eddy current is very powerful that the sample can be heated up and melted within seconds. Induction melting is specifically useful to melt powder pellets or elemental pieces with low melting points, which otherwise are hard to be synthesized via direct arc melting.

2-1-4 Solid State Reaction

Neither arc melting nor induction melting is able to perform an alloying process with temperature precisely controlled. Dissimilarly, solid state reaction (SSR) (sometimes called solventless reaction or dry media reaction) which is a chemical reaction in the absence of a solvent, is occasionally used to synthesize composites with low melting points or whose reaction processes need to be well controlled to avoid dangerous situations like explosions. For instance, Fe_3P can be synthesized using the following recipe:

(1) Stoichiometric Fe and red phosphorous powders are weighed out and ball mixed in a stainless steel vessel for 40 min to allow sufficient mixing.

(2) The powder mixture is compressed into a cylindrical pellet with an arbor press.

(3) The compressed pellet is then loaded into a piece of quartz tube.

(4) The quartz tube is evacuated with a two-phase pumping system down to 10 mTorr and sealed with a Hydrogen-Oxygen torch.

(5) Finally, the quartz tube is heat treated in a relatively slow and cautious way as following:

- Stays at 100°C for 1 hour
- Stays at 150°C for 1 hour
- Stays at 200°C overnight and one day to allow sufficient reaction of P with Fe
- Stays at 250°C for 2 hours
- Stays at 300°C for 2 hours
- Stays at 350°C overnight

- Stays at 400°C for 2 hours
- Stays at 500°C, 600°C, 700°C, 800°C for 1 hour each
- Finally stays at 900°C overnight

(6)The quartz tube is cooled in air slowly down to room temperature. Goggles are strictly required when the cooled quartz tube is broken, in order to avoid possible explosion due to the outgassing during heat treat process.

2-1-5 Melt spinning

Melt spinning is a technique used to perform rapid cooling in order to obtain amorphous or near amorphous microstructures. A thin stream of melted liquid solution is dripped onto the surface of a rapidly rotating water-cooled copper wheel, resulting in fast solidification. The cooling rate that can be achieved by melt-spinning is between $10^4 \sim 10^7$ K/s. Although it is hard to obtain amorphous TE materials with this method, ribbons with nano-scaled features were still achievable for Half Heusler,[32] Bi_2Te_3 [33] and Si-Ge[34].

Fractures of homogeneously arc melted alloy are loaded into a piece of quartz tube, whose bottom end has been fused into a 0.5mm diameter hole. The quartz tube is then placed right through the center of water-cooled copper coils, and several millimeters above the water-cooled copper wheel. Next, the rotating rate of the copper wheel (typically 3000 rps or round/s) is carefully adjusted, with an AC current

running through the copper coils, the alloy fractures are liquefied and injected out of the quartz tube onto the copper wheel for fast consolidation. The obtained ribbons with nano-sized grains can thus be compressed into bulk form using Spark Plasma Sintering (SPS) or Hot Press (HP) method.

2-1-6 Ball Milling

In addition to melt spinning, ball milling—a powerful mechanical grinding and alloying technique—is also widely used to obtain nano-sized powders. The materials of ball milling vessels and grinding balls have to be carefully chosen to avoid mutual contaminations with TE alloys. Surfactants are also widely used to avoid over-alloying. There are experience rules that the mass ratio of balls to samples has to be between 6:1 and 8:1, and that the quantity ratio of ball size of 0.25” to that of 0.125” has to be between 1:2 and 1:4, depending on sample compositions.

To start, 10 grams of hand ground Half Heusler raw powders or element powders of Si and Ge, as well as grinding balls, are loaded into a pre-cleaned stainless steel vessel; two of these balls are 0.25” in diameter, while the rest four are 0.125” in diameter. The sealed vessel is then fixed in position in the SPEX Dual ball miller 8000D, which is seated in an aluminum box. The aluminum box is then evacuated and backfilled with argon to provide a protecting atmosphere during the ball milling process. Ball milling process usually takes 5 to 10 hours, and the size of obtained particles fall in the range from 20nm to 50nm. The nanopowders can then be consolidated into bulk form with Spark Plasma Sintering (SPS) or Hot Press (HP) technique. Significant grain growth may happen during the SPS or HP process.

SPS is believed to have less grain growth in the sense that the heating/cooling rate of SPS is much faster than its competitor HP.

2-1-7 Spark Plasma Sintering

Spark Plasma Sintering (SPS), also known as field assisted sintering technique (FAST)[35] or pulsed electrical current sintering (PECS), is a powerful sintering technique. The main characteristic of SPS is that the pulsed DC current (typically over 500 A) is directly passing through the graphite die as well as the compacted powder layer; therefore, the heat is generated internally, in contrast to conventional hot pressing (HP), where the heat is transported into the intended powder layer from external hot sink. This internal heating mechanism facilitates a very high heating or cooling rate (up to 1000 K/min); hence, the sintering process is generally very fast (within a few minutes). The rapid heating speed ensures that SPS has the potential to densify the nano-sized powders while avoid the significant grain growth which accompanies standard densification routes. While the term “spark plasma sintering” is commonly used, this term is misleading, since neither a spark nor any plasma is present in the SPS process.[35] It has been experimentally verified that densification is facilitated by the use of a tremendous direct current.

Model 10-4 SPS, a Thermal Technology LLC product, is composed of three main parts: a DC power supply, a hydraulic compressing system and an operation chamber. Fine powders are loaded into a graphite die of 2cm in diameter and sandwiched by a pair of graphite punches. Thin graphite foils are placed between the graphite punches and the compacted powder layer, as well as between the graphite

die and the compacted powder layer, so as to avoid mutual contamination between sample and die. The graphite die is then wrapped by a few layers of graphite fur, in order to minimize heat loss during the heating process so as to maximize the heating rate. The “coated” graphite die is then sandwiched between two graphite blocks before being inserted into upper and lower stainless steel rams which are driven by the hydraulic pump. The temperature of the upper and lower rams can be read from the attached thermal couples. It should be noted that the temperature of either of the rams should not exceed 650 °C for safety reasons; thus, the system is programmed so that once either ram reaches this temperature limit, the whole program will be aborted and the power supply will be cut off immediately. The temperature of the compacted powder layer can be monitored by two independent systems: if the max operation temperature is below 1000°C, a third thermal couple is attached with the lower punch; otherwise, an infrared pyrometer is adopted to read corresponding temperatures.

The compressing chamber is evacuated to or below a setting pressure of 20 mTorr and then backfilled with an inert gas like argon or helium. This backfilling process will be automatically stopped once the pressure in the chamber exceeds the atmosphere pressure. The hydraulic pump-driven rams and the operation chamber are water-cooled during the whole SPS process, and an automatic warning system is also implemented in the water-cooling system. The SPS process (temperature, pressure and holding time) can be pre-programmed using a software program called iTools. The recommended maximal heating rate is 300 K/min, and the ramp rate of pressure is 60 MPa/min. The maximal weight provided by the hydraulic pump is around 10 tons, for a die with inner diameter of 20 mm, the corresponding maximal pressure shall be around 300 MPa. Once the pre-set program is turned on, corresponding SPS parameters can then be read from a software program called SpecView. When the SPS process is done,

allow around 30 minutes for the graphite die and the rams to be water cooled down to room temperature. Normally, the sample obtained is covered by the protecting graphite foils, thus, successive polishing must be performed before the sample can be characterized.

2-1-8 Sample preparation for SEM

Samples in both powder and bulk form can be examined under SEM. For powders, 2 to 3 mg powders are evenly spread on one side of a piece of double-side adhesive, with the other side sticking to an aluminum supporting platform ready for SEM scan. For bulk samples, two options are provided. If morphology of the cross section is to be studied, one may simply crack the bulk into smaller pieces and select one piece with a relatively flat cross section. Or, if grain boundaries and impurity grains are of more interest, fine polishing and surface etching are thus necessary. In this case, the bulk sample is polished with SiC sandpapers in mesh sizes of 300, 800, 1200 and 4000 successively, until the surface becomes mirror-smooth; finer polishing is then performed on a polishing fur with corresponding polishing additives (turbid liquids containing micron-sized Al_2C_3 particles). Next, the sample is cleaned in an ultrasonic vibrator to “shake off” residual Al_2C_3 and SiC particles. After being cleaned, the sample needs to be etched with proper etchant to reveal the surface grains; for HH alloys, the etchant is composed of 4 parts 100% acetic acid, 4 parts 70% nitric acid, and 2 parts 50% hydrofluoric acid. This etchant is applied to the polished surface of the sample, which is then exposed to air for 15 seconds to allow for a sufficient chemical reaction before the surface being cleaned with distilled water.

2-1-9 Sample preparation for TEM

(1) Powders

Powders of approximately 2 to 3 mg are mixed into 100ml alcohol; the turbid liquid is then stirred for 5 minutes to allow for thorough mixing. A veco center reference grid (copper) with 400+ mesh (a TED PELLA product) is then dipped into the turbid liquid for 5 seconds; afterwards, the grid is covered by a piece of wax paper and allow air dry.

(2) Bulk samples

- Polishing: A piece of bulk sample about 5mm x 5mm in size is polished using the method described in section 2-1-8 to a thickness around 150 μ m.

- Dimpling: The sample is stuck on to a TED PELLA designed Cu aperture grid with a 2mm diameter inner hole; it is necessary to tailor the size of the sample so as not to exceed the outer edge of the Cu grid. The Model 200 Fischione Instruments Dimpling Grinder is used to thin the sample to the point that the thinnest part is eventually in the range of 20 to 30 μ m.

- Ion milling: The sample, with its Cu grid base, is fixed on a rotating support platform in the ion mill chamber, which is then evacuated to 10^{-4} Torr. One should adjust the left emission gun to 10° on top of the sample and the right emission gun to 10° below the sample to maximize the ion mill rate. After charging, argon atoms are ionized and accelerated in the electrical field before they bombard onto

the rotating sample. This ion mill process is continued until a hole appears at the center of the dimpled sample. Adjust the both left and right guns to 4° , and perform another 15 minutes ion mill to make the edge around the hole thinner. TEM examination will be focused on the edge around the hole, because only this region is thin enough for the transmission of electrons.

2-2 Sample characterization

2-2-1 X-Ray Diffraction

Powder X-Ray Diffraction (XRD) can be used to identify crystalline phases and to trace the changes on lattice constant due to doping level. A piece of alloy is smashed with a hammer and hand ground into micron-sized powders with mortar and pestle. Obtained powders are then spread on top of a piece of single crystal substrate, which is utilized to minimize the background signals. Diffracted beam adopts a Ni beta-filter and a 0.04rad soller slit. Usually, the scanning range is from diffraction angle $2\theta = 20^\circ$ to $2\theta = 80^\circ$, although this may be adjusted if necessary. The diffraction patterns obtained are then compared with the database to identify the crystal structures, and possible composites.

It worth nothing that XRD peaks can also be utilized to estimate crystallite size, which will be introduced in detail in chapter 4.

2-2-2 Atomic Force Microscopy

Atomic force microscopy (AFM), also called dynamic force microscopy (DFM), is a scanning probe microscopy of very high resolution. Its main component is a piezoelectric feedback loop, which is used to keep a constant tip-sample interaction, the interaction signal in return can be used to adjust the height of the tip above the sample surface. A Nanosurf easyScan dynamic force microscopy is used for surface scanning of well-polished and etched samples and for grain-size determination by a silicon cantilever that is 228 μm in length. This DFM can be operated in three modes:

(1) Static force mode

A laser beam deflection system with an 830nm characteristic wavelength and an 0.4mW operation power is used to measure the bending of the cantilever. The deflected laser is then gathered by array of photodiodes for imaging.

(2) Dynamic force mode

The cantilever is oscillated at a pre-set amplitude and at a frequency near its resonance by a piezo element. Any change on the tip-sample forces will alter the resonance frequency of the cantilever, thereby inversely altering the oscillating amplitude, which is measured by the laser deflection system.

(3) Phase contrast mode

This mode is essentially an enforced dynamic force mode. In addition to the oscillation amplitude, the oscillation phase of the cantilever is also monitored, providing information regarding the relative stiffness of the sample surface under the tip; hence, this mode is used primarily to detect possible nanosized minor phases in the main matrix.

The scan area of AFM can be as large as $10\mu\text{m}$ by $10\mu\text{m}$, and the characteristic features as small as $20\sim 30\text{nm}$ can be resolved.

2-2-3 “Homemade” high temperature probe

The Seebeck coefficient and electrical resistivity can be measured simultaneously using a homemade HT probe up to 1100K , the probe’s schematic structure is sketched in Figure 2-1.

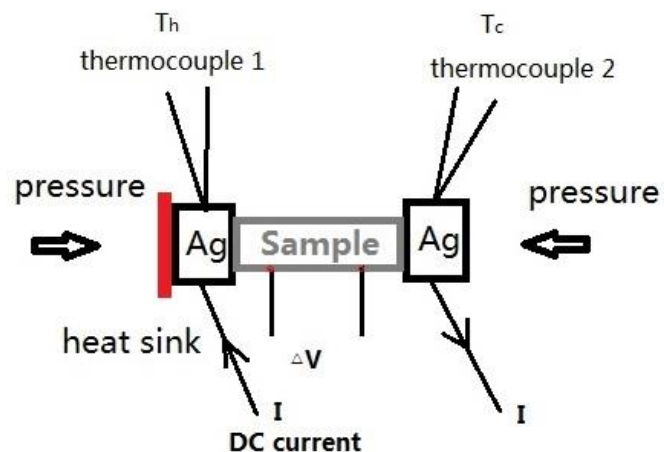


Figure 2-1 A schematic “homemade” high temperature thermoelectric probe.

A sample to be measured is cut into a rectangular piece of 10mm x 4mm x 4mm before being inserted between two silver blocks. External pressures are then applied on both sides to make sure that the sample tightly sticks against the silver blocks so as to provide reliable thermal and electrical contacts. In a typical resistance measurement loop, constant DC current I (10^{-3} A) runs into one silver block, through the sample, and out from the other silver block. Voltage ΔV , across a pre-measured distance along the sample, is measured. Resistivity can then be derived from this well-known four-point resistance measurement method, which was first proposed by Lord Kelvin in 1861:

$$\rho = \frac{Rl}{S} \quad (2-1)$$

Where ρ is the electrical resistivity, l is the distance between the two voltage leads, S is sample's cross section. In a typical Seebeck coefficient measurement loop, a heater strip is used to heat up the hot sink, temperature T_h of hot end is then read by thermocouple 1, while T_c of the cold end is read by thermocouple 2. The Seebeck voltage ΔV_s , induced by the temperature difference $\Delta T = T_h - T_c$, is read by the DC current leads. Note that ΔV_s also receives a contribution from the silver blocks; to calculate the net Seebeck coefficient of the sample, one has to subtract the thermopower of silver- S_{Ag} from total Seebeck $\Delta V_s / \Delta T$, S_{Ag} is given by an experience formula as:

$$S_{Ag} = 0.97153 - 0.0018878T + 1.3617E-5 T^2 - 4.7322E-9 T^3 \quad (2-2)$$

Other than the data acquisition probe described above, the measuring circuit also contains a Keithley 220 precision current source, a Keithley 2182 nanovoltmeter, a Keithley 7001 control system

and an Agilent E3642A DC power supply. This system of data acquisition and analysis circuit was programmed by S. R. Culp via Labview, as outlined in his PhD thesis.[36]

Despite this HT probe's moderate performance, the drawbacks listed below make it necessary to find a replacement.

(1)Both the DC current supply loop and the temperature acquisition loop are wired with silver strings of 0.25mm in diameter, which are extremely brittle in light of the possibility of external force and high temperature "baking" during the measuring process.

(2)Two tiny Ni-Cr wires are attached to the sample as voltage leads via silver paint, however, this sort of attachment is unstable and always cause loose electric contacts during measurements.

(3)The probe necessitates frequent refurbishment to get rid of residual contaminants which may lead to short circuits.

(4)It is hard to obtain a steady state temperature at which the Seebeck coefficient can be measured, since the heating unit of the whole probe and the heater strip attached with the hot sink are controlled independently.

2-2-4 ZEM-3

A more sophisticated measuring unit to be introduced is the Seebeck coefficient/Electric resistance measurement system ZEM-3 by ULVAC-RIKO Inc.



Figure 2-2 ZEM-3 system made by ULVAC-RIKO Inc.

The working mechanism is similar to that of the HT probe described in chapter 2-2-3; however, improvements in the following aspects make this system more reliable:

(1)The wires for thermocouples and thermal contacts in ZEM are made of platinum (Pt), which is less prone to deformation and crack than silver (Ag).

(2)The operation chamber holding the probe can be evacuated to 10 mTorr in a couple of minutes and backfilled with protecting gas, thus refurbishment is no longer necessary; it also has a built-in relief valve for safety reasons.

(3)Thermal and electrical contacts are ensured by both vertical and horizontal external pressure.

(4) The heating unit of the chamber coordinates well with the heater strip attached with the hot sink, ensuring a steady state temperature at any measuring point.

2-2-5 Thermal conductivity

The pulse or laser flash method to determine thermal conductivity was first described by Parker *et al.*[37] in 1961; since its inception, approximately more than 75% of all thermal diffusivity results published in the primary scientific literature[38] after the 1970s have been obtained using this single technique. A Netzsch LFA 457 MicroFlash system is used to perform laser flash thermal conductivity measurements. One surface of a disc-shaped sample (dimensions 1/2" x 1/2" x 1/10") is irradiated by a short (less than 1ms) laser pulse. The resultant temperature T on the opposite surface is recorded; the thermal diffusivity δ can then be computed from T vs. time data:

$$\delta = \frac{1.37L^2}{\pi^2 t_{1/2}} \quad (2-4)$$

Where L is the diameter of the disc-shaped sample, and $t_{1/2}$ is the time taken for the temperature on the rear surface to reduce to half its maximum value. This technique relies on the fulfillment of relatively stringent boundary conditions,[16] namely:

- (1)The pulse of energy is uniformly absorbed in a small depth at the surface $x=0$,
- (2)The heat pulse dissipation time is of negligible duration, and
- (3)The measurement time is sufficiently short so that no loss of heat occurs from the sample.

As long as thermal diffusivity is determined, the thermal conductivity can be calculated via:

$$\lambda = C_p \rho \delta \quad (2-4)$$

Mass density ρ is measured via classical Archimedes method, and specific heat C_p is measured by a Netzsch LFA Differential Scanning Calorimeter (DSC). The DSC technique was developed by Watson and O'Neill in 1962 and introduced commercially at the 1963 Pittsburgh Conference on Analytical Chemistry and Applied Spectroscopy. The first adiabatic differential scanning calorimeter usable in biochemistry was developed by Privalov and Monaselidze in 1964.[39] During a measurement, intended sample and reference material of equal weight are maintained at nearly the same temperature throughout the experiment. The temperature program for a DSC analysis is designed such that the sample holder's temperature increases linearly as a function of time. Since the reference material has a well-defined heat capacity over the range of temperatures to be scanned, provided the difference in

required heat to maintain the intended and reference samples at the same temperature, one can then determine the intended sample's heat capacity.

2-2-6 Hall Effect

Hall effect was discovered by Edwin Hall in 1879. The process can be described as follows: when a current is passing through a conductor in a perpendicular magnetic field, the charge carriers constituting the current will accumulate in the direction transverse to both the direction of the current flow and the direction of the applied magnetic field, due to the Lorentz force; the process eventually will arrive at equilibrium when the induced electric field due to carriers' accumulation can completely balance the effect of the Lorentz force. This induced electric field is named the Hall voltage V_H , and the ratio of Hall voltage to the product of the current density and the magnetic field is called Hall coefficient. The Hall coefficient is a characteristic property of the conductor, which reveals carrier's type and density as follows:

$$V_H = -\frac{IB}{net} \text{ or } R_H = \frac{V_H t}{IB} = -\frac{1}{ne} \quad (2-5)$$

Where t is the thickness of the conductor in the direction of magnetic field.

A VersaLab, 3 Tesla, Cryogen-free Vibrating Sample Magnetometer (VSM) is used to conduct the Hall effect measurement. This VSM has a sensitivity of 10^{-6} emu/rt-Hz, a characteristic maximal magnetic field up to 3 Tesla, and an operating temperature ranging from 50 to 400K. In our case, a

carefully polished rectangular sample is mounted on a sample holder, the electrical joints of which are then wired with two ends and two perpendicular sides of the sample, forming a typical four-point resistance measuring circuit. The electrical connections between wires and leads are soldered by Indium. The magnetic field is applied in the direction perpendicular to the sample holder. The electrical leads on the two ends of the sample are used as current supply and the other two on the sides are used to record the induced Hall voltage. In a typical measuring loop, current flow I is kept constant, as the magnetic field varies, corresponding Hall resistances $r_H = V_H/I$ are automatically recorded. For non-magnetic materials, the outcome is a linear dependence of Hall resistance r_H on the applied magnetic field B ; the slope is then expressed as $L = r_H/B = V_H/IB = -1/neL$. With carrier density $n = -1/eL$ being calculated, the carrier mobility is then derived as follows:

$$\mu = -\frac{\sigma}{ne} = Lt\sigma \quad (2-6)$$

3. Thermoelectric properties improvement on Half Heusler alloys via nanostructuring

Half Heusler (HH) alloys of MNiSn and MCoSb ($\text{M}=\text{Hf, Zr, Ti}$) types are well-studied TE materials with decent performances at high temperatures ranging from 700K to 1100K;[40][41] in addition, they are low-cost and non-toxic. The thermoelectric performance of Half Heusler alloys is mainly limited by their comparably high thermal conductivity. This chapter will focus on how to improve the thermopower and reduce the lattice thermal conductivity. Through introducing localized impurity states, the density of states (DOS) of host at the Fermi level can be significantly increased over a narrow range, forming so-called resonant states, which can greatly enhance the Seebeck coefficient according to the Mahan-Sofa theory.[42] Mechanical alloying/ball milling is adopted to implement nanostructured features into state-of-the-art bulk HH, not only leading to a reduction in thermal conductivity by the much more intense interface scattering at grain boundaries, but also resulting in low energy carriers that are detrimental to thermopower being trapped at grain boundaries, eventually an improvement in the Seebeck coefficient.

The work in this chapter has been published in by J. W. Simonson, D. Wu *et al.* in *Phys. Rev. B* **83** (2011) 235211 and by S. J. Poon and D. Wu *et al.* in *Journal of Materials Research* **26** (2011) 22.

3-1 Introduction of Half Heusler (HH) alloys

The crystal structure of HH alloys is a face centered cubic (FCC). For example, in MNiSn, the transition metal M (M=Hf,Zr,Ti) atoms and Sn atoms form a rock salt (NaCl) frame, with four Ni atoms filling half of the eight quadrants, as shown in Figure 3-1. This is also the origin of the term “Half Heusler”, compared with “Full Heusler” in which all eight quadrants are occupied.

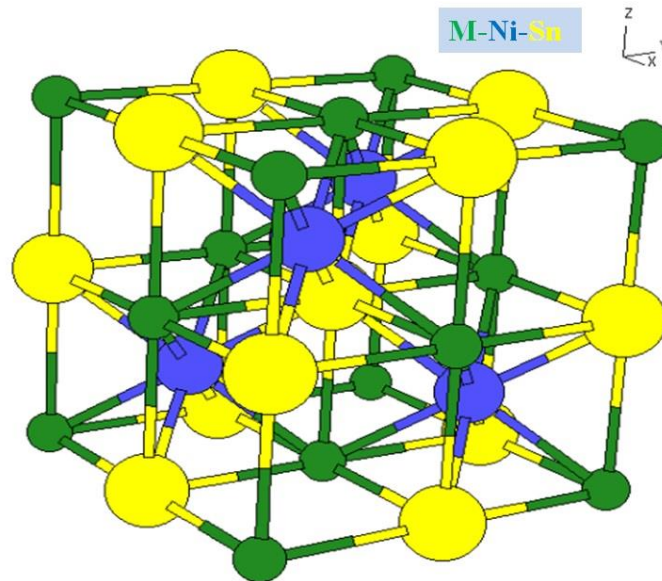


Figure 3-1 Crystal structure of MNiSn (M=Hf, Zr, Ti) Half Heusler phase.

Undoped intrinsic Half Heusler alloys express semiconducting properties, as their valence electron count (VEC) is equal to 8 or 18, and the band gap for typical MNiSn/MCoSb (M=Hf, Zr, Ti) lies in the range of 0.5~0.8 eV. The origin of the band gap in Half Heusler is still unclear; calculations via first principles show that it either comes from the combination effect of M-3d – Sn-4p strong hybridization

and Ni-3d orbitals indirectly mediating the interaction between the M- d_{xy} orbitals and hybridized M-3d – Sn-4p[43], [44] or comes from the d-d repulsion between Ni-3d orbitals and strongly hybridized M-3d – Sn-4p.[45] In either case, the conduction band edge is predominated by M-3d character, while the valence band edge is predominated by Ni-3d orbitals.

Although high Seebeck coefficients were observed in intrinsic MNiSn/MCoSb,[45], [46], [47] the relatively low electrical conductivities result in insufficient Power Factors ($PF=S^2\sigma$) for any actual applications. The Power Factors of intrinsic Half Heusler alloys can be greatly improved by proper doping on the Sn/Sb site, as has been shown in many works.[36], [40], [41] Further enhancement in the Seebeck coefficient can be achieved with band structure engineering – specifically, increasing the local density of states (DOS) at the Fermi level by introducing localized impurities to the matrix material. Additionally, low energy carriers are found to be detrimental to thermopower, as discussed theoretically and experimentally by Shakouri *et al.*,[48] their finding further indicates that preferentially scattering low energy carriers via energy barriers can result in an enhanced Seebeck coefficient.

It has also been well presented that the thermal conductivity can be reduced by over 50% through introducing isoelectronic elements, specifically $Hf_{1-x-y}Zr_xTi_yN(N=Ni,Co)S(S=Sn,Sb)$,[49], [50] without compromising the Power Factor.[41][51] The dramatic reduction of thermal conductivity is attributed to mass fluctuation effect/point defect scattering-phonon transport is impeded by the strain field fluctuation. A widely used model to evaluate point defect scattering is the Klemens-Drabble theory.[50], [52] Moreover, nanostructuring techniques have also shown great promise of achieving high ZT[18], [32], [53], [54], [55], [56] by significantly reducing thermal conductivity; in some cases, they can result in

Power Factor $PF(=S^2\sigma)$ enhancement.[9], [13] The mechanism of nanostructuring is understandable in the sense that interfaces intensity among embedded nanoparticles and matrix materials is significantly increased, these interfaces act as both thermal barriers and scattering centers of acoustic phonons,[14], [15], [16] as well as energy filterers for charge carriers, resulting in the reduction of thermal conductivity and the enhancement of thermopower.[32], [57]

3-2 Resonant states

3-2-1 Background

In most semiconductors, the addition of doping atoms results in extra impurity states in the band gap. When these states are close to valence (conduction) band edges, the holes (electrons) in the impurity states will tend to be thermally activated into the valence (conduction) band and thereby lead to an increase of carrier concentration. There is also an exception to this mechanism; specifically, when the impurity states introduced by dopants lie in the valence or conduction band edge, a localized increase of density of states over a narrow energy range may be formed due to the strong hybridization between the impurity states and matrix band, forming so-called resonant states, as shown in Figure 3-2. The theory of localization of DOS was well studied in the $GaAs_{1-x}N_x$ system by Wu *et al.*[58] and in the $ZnSe_{1-x}O_x$ system by Lee *et al.*[59] A remarkable increase in the Seebeck coefficient, and therefore ZT, was also observed in a state-of-the-art PbTe system with 2% Tl doping on the Pb site by Heremans *et al.*[9]

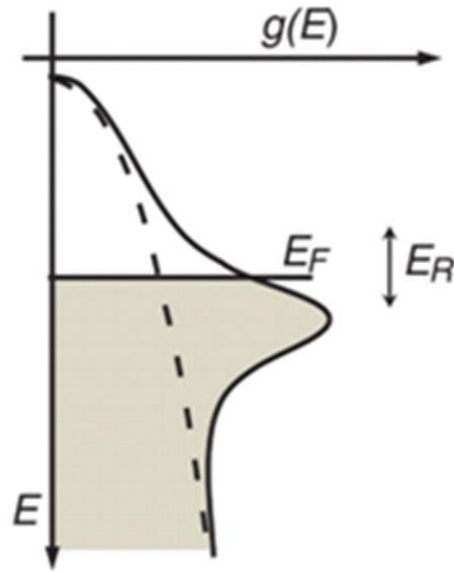


Figure 3-2 Localized resonant states over a narrow energy range E_R at Fermi level.

The mechanism of enhancement of the Seebeck coefficient by localized DOS increase at the Fermi level can be expressed using the Mott expression[60] as follows:

$$S = \frac{\pi^2 k_B^2 T}{3q} \left. \frac{d[\ln(\sigma(E))]}{dE} \right|_{E=E_F} = \frac{\pi^2 k_B^2 T}{3q} \left\{ \left. \frac{1}{n} \frac{dn(E)}{dE} \right|_{E=E_F} + \left. \frac{1}{\mu} \frac{d\mu(E)}{dE} \right|_{E=E_F} \right\} \quad (3-1)$$

With the differential electrical conductivity σ expressed as:

$$\sigma(E) = n(E)q\mu(E) \quad (3-2)$$

Where carrier concentration $n(E)=g(E)f(E)$ is the product of DOS $g(E)$ and Fermi distribution function $f(E)$ at E , $\mu(E)$ is the energy dependent carrier mobility. From Eqn (3-1), an enhanced Seebeck coefficient can be expected, if the Fermi level lies where DOS $g(E)$ (and therefore $n(E)$) is experiencing a steep change.

3-2-2 Experiments

Polycrystalline Half Heusler alloys of nominal compositions $(\text{Hf}_{0.75}\text{Zr}_{0.25})_{1-x}\text{V}_x\text{NiSn}$ with $x=0\%$, 0.25% , 0.5% and 1.0% were arc melted 3~4 times to allow for homogeneity, and the mass losses during arc melting processes were strictly controlled under 0.5% . The purities of the commercially available elements Hf, Zr, V, Ni and Sn are 99.7% , 99.95% , 99.7% , 99.98% and 99.99% , respectively. The as-casted ingots were then sealed in quartz tubes under vacuum for post-annealing, the details of which were described in chapter 2-1-2. The post-annealing recipe is at 900°C for 1 day, and 800°C for 7 days. Post-annealing was performed in order to allow for strain release and crystal growth via thorough diffusion. The existence of the Half Heusler phase was then identified by XRD diffraction, and homogeneity was verified via Energy Dispersive Spectroscopy (EDS) line scan (Figure 3-3) over a well-polished sample, as presented in our published work.[61]

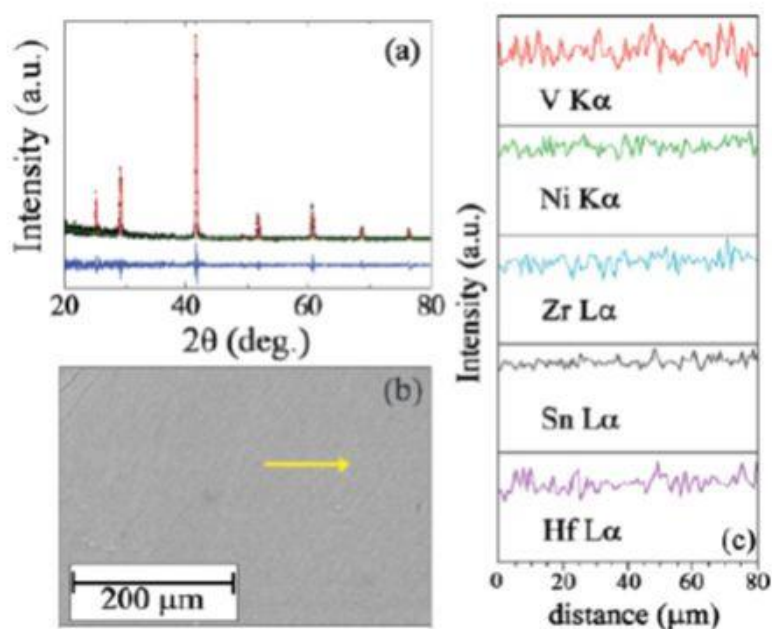


Figure 3-3 (a) Powder XRD scan (b) SEM image of surface micrograph and (c) EDS line scan of $(\text{Hf}_{0.75}\text{Zr}_{0.25})_{0.99}\text{V}_{0.01}\text{NiSn}$ along the yellow arrow in (b).

The actual chemical compositions of V doped HH alloys were determined by EPMA (Electron Probe Microanalyzer) with 50 ppm detection limit. The atomic percentages of V were found to be 0.24%, 0.63% and 0.78%, somewhat deviating from the nominal 0.25%, 0.50% and 1.0%; nevertheless, the increasing trend of V content in $(\text{Hf}_{0.75}\text{Zr}_{0.25})_{1-x}\text{V}_x\text{NiSn}$ was still retained.

Thermopower and electrical resistivity from RT (300K) to 1083K were measured with a home-built high temperature thermoelectric probe. It can be seen from Figure 3-4 that the electrical resistivity remained constant upon V doping from 0% to 0.78%, whereas thermopower was found to be enhanced as the V content increased from 0% to 0.63% in the temperature range from 300K to 700K. In particular,

the 0.63% V-doped sample achieved a maximal RT thermopower of $-260\mu\text{V}/\text{K}$, compared with undoped one of $-196\mu\text{V}/\text{K}$.

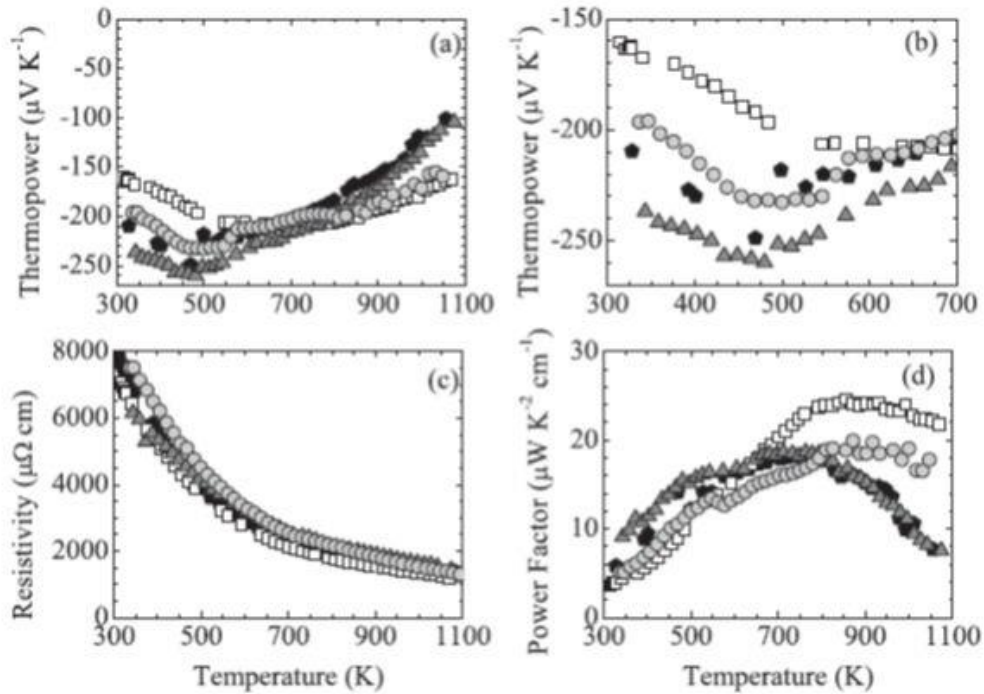


Figure 3-4 Thermopower in the range of (a) 300K to 1100K (b) 300K to 700K, and (c) electrical resistivity (d) power factor for V doped HH $(\text{Hf}_{0.75}\text{Zr}_{0.25})_{1-x}\text{V}_x\text{NiSn}$, with $x=0\%$ (open square), 0.24% (gray circle), 0.63% (gray triangle) and 0.78% (black pentagon).

3-2-3 Discussions

The enhancement of thermopower S indicates that V atoms were not doped into the band gap as normal donors, instead, they introduced a local increase of density of states near or within the band gap,

where Fermi level lies. The enhancement effect on S diminished at higher temperatures (over 600K), the reason can be attributed to the promotion of electrons further into the conduction band, away from the local enhancement feature of DOS; on the other hand, this phenomenon implicitly discloses that the locally increased DOS feature spreads only across a narrow energy range, around 50 meV. This range is estimated as $2k_B\Delta T=2*0.0256 \text{ eV}\sim 50 \text{ meV}$, which is very small compared with either the theoretical band gap of 0.5 eV or the experimental effective bandgap of 0.23 eV of ZrNiSn.[62]

No obvious changes in band gap width were found in this series of V- doped $\text{Hf}_{0.75}\text{Zr}_{0.25}\text{NiSn}$ samples, unlike chalcogenide systems, which showed a systematic decrease in band gap width coinciding with the incorporation of resonant states into the matrix density of states near the Fermi level. Presented in Figure 3-5 are plots of $2k_B\ln(\rho)$ vs. $1/T$ for V- doped Half Heusler samples, at the temperature range from 900K to 1030K; the slopes of corresponding linear fitted lines represent the width of band gaps. The band gap widths, which can be found in Table 3-1, agree very well with the reported experimental value of 0.23 eV.

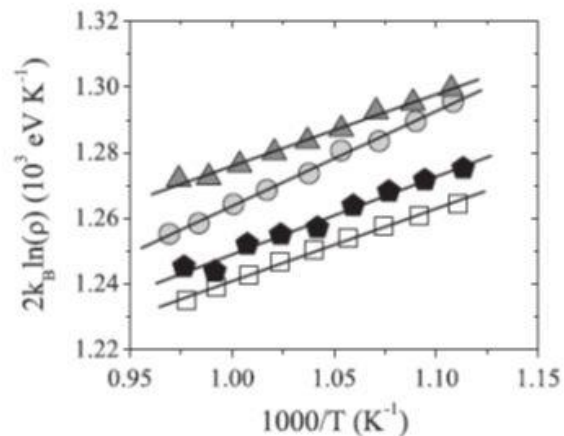


Figure 3-5 Plots of $2k_B \ln(\rho)$ vs. $1/T$, with slopes representing width of band gaps. From top to bottom, the plots are: 0.63% (dark grey triangle), 0.24% (light grey circle), 0.78% (black pentagon) and 0% (open square) V- doped $\text{Hf}_{0.75}\text{Zr}_{0.25}\text{NiSn}$ separately.

An explanation of the somewhat unexpected small change of band gap width in V doped $\text{Hf}_{0.75}\text{Zr}_{0.25}\text{NiSn}$ alloys can be stated as follows: ab-initio calculations[63] suggest a non-zero density of states due to the existence of antisite disorder in the band gap even in undoped ZrNiSn , these stable energy states then hybridize with the unstable localized V 3d-orbitals, forming a localized resonance which can hold certain quantity of electrons, preventing the Fermi level moving up to the conduction band edge until these resonant states are overfilled by electrons coming from other dopants.[64], [65]

A single parabolic band model[66] was adopted for following discussions; within this model, it is assumed that longitudinal acoustic scattering ($r=0$) dominates:

$$\begin{cases} S = \pm \frac{k_B}{e} \left(\frac{(2+r)F_{1+r}(\eta^*)}{(1+r)F_r(\eta^*)} - \eta^* \right) \\ F_r(\eta^*) = \int_0^\infty \frac{x^r}{1+\exp(x-\eta^*)} dx \\ n = 4\pi \left(\frac{2m^*k_B T}{h^2} \right)^{\frac{3}{2}} F_{1/2}(\eta^*) \end{cases} \quad (3-3)$$

Where S is the Seebeck coefficient, r is the scattering mechanism factor, $\eta^* = E/\eta_0$ is reduced Fermi energy, F_r is the r -th Fermi integral, n is the carrier density and m^* is carrier's effective mass. A numerical approach is utilized to find out the reduced Fermi energy from the Seebeck coefficient at

room temperature, together with carrier concentration n which can be derived from the Hall effect; effective carrier mass m^* was then obtained. Corresponding values are listed in Table 3-1.

Table 3-1 Thermoelectric properties of V-doped $\text{Hf}_{0.75}\text{Zr}_{0.25}\text{NiSn}$.

x	S_{RT} ($\mu\text{V}/\text{K}$)	E_{gap} (eV)	n (cm^{-3})	μ ($\text{cm}^2/\text{V s}$)	m^* (m_0)	γ ($\text{mJ}/\text{mol}\cdot\text{K}^2$)	$N(E_F)$ (states/eV unit cell)	θ_D (K)
0	-167	0.22	5.5×10^{19}	16	1.5	0.42	2.2	250
0.0024	-196	0.27	4.2×10^{19}	20	1.6	0.49	2.5	250
0.0063	-237	0.22	4.1×10^{19}	24	2.2	0.53	2.7	252
0.0078	-209	0.22	3.3×10^{19}	25	2.1	0.78	4.0	251

It can be seen that, although the carrier concentration n decreases as V doping level increases, there is little change in the electrical resistivity ρ , as shown in Figure 3-4; that is because the reduction in n is compensated by carrier mobility enhancement. The unexpected carrier concentration reduction due to V doping strongly indicates that the doped V atoms do not exist as normal donors in the band gap, instead, they hybridize with matrix states and result in an resonance of DOS. The enhancement of the Seebeck coefficient can also be understood in terms of Mott expression shown in Eqn (3-1):

$$S = \frac{\pi^2 k_B^2 T}{3q} \left. \frac{d[\ln(\sigma(E))]}{dE} \right|_{E=E_F} = \frac{\pi^2 k_B^2 T}{3q} \left\{ \left. \frac{1}{n} \frac{dn(E)}{dE} \right|_{E=E_F} + \left. \frac{1}{\mu} \frac{d\mu(E)}{dE} \right|_{E=E_F} \right\} \quad (3-1)$$

Vanadium doping supplements the number of valence electrons of the whole system, thereby increases the carrier energy E . In this case, the dependence of $n(E)$ and $\mu(E)$ on carrier energy E can then be interpreted via dependence on vanadium doping level. It can be seen from Figure 3-6 that the slope of carrier concentration n vs. V doping level (%V) remains negative from 0% to 0.78%; however, the

positive slope of carrier mobility μ vs. V doping level (%V) compensates for this negative trend in the range of 0% to 0.63%. Once the slope of μ starts to flatten at 0.78%, the negative trend of carrier concentration dominates, eventually resulting in a diminished Seebeck coefficient. This trend of the Seebeck coefficient can also be interpreted in terms of carrier effective mass, which is also presented in the figure.

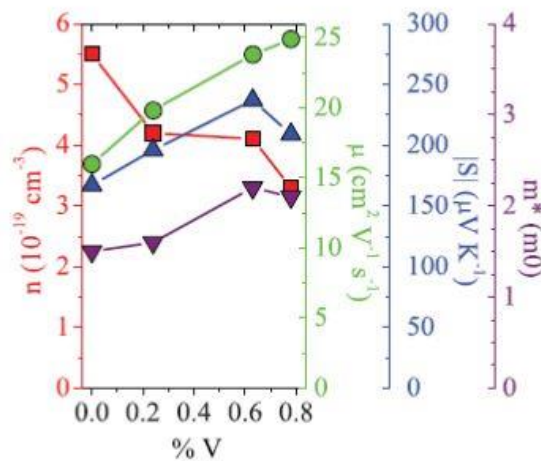


Figure 3-6 The dependence of carrier concentration n , carrier mobility μ , Seebeck coefficient S and carrier effective mass m^* on V doping level in intrinsic $\text{Hf}_{0.75}\text{Zr}_{0.25}\text{NiSn}$ alloys.

It worth noting that carrier mobility $\mu = e \langle \tau \rangle / m^*$ in a single parabolic band semiconductor; in our case, however, effective mass m^* and carrier mobility increase simultaneously as the doping level of V goes up. This atypical observation might be attributed to the substantial modification of the density of states predicted by interimpurity Columbic interactions over impurity-host hybridization, which was used to explain increased carrier mobility with dopant concentration. Upon the sharp modification of the

band structure, the calculated effective mass based on the simple parabolic band model thus appears questionable. In light of this development, heat capacity measurements were performed to provide a direction view of density of states increase at Fermi level.

Heat capacity measurements were performed on V-doped $\text{Hf}_{0.75}\text{Zr}_{0.25}\text{NiSn}$ alloys. At temperatures far below Debye temperature and Fermi temperature, the heat capacity of a solid can be expressed as a combination of electrical and phonon contributions:

$$C_p = \gamma T + \beta T^3 \text{ or } \frac{C_p}{T} = \gamma + \beta T^2 \quad (3-4)$$

The electrical contribution is proportional to temperature T , while the phonon contribution is proportional to T^3 . The Sommerfeld constant γ is used to derive the density of states at the Fermi level $N(E_F)$ via the formula as:

$$\gamma = \frac{\pi^2}{3} k_B^2 N(E_F) \quad (3-5)$$

With the intercept of C_p/T vs. T plots being determined, $N(E_F)$ can then be figured out.

The C_p/T dependence on T^2 is shown in Figure 3-7, and corresponding density of states at the Fermi level at absolute zero temperature for different doping levels are listed in Table 1. A 23% increase in density of states at the Fermi level was observed when vanadium's doping level increased from 0% to 0.63%. The Debye term of the heat capacity, given by the slope β , has almost no variation, which

indicates that there is little change in the phonon spectrum due to the introduction of impurity vanadium atoms.

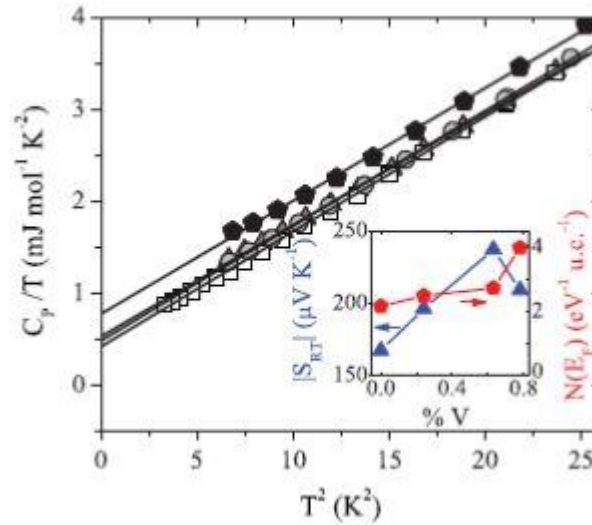


Figure 3-7 The dependence of heat capacity C_p on temperature at temperatures ranging from 1.8K to 5.0K in V doped $\text{Hf}_{0.75}\text{Zr}_{0.25}\text{NiSn}$ alloys, the inset shows that dependence of the Seebeck coefficient at room temperature and density of state at the Fermi level on V doping level.

3-2-4 Conclusions of resonant states

Enhancement of the Seebeck coefficient was observed for V-doped intrinsic semiconductor $\text{Hf}_{0.75}\text{Zr}_{0.25}\text{NiSn}$ in the temperature range from 300K to 600K. The enhancement was attributed to the localized density of states at Fermi level due to the resonance of introduced Vanadium's d-orbitals with matrix's conduction band edge. This conclusion was analyzed in a single-band model via effective mass

calculation and then qualitatively explained using the Mott expression. Finally, low-temperature heat capacity measurement was utilized to experimentally verify the existence of DOS increase near the Fermi level.

3-3 Nanostructuring

Nanostructuring refers to various techniques used to construct nanostructured features in conventional materials. Enhancement of thermoelectric properties can be achieved in nanostructured form in means which are otherwise not possible in corresponding bulk form.[12], [67], [68] Hick and Dresselhaus[69] were the first to propose to use lower dimensional structures to selectively modify materials' properties; they showed in their work that, by utilizing zero-, one- and two- dimensional structures, one could obtain remarkable improvement in electronic properties. Theoretical work also showed significant reductions in lattice thermal conductivity via nanostructuring in lower dimensional nanostructures,[70] which was soon experimentally proved.[71], [72], [73], [74] Later on, a very low thermal conductivity was reported in a three dimensional nanocomposite - ErAs nanoparticles embedded $\text{In}_{0.53}\text{Ga}_{0.47}\text{As}$, [75] and enhanced Seebeck coefficients were also achieved in three dimensional nanostructures.[76], [77]

Due to the relatively complex fabrication process and extremely low yield, lower dimensional thermoelectric nanostructures are less favored to be applied in TE devices than their three dimensional

counterparts. Mechanical alloying (MA), melt spinning (MS), hydrothermal method and other methods are employed to obtain three dimensional nanostructured thermoelectric materials. In our case, the MA method, or also called ball milling (BM) was adopted.

3-3-1 Exploration in finding proper BM vessel

Mechanical alloying (MA) is a solid-state powder processing technique involving repeated cold welding, fracturing, and re-welding of powder particles in a high-energy ball mill. It was originally developed to produce oxide-dispersion strengthened (ODS) nickel- and iron- based super alloys for applications in the aerospace industry. MA has now been shown to be capable of synthesizing a variety of equilibrium and non-equilibrium alloy phases starting from blended elemental or pre-alloyed powders. Mechanical alloying is akin to metal powder processing, where metals may be mixed to produce super alloys. Mechanical alloying normally occurs in three steps. First, materials are alloyed in a ball mill and ground to a fine powder. A hot pressing (HP) or Spark Plasma Sintering (SPS) process is then applied to simultaneously compress and sinter the powder. A final heat treatment stage helps to remove residual stresses produced during any cold compaction that may have been used.

Oxidizations, incomplete alloying, and contamination from BM vessels always cause remarkable differences in thermoelectric properties, which are usually detrimental to figure of merit ZT ; therefore, well-selected BM vessels, reasonable BM time and an inert BM environment are key components needed to obtain clean, fine and well-alloyed nanopowders.

Our first trial uses a hardened steel grinding vial set from SpexSamplePrep. The cylindrical vial is 2.25" in diameter and 3" in height (5.7 cm x 7.62 cm), with a volume of 65 mL. It also includes a screw-on cap and two 0.5" (12.7 mm) and four 0.25" (6.35 mm) steel balls, these grinding balls as well as the vessel are made of type 52-100 steel. Unfortunately, Fe contaminations were detected after five hours BM, and the condition was even worsened with longer BM times. Our earlier research[44] found that even a tiny bit of Fe content can lead to a fatal detriment to thermopower S . The reason is that Fe atoms exist as P-type dopants upon replacing Ni atoms, while Zr(Hf)NiSn itself is an N-type semiconductor; therefore, the Seebeck coefficient is harmed by the contradictory effect.

The next trial uses the 45 mL zirconia ceramic grinding vial set. The vial is 2.5" in diameter and 2.69" in height (6.35 cm by 6.8 cm). This zirconia set also includes a slip-on cap, and two zirconia balls of 0.5" (12.7 mm) and the other two of 0.25" (6.4 mm). Although the hardness of ZrO_2 is high (Mohs 8.5), contamination was still detected after only 5 hours of BM. The zirconia (ZrO_2) impurity into HH content resulted in significantly reduced electrical conductivity.

The most satisfactory vial set is made of 440C hardened stainless steel. This is a high-carbon high-chromium stainless steel, capable of developing high hardness and high mechanical properties by conventional heat treating methods. The 440C steel exhibits remarkable corrosion resistance in the hardened condition. It has excellent resistance to wear and abrasion and is magnetic in all conditions. It develops the highest hardness of the stainless steels. No obvious coarsened surface was found either on the inner wall or on the grinding balls of this 440C stainless steel set, nor was contamination in intended Half Heusler powders detected, even after 15 hours of continuous BM.

X-ray patterns in Figure 3-8 provide the evidences of contaminations when N-type $\text{Hf}_{0.6}\text{Zr}_{0.4}\text{NiSn}_{0.995}\text{Sb}_{0.005}$ were ball milled in normal hardened steel vial set and in ZrO_2 vial set. FeSn_2 and ZrO_2 contaminations were found in obtained nanopowders respectively.

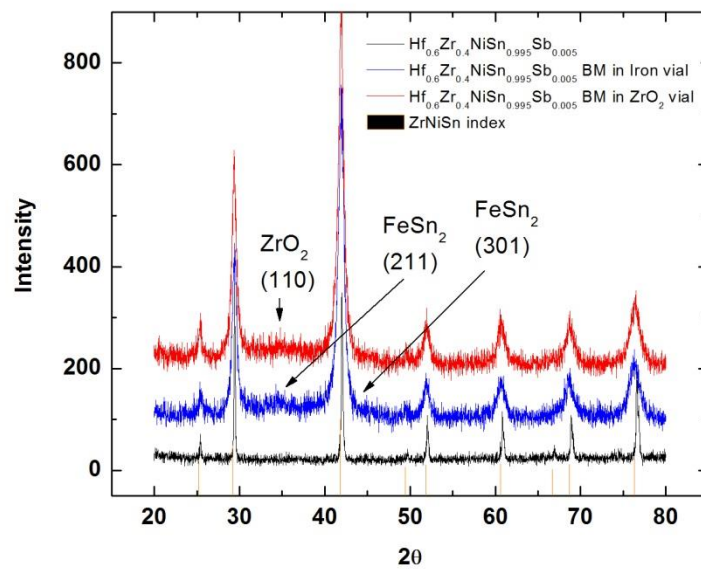


Figure 3-8 X-Ray Diffraction patterns of as-cast Half Heusler $\text{Hf}_{0.6}\text{Zr}_{0.4}\text{NiSn}_{0.995}\text{Sb}_{0.005}$ (black) and corresponding powders that were ball milled in normal iron vial set (blue) and that in ZrO_2 vial set (red) respectively.

3-4 Efforts on thermopower improvement via energy filtering

Low energy charge carriers are believed to be detrimental to the Seebeck coefficient S , thus S could be enhanced if these low energy carriers can be selectively scattered. This concept of S enhancement based on elimination of lower energy charge carriers can be expressed explicitly as:[5]

$$\alpha = -\frac{1}{e\sigma} \int d\varepsilon \frac{\mu - \varepsilon}{T} \sigma(\varepsilon) \left(-\frac{\partial f^0(\varepsilon)}{\partial \varepsilon}\right) \quad (3-6)$$

Where e is the charge of an electron, ε is the energy of a carrier, μ is the chemical potential, $\sigma(\varepsilon)$ is the differential electrical conductivity and $f^0(\varepsilon)$ the Fermi distribution function. Moyzhes and Nemchinsky[78] suggested that the contribution to thermopower from a carrier whose energy is lower than its chemical potential is opposite to that of a carrier whose energy is higher than the chemical potential; thus, the overall thermopower is reduced due to the contrary contribution. Therefore, if transport of low energy carriers can be selectively eliminated by potential barriers, then thermopower S (and hence the dimensionless figure of merit ZT) can be greatly improved. Next, we will estimate the optimal barrier height in order to maximize figure of merit Z .

Considering degenerate semiconductors, the electronic part of figure of merit Z can be expressed as:

$$Z = \frac{\alpha^2}{L_0} \quad (3-7)$$

Where L_0 ($\sim 2 W\Omega K^{-2}$) is the Lorentz number. The electrical conductivity can be written as:

$$\sigma = \int d\varepsilon \sigma(\varepsilon) \left(-\frac{\partial f^0(\varepsilon)}{\partial \varepsilon}\right) \quad (3-8)$$

Now, considering a virtual change of differential electrical conductivity due to potential barrier $\sigma(\varepsilon) \rightarrow \sigma(\varepsilon) + \delta\sigma(\varepsilon)$, the change of figure of merit Z will then be:[79]

$$\delta Z = Z(\sigma(\varepsilon) + \delta\sigma(\varepsilon)) - Z(\sigma(\varepsilon)) = \int_0^\infty d\varepsilon \frac{\delta Z}{\delta\sigma} \delta\sigma(\varepsilon) \quad (3-9)$$

Thus the derivative of Z over $\sigma(\varepsilon)$:

$$\frac{\delta Z}{\delta\sigma} = \frac{2\alpha}{L_0} \frac{\delta\alpha}{\delta\sigma} = -\frac{2\alpha}{L_0\sigma} \left(\frac{\varepsilon - \mu}{eT} + \alpha \right) \left(-\frac{\partial f^0(\varepsilon)}{\partial\varepsilon} \right) \quad (3-10)$$

Combining Eqn (3-9) with Eqn (3-10), the relative change in the figure of merit is then:

$$\frac{\delta Z}{Z} = -\frac{2}{\alpha\sigma} \int_0^\infty d\varepsilon \left(\frac{\varepsilon - \mu}{eT} + \alpha \right) \left(-\frac{\partial f^0(\varepsilon)}{\partial\varepsilon} \right) \delta\sigma(\varepsilon) \quad (3-11)$$

As shown in Figure 3-9, in a classic regime, carriers of energies lower than the potential barrier ε_b are impeded by the barrier, while carriers whose energies are higher than ε_b would penetrate the potential barrier unaffected; in other words, electrical conductivity in this classic regime is:

$$\delta\sigma(\varepsilon) = \begin{cases} -\sigma(\varepsilon), & \text{if } \varepsilon < \varepsilon_b \\ 0, & \text{if } \varepsilon > \varepsilon_b \end{cases} \quad (3-12)$$

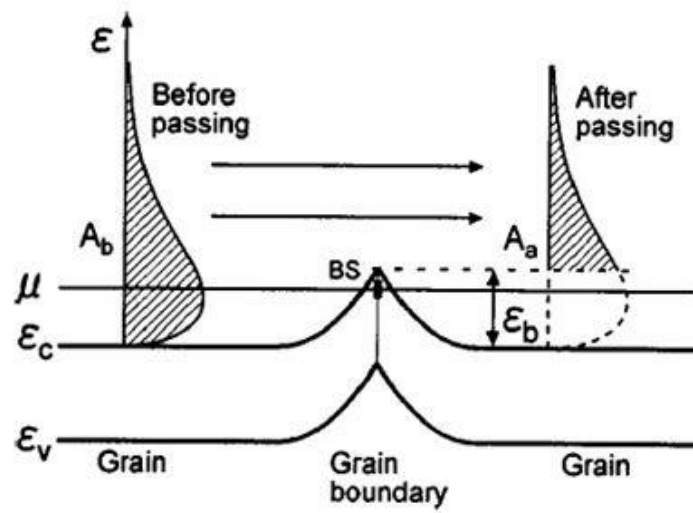


Figure 3-9 The preferential scattering mechanism of charge carriers in conduction band through grain boundary of barrier height ϵ_b .

If we substitute $\delta\sigma(\epsilon)$ of Eqn (3-12) into Eqn (3-11), we will find:

$$\frac{\delta Z}{Z} = \frac{2}{\alpha\sigma} \int_0^{\epsilon_b} d\epsilon \left(\frac{\epsilon - \mu}{eT} + \alpha \right) \left(-\frac{\partial f^0(\epsilon)}{\partial \epsilon} \right) \sigma(\epsilon) \quad (3-13)$$

Only charge carriers with energy ϵ satisfying:

$$\frac{\epsilon - \mu}{eT} + \alpha < 0 \text{ or } \epsilon < \mu - \alpha eT \quad (3-14)$$

will bring a positive change in figure of merit; hence, in order to maximize Z, Eqn (3-14) shall hold true for all $\varepsilon < \varepsilon_b$; this requirement can always be satisfied only if:

$$\varepsilon_b = \mu - \alpha eT \quad (3-15)$$

It can be seen from this equation that the elimination of lower energy charge carriers by the appropriate potential barrier will always lead to enhancement in Z as long as $\varepsilon_b > 0$.

More rigorous treatments on the effect of potential barriers on electrical transport and thermal transport have been well discussed. Impressive enhancement in the power factor [19], [78], [80], [81], [82], together with reduced thermal conductivity, [83] were achieved, resulting in a very promising figure of merit applicable in building TE generators and coolers.

Although precise control of the height and width of potential barriers may be achieved via lower dimensional nanostructuring, due to the relatively complex technique and extremely low yields, researches are mostly focused on three-dimensional nanocomposites.

3-4-1 Monolithic N-type HH nanocomposite

To prepare N-type Half Heusler $\text{Hf}_{0.6}\text{Zr}_{0.4}\text{NiSn}_{0.995}\text{Sb}_{0.005}$, high purity (>99.95%) Hf, Zr, Ni, Sn and Sb elemental pieces were arc melted three times under an argon atmosphere to ensure homogeneity. The obtained ingot was then pulverized using mortar and pestle before being moved to a BM vessel for 15 hours' mechanical alloying. The BM process was conducted under a protecting atmosphere of argon.

The obtained powders were then consolidated with the Spark Plasma Sintering (SPS) technique; the sintering process was held at 1200°C and 60MPa for 2~3 min. The existence of HH single phase was identified via XRD pattern, as shown in Figure 3-10(a). The solidified disk-shaped sample was then polished and fractured for cross section scan under SEM (JEOL 6700F), and another piece was also prepared for TEM (Titan HRTEM) after careful polishing and ion milling. The size of the majority of the grains was found to be around 150~250nm, as shown in Figure 3-11. Smaller nano-patterns (5~10nm) were also found both in the grains and on the grain boundaries. The average thickness of grain boundaries was in the range of 2~5nm.

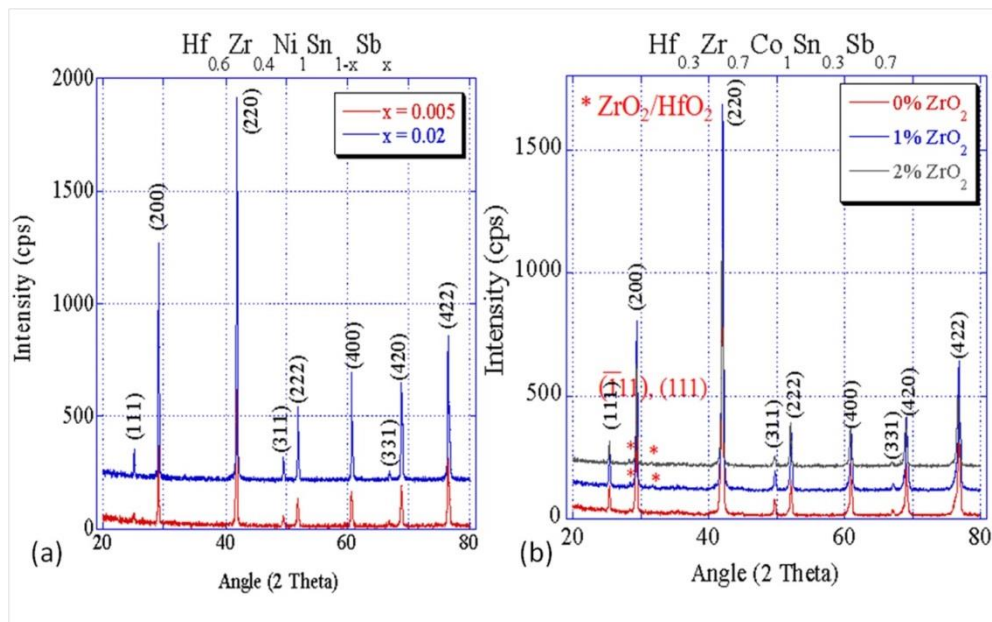


Figure 3-10 X-Ray Diffraction patterns of (a) N-type $\text{Hf}_{0.6}\text{Zr}_{0.4}\text{NiSn}_{1-x}\text{Sb}_x$ ($x=0.005, 0.02$) and (b) P-type $\text{Hf}_{0.3}\text{Zr}_{0.7}\text{CoSn}_{0.3}\text{Sb}_{0.7}$ with ZrO_2 impurities.

Charge carriers' transportation in a polycrystalline bulk can be divided into two phases: one inside the grains, the other through the grain boundaries which are somewhat amorphous unlike the crystalline grains. These thin grain boundary layers act as potential barriers; thus, carriers with low energy (which is insufficient to penetrate the barriers) would be excluded from the heat transport process. Although filtering lower energy charge carriers result in the enhancement of thermopower, it can also lead to a reduction of electrical conductivity (or an increase of electric resistivity); therefore, the overall power factor may not be benefited. As depicted in Figure 3-12, the Seebeck coefficient was increased by up to 13% at 750°C from $-199\mu\text{V/K}$ to $-224\mu\text{V/K}$, while electrical conductivity was reduced by 35% at the same temperature.

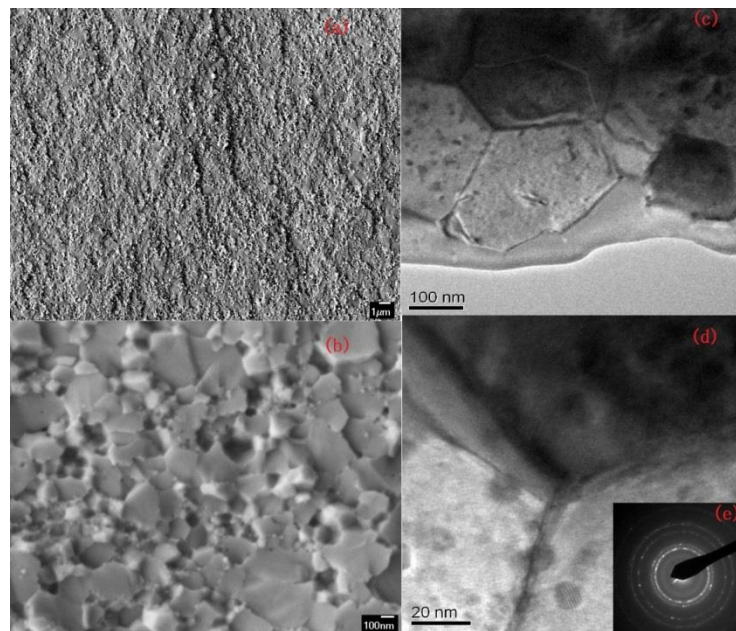


Figure 3-11 (a)(b) SEM scanning, (c)(d) TEM scanning and (e) Selected Area Diffraction pattern on 15hrs Ball Milled N-type $\text{Hf}_{0.6}\text{Zr}_{0.4}\text{NiSn}_{0.995}\text{Sb}_{0.005}$ alloy.

Without considering the reduction in thermal conductivity, an overall 15% reduction in Power Factor S^2T/ρ was obtained as shown in Figure 3-13, mainly due to the significantly reduced carrier concentration by potential barrier scattering. A simple model can be utilized to demonstrate the reduction of total electrical conductivity across potential barriers (grain boundaries):[81]

$$\frac{L_{total}}{\sigma_{total}} = \frac{L_{grain}}{\sigma_{grain}} + \frac{L_{gb}}{\sigma_{gb}} \quad (3-16)$$

Where “total” represents the overall carrier transportation, “grain” represents carrier transportation inside grains, and “gb” represents transportation through grain boundaries. L is the length scale. Within classical regime, low energy charge carriers ($\epsilon < \text{barrier height } \epsilon_b$) will be confined within grains and thus do not contribute to electrical conductivity. In the case of $\sigma_{gb}(\epsilon) = \sigma_{grain}(\epsilon)$ for $\epsilon \geq \epsilon_b$, and $L_{grain} + L_{gb} = L_{total}$, from Eqn (3-16):

$$\Sigma_{total} = \int_0^{\infty} d\epsilon \sigma_{total}(\epsilon) f(\epsilon) = \int_{\epsilon_b}^{\infty} d\epsilon \sigma_{grain}(\epsilon) f(\epsilon) < \int_0^{\infty} d\epsilon \sigma_{grain}(\epsilon) f(\epsilon) = \Sigma_{grain}$$

(3-17)

This simplified calculation reveals the fact that the overall electrical conductivity is always reduced as long as low energy carriers are filtered by potential barriers.

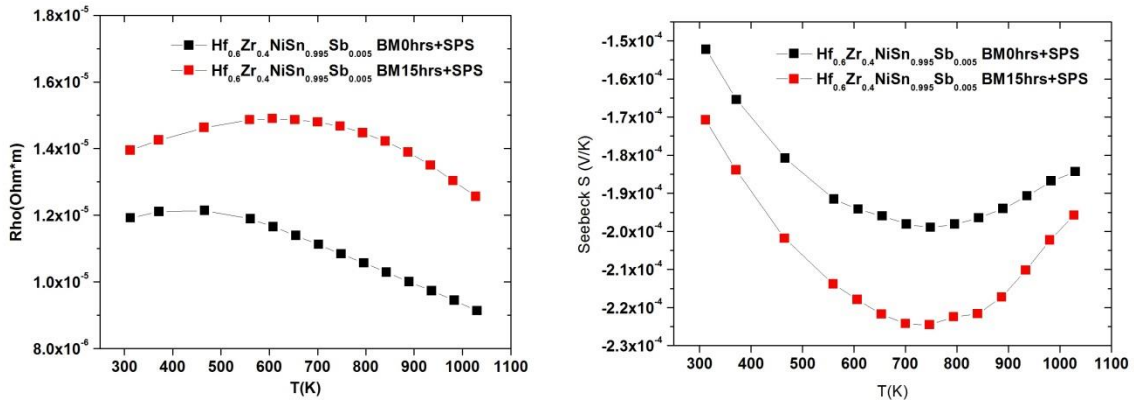


Figure 3-12 Measured electrical resistivity (Ohm*m) and thermopower S (V/K) of N-type Half Heusler $\text{Hf}_{0.6}\text{Zr}_{0.4}\text{NiSn}_{0.995}\text{Sb}_{0.005}$ which was SPSed at 1000°C after 15 hours BM (red square), compared with the properties of its bulk counterpart (black square).

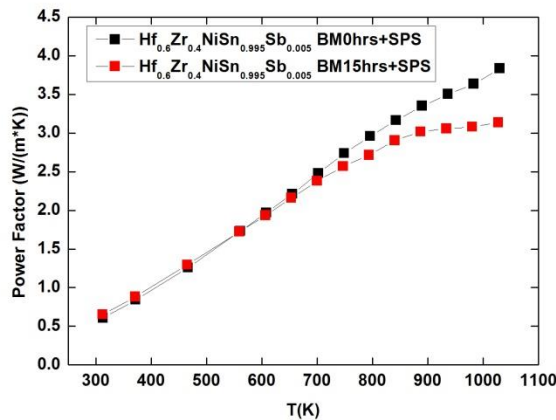


Figure 3-13 Power factor S^2T/ρ dependent on temperature in monolithic nanostructured $\text{Hf}_{0.6}\text{Zr}_{0.4}\text{NiSn}_{0.995}\text{Sb}_{0.005}$.

Neophytou *et al.*[81] have made use of similar treatment in Si nanowires system and suggested that the reduction of electrical conductivity due to barrier potential scattering would not diminish until the Fermi level was increased high enough for the carriers to be thermionically emitted over the potential barriers, and enhanced Fermi level can be achieved via heavier doping. Although increasing the doping level normally leads to a reduction in thermopower S , the combined effect of energy filtering and increased carrier concentration would still get to an optimal point where the overall power factor ($PF=S^2\sigma T$) can be enhanced. In the N-type HH system, increasing the Sb doping level from 0.5% to 1%~2%, while keeping grain size and grain boundary thickness constant, may be an effective means to achieve overall enhancement of the Power Factor. Too high a doping level will not result in further enhancement of the TE properties. On one hand, increasing the doping level eventually leads to enlarged bipolar effect detrimental to thermopower S ; on the other hand, according to the Wiedemann-Franz law, electrical thermal conductivity $\kappa_e=L_0\sigma T$ would increase as σ goes up, resulting in an overall higher thermal conductivity.

Beside the dependence of thermoelectric properties on barrier height, the dependence of thermopower on the density of potential barriers was also discussed by Nishio and Hirano.[79]

3-4-2 Nanoparticles embedded in P-type bulk HH

In addition to monolithic nanostructures, nanocomposites constructed by implementing nanoparticles into bulk materials externally or nanocomposites with in-situ formed secondary phases are

also commonly used. The embedded nanoparticles not only serve as scattering centers of phonons and charge carriers, but are also able to suppress the grain growth of matrix materials.

In this section, ZrO₂ nanoparticles (grain size ~80nm) dispersed P-type HH Hf_{0.3}Zr_{0.7}CoSn_{0.3}Sb_{0.7} nanocomposites were synthesized. First, bulk ingots of Hf_{0.3}Zr_{0.7}CoSn_{0.3}Sb_{0.7} were fabricated from elemental pieces in an argon atmosphere using the arc melting technique; the obtained ingots were then pulverized and hand ground to micron size with mortar and pestle. Next, commercially available high purity ZrO₂ nanopowders were added into micron-sized HH powders and hand ground for 10 minutes to allow for homogeneous mixing; another 15 minutes of BM was also applied to further disperse these ZrO₂ nanopowders into matrix materials. The mixed powders were eventually consolidated with Spark Plasma Sintering, with sintering temperature of 1200°C and pressure of 60MPa.

The existence of the oxide phase was identified via XRD peaks shown in Figure 3-10b. Scanning electron microscope (SEM, JEOL 6700F) and transmission electron microscope (TEM, JEOL 2000FX) were also employed to study their morphologies and microstructures. Energy dispersive spectroscopy (EDS) line scan further confirmed the existence of the oxide particles as well the homogeneity of samples.

In Figure 3-10(b), the existence of an impurity oxide phase can be identified, however, the exact composite is still pending, due to the similar crystal structure and lattice constant of HfO₂ and ZrO₂; thus, further scanning under TEM and SEM is necessary.

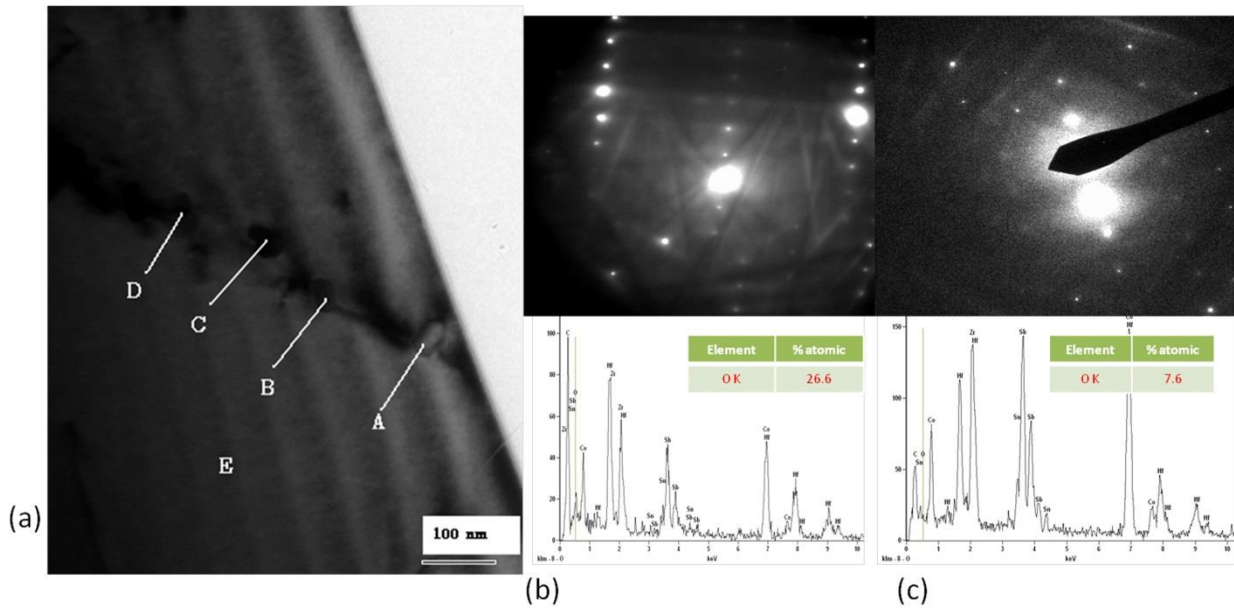


Figure 3-14 (a) Microstructure of P-type HH $\text{Hf}_{0.3}\text{Zr}_{0.7}\text{CoSn}_{0.3}\text{Sb}_{0.7}$ under TEM, and selected area diffraction as well as corresponding EDS at (b) nanoparticle B (c) matrix area E.

Presented in Figure 3-14(a) are TEM images of $\text{Hf}_{0.3}\text{Zr}_{0.7}\text{CoSn}_{0.3}\text{Sb}_{0.7}$ bulk which was dispersed with 2 vol.% ZrO_2 nanoparticles. Nanograins of 50 to 80 nm in size can be found at the boundaries of HH grains, meanwhile, nanoparticles as large as 200-300 nm in size were also detected. Select area diffraction patterns as well as energy dispersive spectroscopy at spots B (nanoparticle) and E (main matrix), as shown in Figures 3-14(b) and 3-14(c), further confirmed that these nanoparticles were indeed oxides and they had different crystal structures than the matrix.

The morphological structure of the same nanocomposite were studied under SEM and shown in Figures 3-15(a) and 3-15(b). The typical grain size of host material was in the range of 5-25 μm , while that of nanoinclusions fell between 80 and 250 nm. The ZrO_2 coagulations ($\sim 250\text{nm}$) were probably due

to insufficient mixing during BM. The EDS patterns shown in Figure 3-15(c) indicate that the composition of the nanoinclusions is mainly HfO_2 , since the contents of Hf and O always peak synchronously whenever the line scan crosses a nanoparticle.

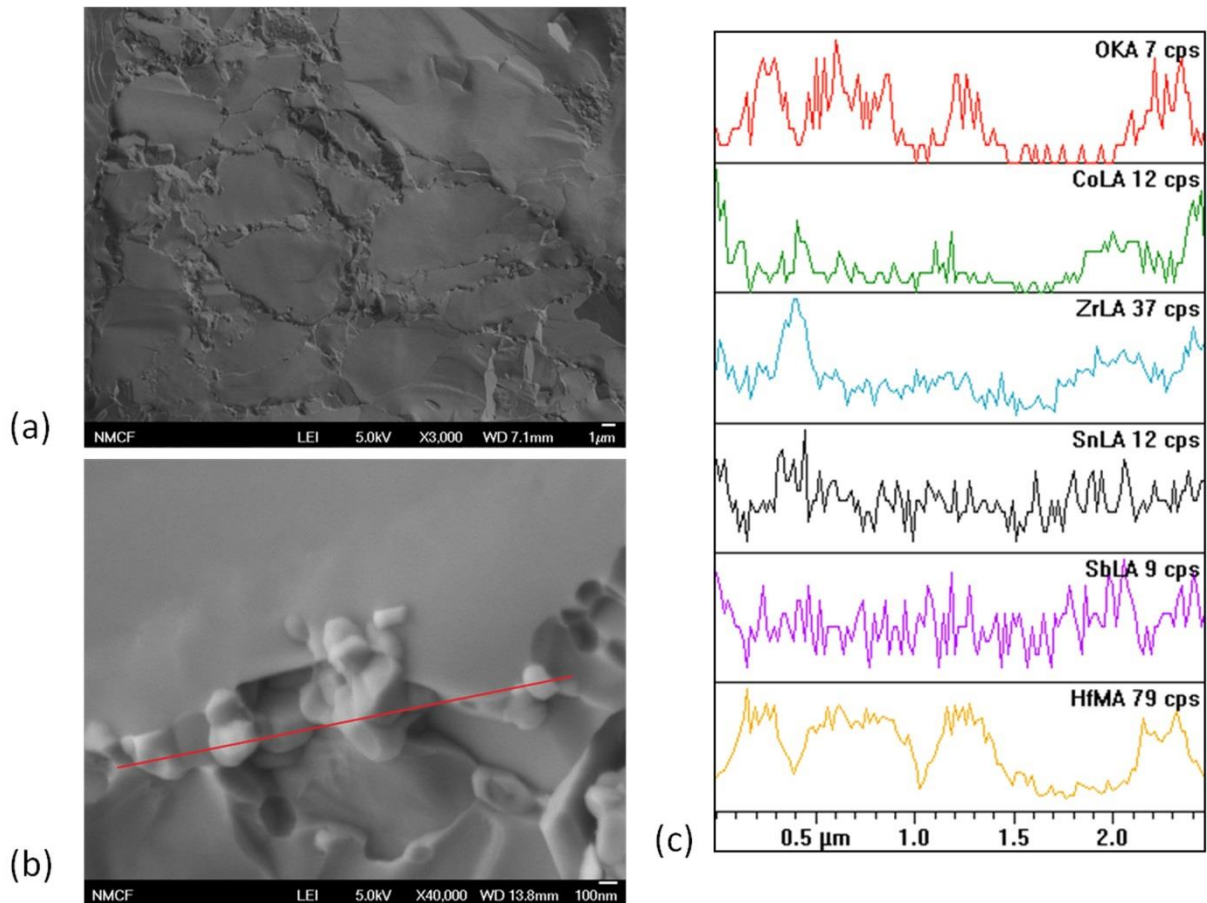


Figure 3-15 (a)(b) SEM scanning of fractured P-type HH $\text{Hf}_{0.3}\text{Zr}_{0.7}\text{CoSn}_{0.3}\text{Sb}_{0.7}$, and (c) energy dispersive spectroscopy line scan along the path shown in (b).

The extra grain boundaries introduced by HfO_2 nanoparticles serve as potential barriers that impede the transport of charge carriers with lower energies, hence reducing the electrical conductivity and enhancing the thermopower. Both effects were experimentally verified, as presented in Figure 3-15. Compared with monolithic N-type HH nanocomposite, the density of grain boundaries in 2% ZrO_2 dispersed P-type HH nanocomposite is much less; hence, the electrical and thermal transports are less affected, specifically lower energy charge carriers will eventually find their way through the potential barriers by detour in this three dimensional nanocomposite, especially when the intensity of potential barriers is dilute.

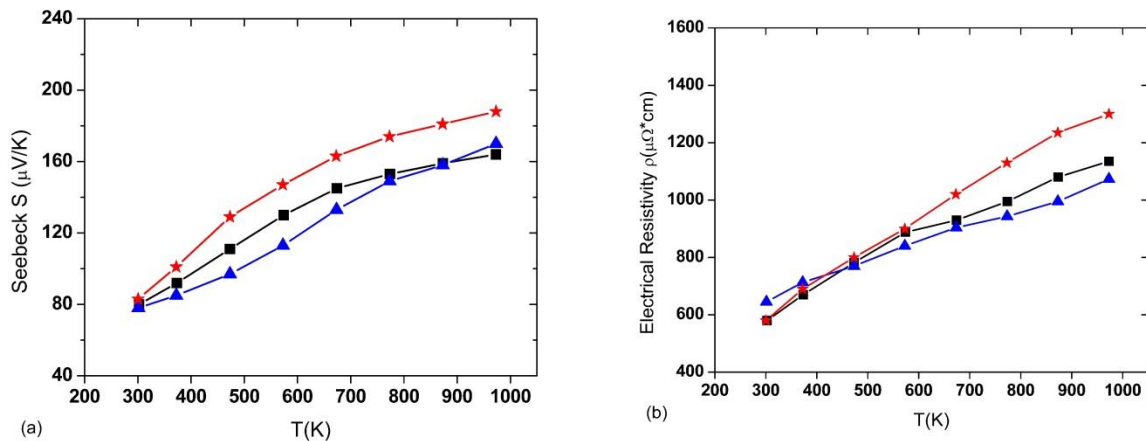


Figure 3-16 (a) Thermopower S ($\mu\text{V}/\text{K}$) and (b) Electrical resistivity ρ ($\mu\Omega\cdot\text{cm}$) of P-type $\text{Hf}_{0.3}\text{Zr}_{0.7}\text{CoSn}_{0.3}\text{Sb}_{0.7}$ with 0% (black square), 1% (blue triangle) and 2% (red star) ZrO_2 nanoparticles.

It is getting harder for the low energy carriers to detour as the concentration of potential barriers (nanoparticles) continues to increase. Both the thermopower S and the electrical resistivity ρ showed

little change as the nominal volume fraction of HfO_2 nanoparticles increased from 1% to 2%, as depicted in Figure 3-16. However, as the volume fraction increased to 4%, a sudden increase in S and a reduction in σ were observed, indicating that at this point energy filtering began to have an obvious effect. Considering that HfO_2 is actually an insulator with a wide band gap, as its concentration increases, the benefit gained in thermopower S will be far less than the loss in electrical conductivity σ ; thus, the overall Power Factor ($\text{PF} = S^2 \sigma T$) will be reduced rather than enhanced. In order to minimize the electrical conductivity reduction, the implemented nano-phase should ideally have a higher carrier mobility to compensate the reduced carrier concentration, as well as a slightly wider band gap to form proper potential barriers to filter low energy charge carriers.

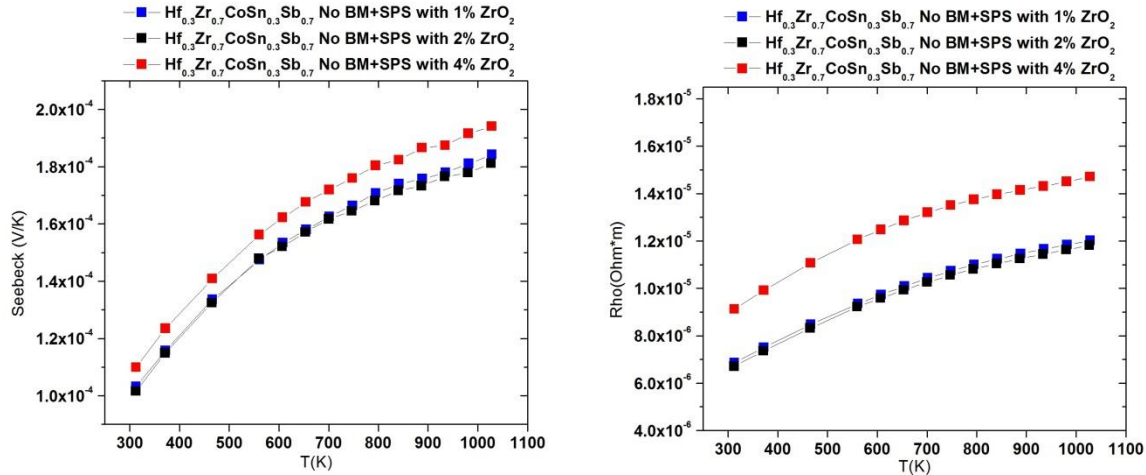


Figure 3-17 Seebeck coefficient and electrical resistivity of nominal 1%, 2% and 4% ZrO_2 dispersed P-type HH $\text{Hf}_{0.3}\text{Zr}_{0.7}\text{CoSn}_{0.3}\text{Sb}_{0.7}$.

3-5 Reduction of thermal conductivity

The introduction of nano-scale features not only affects the charge carriers' transport, resulting in changes in thermopower and electrical conductivity, but also provides extra phonon scattering centers, leading to a reduction in the lattice thermal conductivity. According to Callaway[57] and Peacor *et al.*[84], lattice thermal conductivity can be expressed as:

$$\kappa_L = \frac{k_B}{2\pi^2 v_s} \left(\frac{k_B T}{\hbar} \right) \int_0^{\theta_D/T} dx \frac{x^4 e^x}{\tau_{ph}^{-1} (e^x - 1)^2} \quad (3-18)$$

Where x is the reduced phonon frequency $x = \hbar\omega/k_B T$, and τ_{ph} is the relaxation time, which consists of three components and can be expressed with Matthiessen's rule:

$$\tau_{ph}^{-1} = \tau_I^{-1} + \tau_U^{-1} + \tau_{GB}^{-1} = A\omega^4 + B e^{-\theta_D/T} T^3 \omega^2 + v_s/d \quad (3-19)$$

τ_I^{-1} ($\sim\omega^4$) represents impurity scattering due to mass fluctuation (density/strain), the second term τ_U^{-1} ($\sim\omega^2$) is Umklapp scattering involving multiple-phonon interactions, and the last term ($\sim\omega^0$) stands for phonon's grain boundary scattering with group velocity v_s and grain size d . Parameter A and parameter B are constant for a certain composite. For a polycrystalline bulk sample with grain size $\sim 10^{-5}$ m, the third term is estimated to be $10^3 \text{ m/s} / 10^{-5} \text{ m} = 10^8 \text{ s}^{-1}$, it can be seen that grain boundary scattering term is almost constant at all temperatures. At temperatures far below the Debye temperature, boundary scattering and impurity scattering dominate, while the temperature is around or above Debye temperature, the grain boundary scattering no longer plays that important a role in obstructing phonon

transport; since the Umklapp term increases quickly with T. However, if the grain size d can be reduced to 10~100nm or 10^{-8} ~ 10^{-7} m, grain boundary scattering will be still decisive in reducing lattice thermal conductivity even at high temperature range.

3-5-1 Monolithic nanocomposite

This section will focus on monolithic $\text{Hf}_{0.6}\text{Zr}_{0.4}\text{NiSn}_{0.995}\text{Sb}_{0.005}$ nanocomposite, the synthesis process has been described in detail in section 3-4-1. The obtained grain size after BM and SPS consolidation is around 150 to 250 nm. Lattice thermal conductivity was derived with $\kappa_{\text{ph}} = \kappa_{\text{total}} - \kappa_{\text{e}}$, where electronic contribution to thermal conductivity $\kappa_{\text{e}} = L_0 \sigma T$, according to the Wiedemann-Franz law. For metals or degenerated semiconductors, Lorentz constant $L_0 = 2.45 \times 10^{-8}$ ($\text{W}\Omega\text{K}^{-2}$). Compared with its bulk form with micron-sized grains, the lattice thermal conductivity of the nanostructured form was found to be lower in all temperature range from 300K to 1050K. At lower temperatures (~300K), the reduction effect of lattice thermal conductivity via grain boundary scattering was more obvious, since the constant relaxation time τ_{GB}^{-1} is still comparable with the Umklapp scattering term τ_{u}^{-1} . As presented in Figure 3-18, when the temperature increases, the difference between the lattice thermal conductivity of the bulk and nanostructured forms eventually diminished; this is because, at this point, it is the Umklapp scattering that dominates phonon transport, while the contribution of grain boundary scattering is negligible.

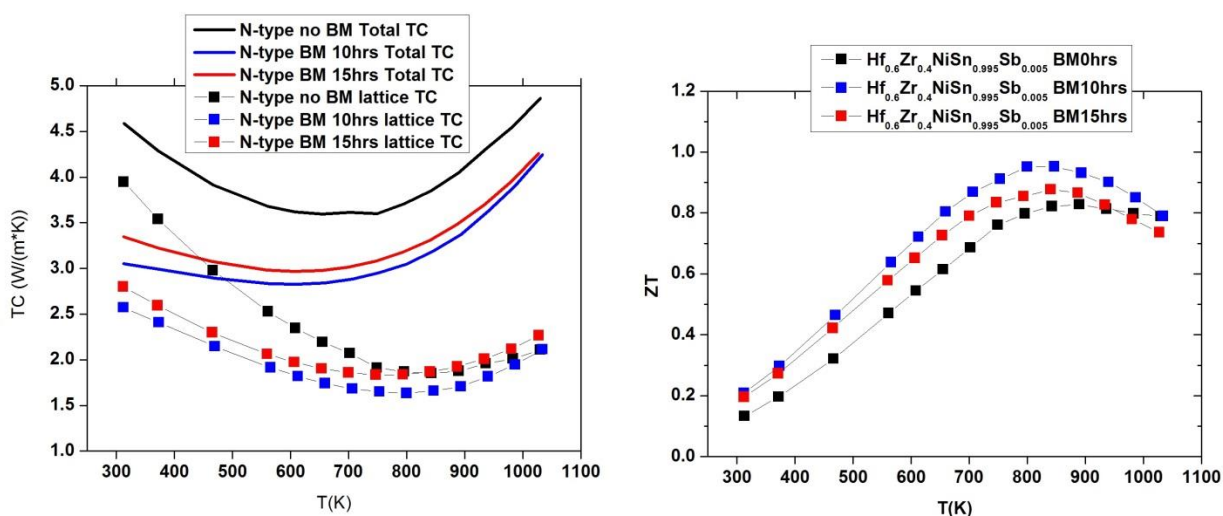


Figure 3-18 (a) Total thermal conductivity (solid lines) and lattice thermal conductivity (solid squares) (b) figure of merit ZT of N-type HH $\text{Hf}_{0.6}\text{Zr}_{0.4}\text{NiSn}_{0.995}\text{Sb}_{0.005}$ with 0hr (black), 10hrs (blue) and 15hrs (red) Ball Milling time.

3-5-2 Nanoparticles embedded in bulk

ZrO_2 nanoparticles of 1%, 2% and 4% nominal volume fractions were dispersed into P-type HH $\text{Hf}_{0.3}\text{Zr}_{0.7}\text{CoSn}_{0.3}\text{Sb}_{0.7}$ bulk, as described in section 3-4-2. It was found, as shown in Figure 3-15(b) and Figure 3-14(a), that most of the HfO_2 (due to Zr-Hf exchange with host material) nanoparticles (~80nm) lay at matrix grain boundaries. No obvious reduction in lattice thermal conductivity was observed upon ZrO_2 nanoparticle dispersion, except for the nominal 2% ZrO_2 dispersed nanocomposite. According to the experimental results, [85], [86] even a small volume percentage of nanoparticles would cause a considerable reduction in lattice thermal conductivity. In our case, as shown in Figure 3-19, the

unconspicuous change in lattice thermal conductivity is either because the embedded HfO_2 nanoparticles have aggregated into larger micron-sized precipitates or because the nanopowders were not thoroughly dispersed into matrix; in either event, the role of added nanoparticles as phonon scattering centers was weakened.

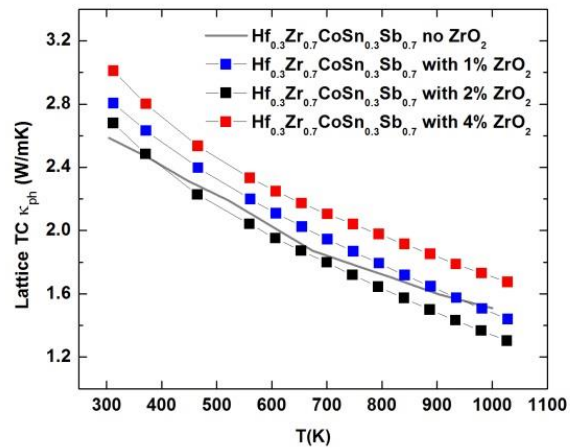


Figure 3-19 Lattice thermal conductivity of P-type HH $\text{Hf}_{0.3}\text{Zr}_{0.7}\text{CoSn}_{0.3}\text{Sb}_{0.7}$ bulk (grey) and corresponding nanocomposites with 1% (blue), 2% (black) and 4% ZrO_2 nanoparticles.

Although further increase of ZrO_2 content might result in lower lattice thermal conductivity, it is nevertheless the case, as discussed in section 3-4-2, that too large a ZrO_2 volume fraction would lead to an extremely high electrical resistivity, which is unlikely to be compensated by the possible enhancement gained by thermopower and reduction gained in thermal conductivity. Actually, 2% ZrO_2

was found to be the optimal volume fraction, which eventually leads to an overall improvement in figure of merit ZT, as can be seen in Figure 3-20.

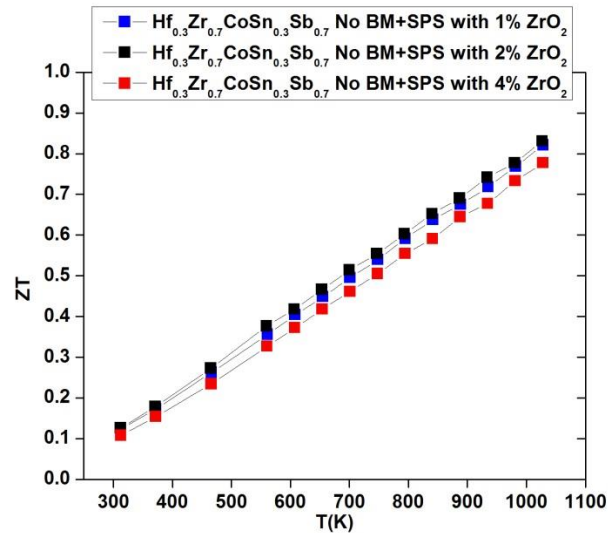


Figure 3-20 The dependence of figure of merit ZT on temperature in 1%, 2% and 4% ZrO₂ dispersed Hf_{0.3}Zr_{0.7}CoSn_{0.3}Sb_{0.7}.

3-6 Mass Fluctuation Effect on Lattice Thermal Conductivity

To analyze the mass fluctuation effect, one should recall the impurity scattering term of relaxation time as expressed in Eqn (3-19), $\tau_i^{-1} = A\omega^4$. According to Callaway[57] and Klemens,[87] the composition dependent constant A can be expressed as:

$$A = \frac{V_0}{4\pi c^3} \sum_i f_i (M_i - M)^2 \quad (3-20)$$

Where V_0 is the volume per atom, M_i is the mass of atom i , f_i is the fraction of atoms with mass M_i , and M is the average atom mass. This effective medium approach, was also adopted by Mingo *et al.*[88] to evaluate parameter A in a two-phase heterogeneous system, in which case, A is expressed as:

$$A = \frac{V_0}{4\pi c^3} (1 - x)x \left[\frac{M_1 - M_2}{M} \right]^2 \quad (3-21)$$

Regardless of the expression of A , a maximal $\tau_l^{-1} = A\omega^4$ shall be achieved at certain ratio of constituents, this maximum of τ_l^{-1} corresponds to the lowest lattice thermal conductivity that can be obtained solely by mass fluctuation.

In N-type Half Heusler $\text{Hf}_{0.6}\text{Zr}_{0.4}\text{NiSn}_{0.995}\text{Sb}_{0.005}$, Hf atoms can be replaced by Zr or Ti atoms within the same group in periodic table. The mass difference between Hf and Ti is the largest, therefore, the mass fluctuation parameter A shall be increased if some heaviest Hf atoms are to be replaced by the lightest Ti atoms, in this way, a reduced lattice thermal conductivity can be expected. Experiments have been performed on $\text{Hf}_{0.6}\text{Zr}_{0.4}\text{NiSn}_{0.995}\text{Sb}_{0.005}$; upon 10% and 20% Hf being replaced by Ti atoms, the lattice thermal conductivity was reduced consistently at all temperatures ranging from 300K to 1050K. The different behaviors between lattice thermal conductivity reduction caused by grain boundary scattering as shown in Figure 3-18 and that caused by mass fluctuation as shown in Figure 3-21 can be ascribed to their different frequency dependences; while τ_{GB}^{-1} stays constant as temperature increases, τ_l^{-1} increases with the fourth power of phonon frequency ω . At high temperatures, most phonons are

populated close to the Brillouin zone boundary (the high frequency region), thus, the contribution of mass fluctuation τ_l^{-1} increases; while the contribution of grain boundary scattering τ_{GB}^{-1} stays constant. Considering the dominating Umklamp scattering is increasing as temperature goes up, the relative contribution of mass fluctuation to phonon scattering may stay unchanged, while the relative contribution of grain boundary scattering will significantly decrease. Although a lower lattice thermal conductivity has been achieved upon replacing a certain percentage of Hf atoms with lighter Ti atoms, severe degradation in thermopower results in an reduction in power factor, eventually leading to an overall lower dimensionless figure of merit ZT at high Ti doping levels. It was found that only when 10% Hf atoms were replaced by Ti atoms, was a higher overall ZT observed, as shown in Figure 3-22.

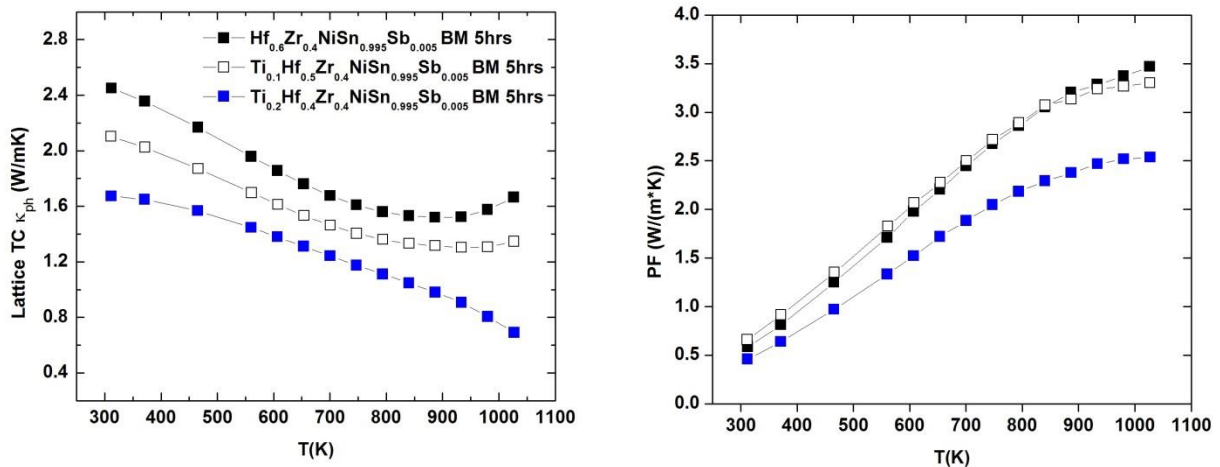


Figure 3-21 Lattice thermal conductivity and power factor of nanostructured $\text{Hf}_{0.6}\text{Zr}_{0.4}\text{NiSn}_{0.995}\text{Sb}_{0.005}$ with 0% (black), 10% (white), and 20% (blue) Hf atoms replaced by smaller Ti atoms.

3-7 Conclusions

Vanadium doped Half Heusler $\text{Hf}_{0.75}\text{Zr}_{0.25}\text{NiSn}$ alloys were fabricated with the arc melting technique. Enhancement of the Seebeck coefficients were observed from 300K to 600K, which was explained by the localized increase of Density of States (DOS) at the Fermi level due to the state resonance of impurity orbits and matrix band edges. Evidence of the density of states increase at the Fermi level E_F was eventually exhibited by low temperature specific heat measurements.

Nanostructured N-type $\text{Hf}_{0.6}\text{Zr}_{0.4}\text{NiSn}_{0.995}\text{Sb}_{0.005}$ and P-type $\text{Hf}_{0.3}\text{Zr}_{0.7}\text{CoSn}_{0.3}\text{Sb}_{0.7}$ Half Heusler alloys were synthesized with arc melting, mechanic alloying and SPS consolidation. While N-type $\text{Hf}_{0.6}\text{Zr}_{0.4}\text{NiSn}_{0.995}\text{Sb}_{0.005}$ was a monolithic nanostructure with grain size around 150 to 250 nm, P-type $\text{Hf}_{0.3}\text{Zr}_{0.7}\text{CoSn}_{0.3}\text{Sb}_{0.7}$ bulk was implemented with inert ZrO_2 nanoparticles, which mostly stayed at matrix grain boundaries and evidenced by EDS line scan and SEM. A remarkable increase in the density of grain boundaries was generated upon introducing these nanostructured features. The effect of low energy charge carriers being selectively scattered by additional grain boundaries on thermopower S and electrical conductivity σ was then discussed in both monolithic N-type and ZrO_2 dispersed P-type nanostructured Half Heusler alloys. The increased density of grain boundaries in nanostructured alloys also prompted a significant decrease in lattice thermal conductivity due to the additional phonon grain boundary scattering. A phenomenological effective medium method will be introduced to quantitatively calculate the reduction in lattice thermal conductivity of various nanostructures in Chapter 5.

Finally, the mass fluctuation effect was applied to further reduce the lattice thermal conductivity. The mechanism was discussed using the Callaway model. A consistently lower lattice thermal conductivity was observed in N-type $\text{Hf}_{0.6}\text{Zr}_{0.4}\text{NiSn}_{0.995}\text{Sb}_{0.005}$ upon 10% and 20% Hf atoms being replaced by lighter Ti atoms.

Overall, the highest dimensionless figure of merit of $ZT=1.0$ for N-type HH was achieved at 850K in monolithic nanocomposite $\text{Ti}_{0.1}\text{Hf}_{0.5}\text{Zr}_{0.4}\text{NiSn}_{0.995}\text{Sb}_{0.005}$ as the result of combining nanostructuring and mass fluctuation, while $ZT=0.85$ for P-type HH was achieved at 1050K in 2% ZrO_2 dispersed $\text{Hf}_{0.3}\text{Zr}_{0.7}\text{CoSn}_{0.3}\text{Sb}_{0.7}$ solely via nanostructuring technique, as shown in Figure 3-22.

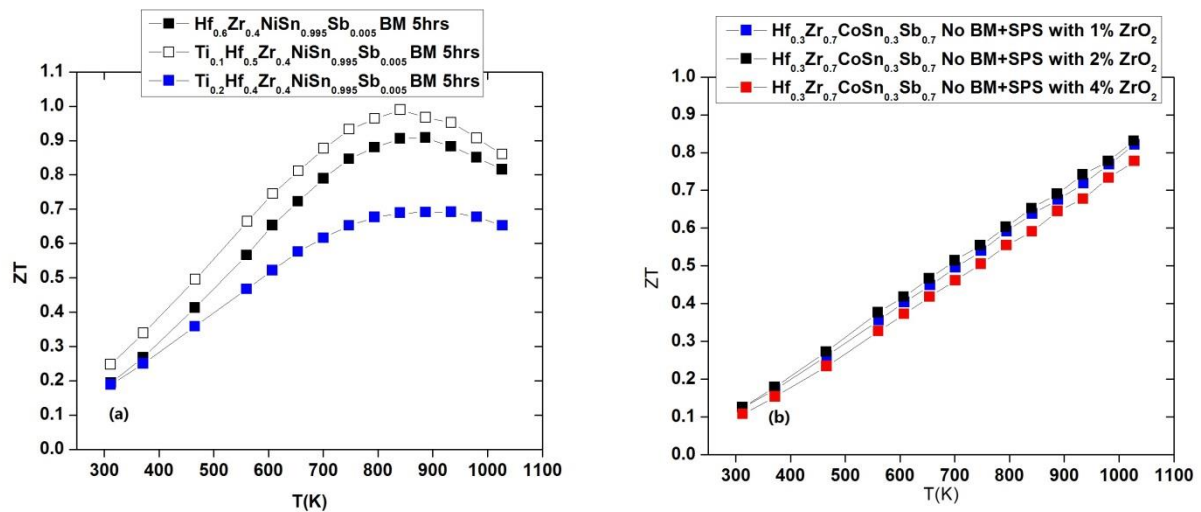


Figure 3-22 Figure of merit ZT achieved of Half Heusler alloys (a) N-type: $ZT=1.0$ at 850K in monolithic $\text{Ti}_{0.1}\text{Hf}_{0.5}\text{Zr}_{0.4}\text{NiSn}_{0.995}\text{Sb}_{0.005}$ (b) P-type: $ZT=0.85$ at 1050K in 2% ZrO_2 nanoparticles dispersed $\text{Hf}_{0.3}\text{Zr}_{0.7}\text{CoSn}_{0.3}\text{Sb}_{0.7}$.

4. Nanostuctured silicon germanide as prospective thermoelectrics

Silicon germanide ($\text{Si}_{1-x}\text{Ge}_x$, $x=0\sim 1$) is one of the most widely studied and applied thermoelectric materials for power generation at high temperatures above 800°C . It has been used in Radioisotope Thermoelectric Generators (RTGs) powering NASA space crafts since 1976.[16] Besides thermoelectric performance, SiGe alloys also have many merits including high mechanical strength, high melting point, low vapor pressure, and excellent resistance to oxidization; therefore, they are of great interest for industrial waste heat recovery, the auto industry and solar thermopower plants.

The milestone of dimensionless figure of merit ZT for n-type bulk $\text{Si}_{1-x}\text{Ge}_x$ is P-doped $\text{Si}_{80}\text{Ge}_{20}$ with $ZT\sim 1$:[16] for p-type bulk, it is B-doped $\text{Si}_{80}\text{Ge}_{20}$ with $ZT\sim 0.5$.[89] The obvious lower ZT of p-type $\text{Si}_{80}\text{Ge}_{20}$ can be largely attributed to the comparably lower carrier mobility of holes than that of electrons in its n-type analogue. It was not until recently, when nanostructuring techniques were introduced to thermoelectrics fabrication, that significant higher ZT s were reported for SiGe with n-type $ZT\sim 1.3$, p-type ~ 0.95 by the Boston College group.[17], [21] The improvement is primarily the result of dramatic reduction in lattice thermal conductivity in nanostructured form due to the much more intense phonon interface scattering than in bulk form. However, the fabrication processes have rarely been discussed in detail, and, as we will present in this chapter, the TE properties are very sensitive to the consolidation parameters (sintering temperature, pressure and holding time); thus, only an optimized synthesis process will lead to the optimal figure of merit ZT , whereas a deviation in fabrication process might cause

severely degraded TE properties. Novel core-shell structures were also fabricated using the wet method by collaborator Nanosonic Inc., and the dramatic reduction in lattice thermal conductivity was observed.

4-1 Synthesis of samples

A fine powder mixture of Silicon (100mesh), Gemernium (200mesh) and Phosphorous or Boron (50mesh) of 5~10 grams was loaded into a 440C stainless steel vial, together with two 0.5” and four 0.25” 440C ultra hard stainless steel balls. The process was performed in a glove box at argon atmosphere. The vial was then sealed and positioned in a SPEX 8000D vibrational mixer, which was then seated in a sealed aluminum box filled with argon. The BM processes were paused for half an hour every three hours to avoid overheating. Dodecane was also introduced to reduce the cold welding between loaded powders and the vial’s inner wall. The obtained nanopowders were removed from the grinding vials in the glove box after the BM process was complete. At this point, the powders should be either stored for future use in an inert atmosphere to avoid oxidization or consolidated immediately with Spark Plasma Sintering technique. SPS temperature and holding time were varied to study the dependence of TE properties on condensing parameters, while sintering pressure was kept constant at 60MPa.

4-2 Grain size vs. BM time

To investigate the effect of BM time on obtained grain size, n-type $\text{Si}_{80}\text{Ge}_{20}\text{P}_2$ nanopowders were prepared under the same grinding conditions, using vibrational BM for both 5 hours and 15 hours separately. The obtained nanopowders were then examined under TEM. The size of the nanoparticles after five hours of ball milling varied from 30nm to 300nm, as shown in Figure 4-1(a). In Figure 4-1(b), under a higher magnification it was found that the large nanoparticles were actually aggregates of finer crystalline grains of 10nm~30nm. Figure 4-1(c) provides a better image of the fine grains composing the larger aggregates. The inset is the selected area electron diffraction pattern (SAED) on a dark large grain, which confirmed that the dark grains were aggregates of smaller multicrystalline grains. Nanoparticles, after 15 hours of ball milling, showed little difference in grain size from those that were ball milled for only 5 hours, as shown in Figure 4-2; similar aggregates of finer grains were also found.

The disability of extending ball milling time to further reduce grain size could be attributed to the size of the grinding balls, which may have been comparably too large ($0.5'' \times 2 + 0.25'' \times 4$); or the high energy vibration ball mill process is so effective that the pulverizing limit has been reached within 5 hours. Now that BM limit can be reached in 5 hours, to avoid possible contamination in a long term ball milling process and to further reduce the grain size, 5 hours BM time and smaller grinding balls are thus suggested in the future work.

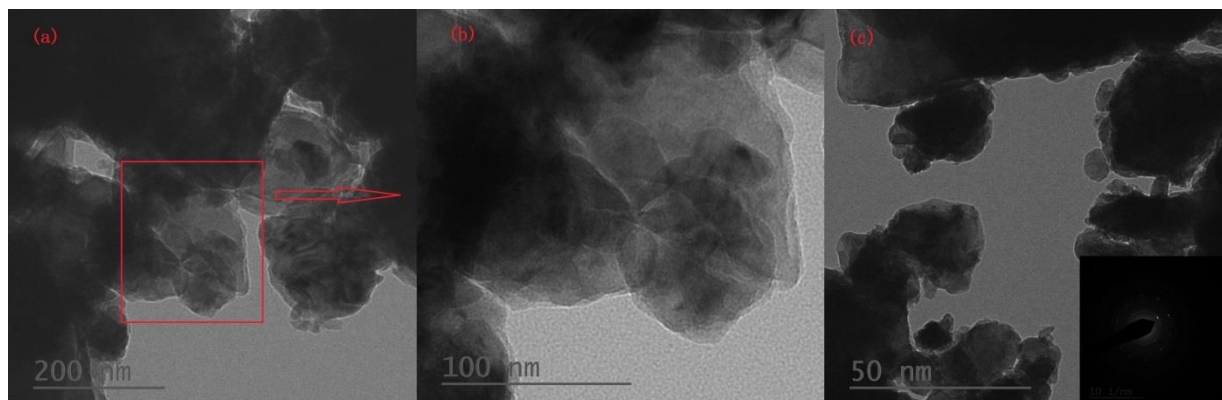


Figure 4-1 TEM images of nanoscaled aggregates in $\text{Si}_{80}\text{Ge}_{20}\text{P}_2$ nanopowders which were ball milled 15 hours.

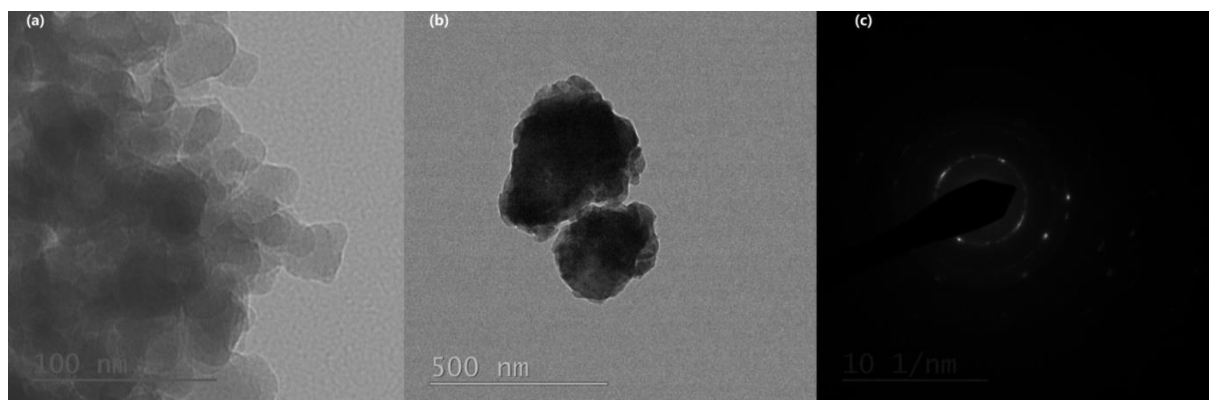


Figure 4-2 TEM images of nanoscaled aggregates in $\text{Si}_{80}\text{Ge}_{20}\text{P}_2$ nanopowders which were ball milled 15 hours.

4-3 Porosity vs. sintering temperature

To investigate the effect of sintering temperature on the microstructure of consolidated samples, $\text{Si}_{80}\text{Ge}_{20}\text{P}_2$ nanopowders that have been ball milled for 15 hours were then SPS compressed at 900°C, 1000°C and 1100°C, separately, with the same pressure (60MPa) and holding time. Mass densities were measured using the Archimedes method and found to be 2.89 g/cc, 2.94g/cc and 3.03g/cc respectively. In comparison with the theoretical density of 2.98g/cc, samples condensed at 900°C and 1000°C showed somewhat porous features. The porosity is evidenced by the relatively high electrical resistivity, since charge carriers tend to be significantly scattered by the introduced vacancies and thick grain boundaries due to porosity, resulting in very low carrier conductivity. As presented in Figure 4-3(a), the electrical resistivity of the sample condensed at 900°C was almost doubled, while that of the sample SPS at 1000°C was found to have increased only by 50%, compared with the fully condensed sample SPS at 1100°C. The corresponding Seebeck coefficients, shown in Figure 4-3(b), also showed a systematic increasing trend as condensation temperature increased from 900°C to 1100°C, indicating a decreased porosity. As discussed in Chapter 3, low energy charge carriers are detrimental to thermopower, thus if these carriers were strongly scattered by the vacancies and grain boundaries in a porous sample, the overall thermopower was then enhanced. However, the benefit gained from the enhanced thermopower S was not enough to compensate for the loss in electrical conductivity; in the end, power factor $S^2\sigma/T$ was reduced due to porosity, as seen in Figure 4-3(c).

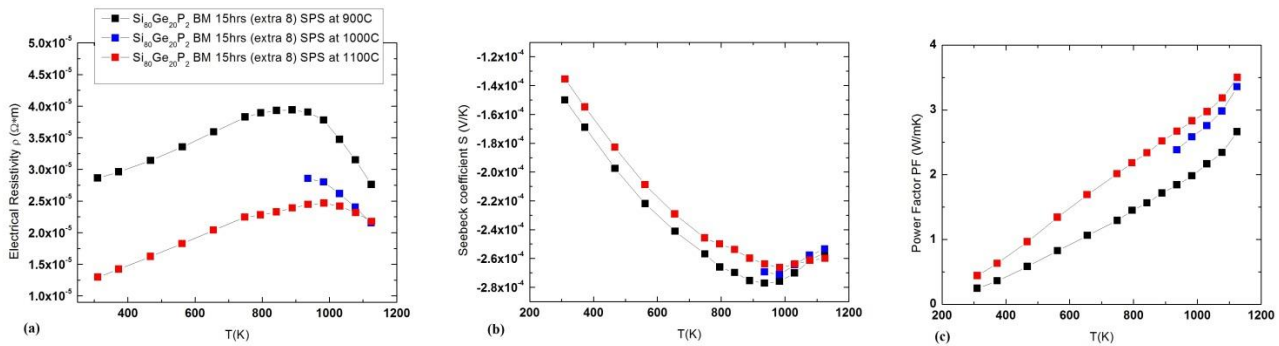


Figure 4-3 Electrical resistivity (a), Seebeck coefficient (b) and Power Factor (c) of $\text{Si}_{80}\text{Ge}_{20}\text{P}_2$ sintered at 900 °C (black), 1000 °C (blue) and 1100 °C (red) separately.

4-4 Grain growth in SPS consolidation process

In this section, the grain growth during SPS is investigated. Nanopowders obtained from 5 hours BM and 15 hours BM were consolidated with SPS, at the same heating rate of $200^\circ\text{C}/\text{min}$, sintering temperature of 1100 °C, pressure of 60MPa and holding time of 6 min. For convenience, the two samples were named SGP-T1-05 and SGP-T1-15 respectively. The mass densities, measured using the Archimedes method, were found to be 3.00 g/cc and 2.99 g/cc, respectively; both values were close to the theoretical value of 2.98 g/cc, indicating full condensations. No impurity phases were found in either sample, according to the XRD scanning, as shown in Figure 4-4, and the diffraction peaks were somewhat shifted due to Si-Ge alloying, compared with these of a Si single crystal.

The average size D of crystalline grains in consolidated samples can be estimated with Scherrer's method as:[90]

$$D = \frac{K\lambda}{w\cos\theta} \quad (4-1)$$

Where K is the Scherrer constant, a shape factor which approximates 0.89 (ratio of full width at half maximum (FWHM) and the integrated breadth), λ is the incident wavelength of X-Ray ($\sim 0.154\text{nm}$ for Cu- $K\alpha$ source), w is the FWHM of a peak at 2θ , and θ is the incident angle with diffraction plane. The average grain sizes of SGP-T1-05 and SGP-T1-15 were calculated to be 54.0 nm and 50.6 nm, respectively. The small difference in grain size between disk sample ball milled for 5 hours and the one for 15 hours was also reflected in their close lattice thermal conductivities, as shown in Figure 4-5.

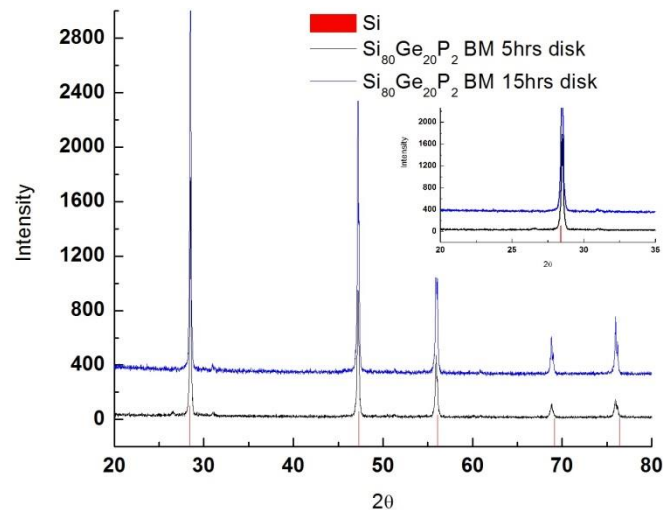


Figure 4-4 XRD pattern of SGP-T1-05 and SGP-T1-15, the inset shows corresponding peaks at (111).

Significant grain growth was disclosed by comparing the grain size in consolidated samples with that in corresponding nanopowders. According to Sherrer's equation, wider diffraction peaks correspond to smaller crystalline grains, and vice versa; as the grain size increases, diffraction peaks become sharper. XRD patterns of $\text{Si}_{80}\text{Ge}_{20}\text{P}_2$ nanopowders (15 hours BM) and the consolidated counterpart are presented in Figure 4-6. A significant grain growth during the consolidation process is indicated by the remarkable reduction in corresponding peak's width in condensed sample.

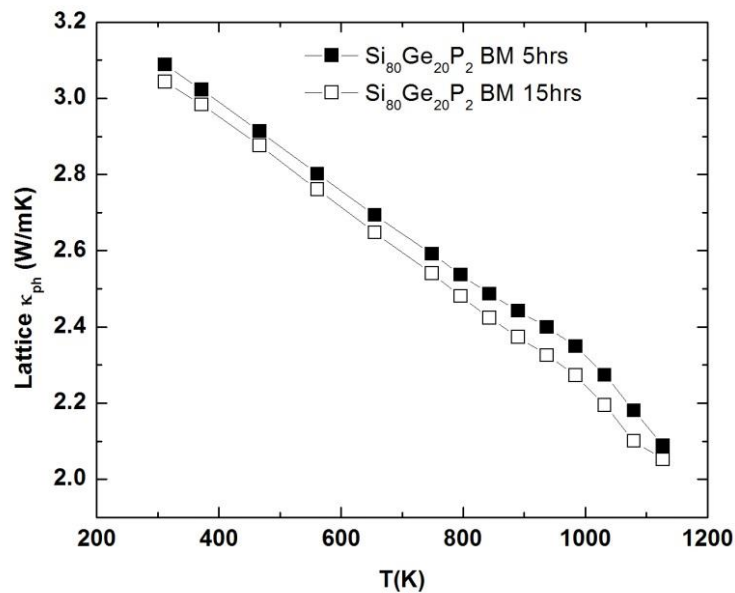


Figure 4-5 Lattice thermal conductivity of SGP-T1-05 and SGP-T1-15.

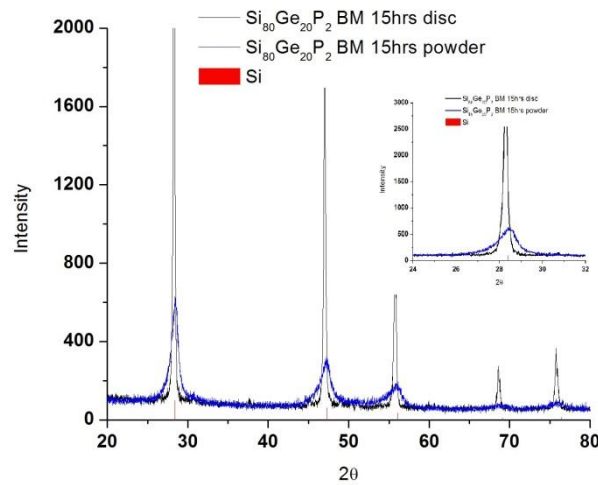


Figure 4-6 XRD pattern of $\text{Si}_{80}\text{Ge}_{20}\text{P}_2$ nanpowders (black) after 15 hours BM and its solidified bulk (blue) form, the inset provides comparison of enlarged diffraction peaks at (111).

A more visualized exhibition of grain growth can be gained under TEM. While the grain size of consolidated bulk $\text{Si}_{80}\text{Ge}_{20}\text{P}_2$ was calculated to be about 50 nm by Scherrer's method, an examination under TEM revealed the inconsistency. Although small grains in the range of 10 nm~20 nm were detected under HRTEM TITAN, as shown in Figure 4-7(c)(d), the size of the majority of the grains, shown in Figure 4-7(a)(b), was found to be extremely large, around 500 nm or even larger, which is far above the estimated 50 nm derived from the peak width of the XRD patterns. The inaccurate estimation of grain size with Scherrer's method can be ascribed to the inaccuracy of FWHM that has been used; in fact, the peak width of a XRD pattern consists of three parts-instrumental broadening, crystallite size broadening and microstrain broadening. When the grains are large (e.g., over 1 μm), the broadening effect coming from crystallite size is so weak that it submerges in the instrumental and microstrain broadening

background; only when the grain size is no more than a few hundred nanometer can the peak width of the XRD patterns be dominated by crystallite size broadening effect, in which case a reasonable approximation of grain size from Scherrer's method can be possibly made. Compared with the grain size of $\text{Si}_{80}\text{Ge}_{20}\text{P}_2$ nanopowders (10~30 nm under TEM as shown in Figure 4-2), remarkable grain growth did take place during SPS process.

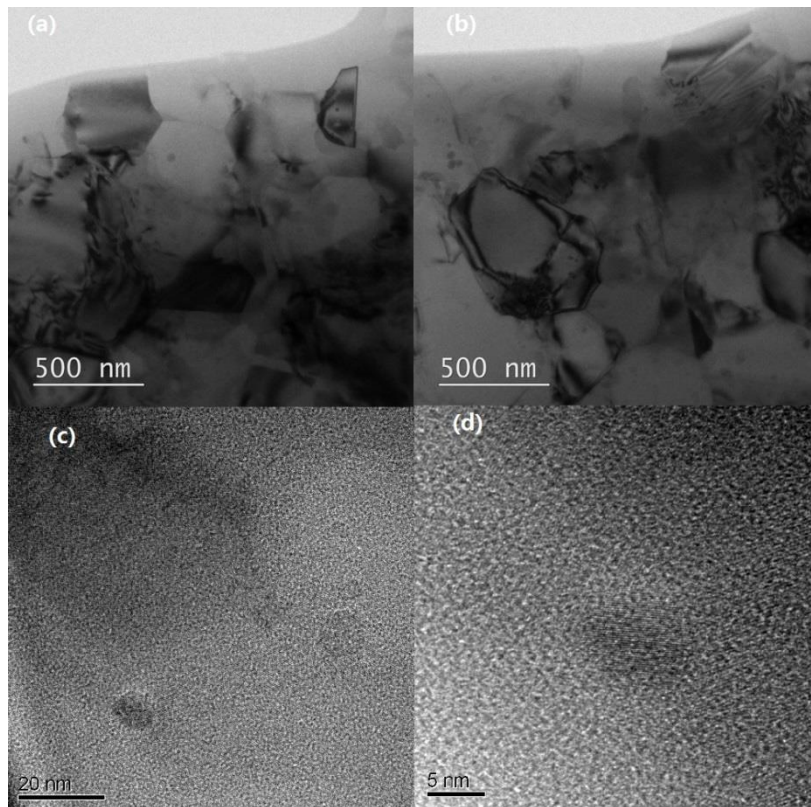


Figure 4-7 Grains of SPS consolidated $\text{Si}_{80}\text{Ge}_{20}\text{P}_2$ with 5 hours BM time under JOEL 2000FX showing the huge majority grains in (a)(b), and HRTEM Titan showing the existence of small minority grains in (c)(d).

Interestingly, no obvious grain growth was reported in similar SiGe composites by Joshi *et al.*[21] during their Hot Press (HP) process, they reported significantly lower thermal conductivity in consolidated nanocomposite with grain size $\sim 20\text{nm}$, compared with the bulk form. Presented in Figure 4-8 is a direct comparison between our measurements and what was reported by the Boston College group; a figure of merit $ZT \sim 1.2$ was achieved compared with the reported $ZT \sim 1.3$ at 1123K . Unfortunately, no detailed consolidation parameters were provided by the Boston College group; however, one can still infer that it was either the internal pulse current heating mechanism of SPS or the relatively high sintering temperature that leads to the significant grain growth in our case. A possible strategy of suppressing grain growth is to lower the sintering temperature, meanwhile, increase the consolidation pressure. Another strategy is to introduce a heterogeneous nanophase to the host grains; as will be shown later, the existence of the incoherent nanophase successfully prohibits grain growth.

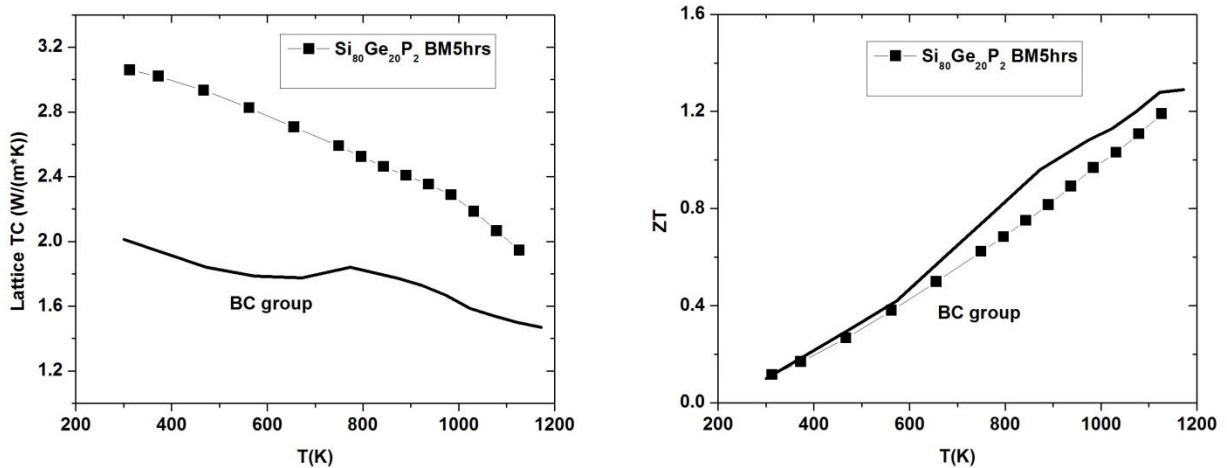


Figure 4-8 Comparison of lattice thermal conductivity and ZT between our samples with significant grain growth (black squares) and Boston College without grain growth (black curve).

For completeness, the condensed $\text{Si}_{80}\text{Ge}_{20}\text{P}_2$ sample made of nanopowders after 15 hours' ball mill was also examined under TEM. The majority grain size was detected to be over $1\mu\text{m}$, as shown in Figure 4-9; smaller grains (10~100 nm and less in quantity) were also found spreading all over the sample, similar as what was observed in the $\text{Si}_{80}\text{Ge}_{20}\text{P}_2$ nanocomposites with only 5 hours' ball mill time.

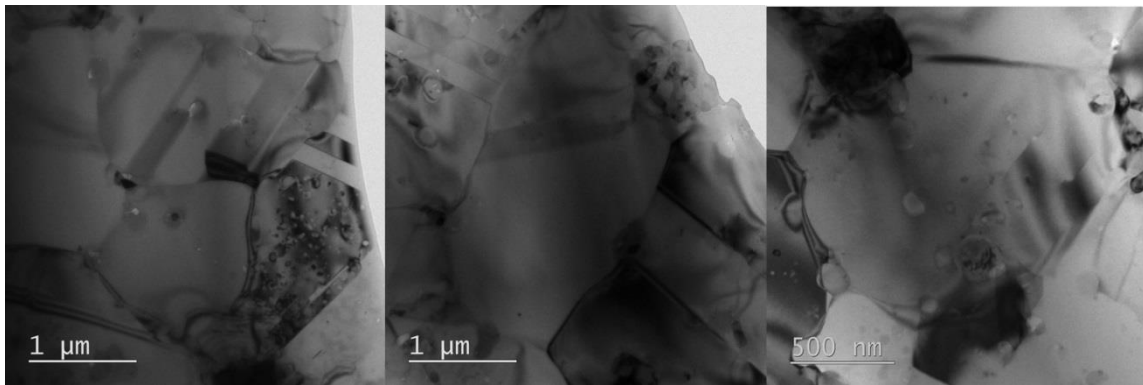


Figure 4-9 $\text{Si}_{80}\text{Ge}_{20}\text{P}_2$ nanocomposites with 15 hours ball mill time examined under JEOL 2000FX (a)(b)(c).

4-5 Heterogeneous nanophases

A heterogeneous nanophase was introduced into the SiGe matrix to act both as extra phonon scattering centers and as low energy charge carrier filters, leading to the reduction in lattice thermal conductivity and the enhancement in the Seebeck coefficient. More remarkably, the introduced heterogeneous nanophase was also able to effectively suppress the grain growth of host grains.

Yttria stabilized Zirconia (YSZ) nanoparticles were dispersed into the $\text{Si}_{80}\text{Ge}_{20}\text{P}_2$ nanopowders which was ball milled for 5 hours. The mixture of powders was ball mixed in a C440 stainless steel vial for 15 minutes, with dodecane as additive to weaken the cold welding effect. The obtained nanopowders were then SPS consolidated at 1100°C , 60MPa, and were sintered for 6 min. $\text{Si}_{80}\text{Ge}_{20}\text{P}_2$ nanopowders without any YSZ were also compressed for comparison. The mass densities of obtained disk-shaped samples were measured using the Archimedes method, and found to be fully condensed. The grain size of $\text{Si}_{80}\text{Ge}_{20}\text{P}_2$ nanopowders before condensation was around 10~30nm, as shown in section 4-2, and the grain size of YSZ nanoparticles was found to range from 15~50 nm, as can be seen in Figure 4-10. However, it was quite difficult to determine if each large grain of YSZ was actually composed of smaller nanocrystals, due to the resolution limit of the TEM (JOEL 2000).

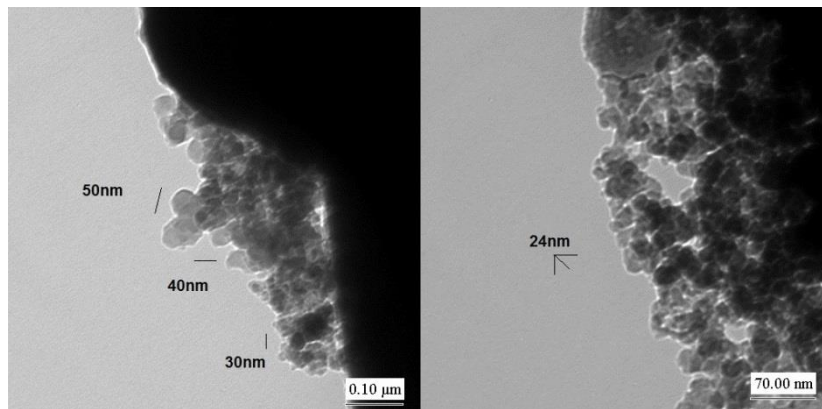


Figure 4-10 TEM image of Yttria Stabilized Zirconia (YSZ) nanopowders.

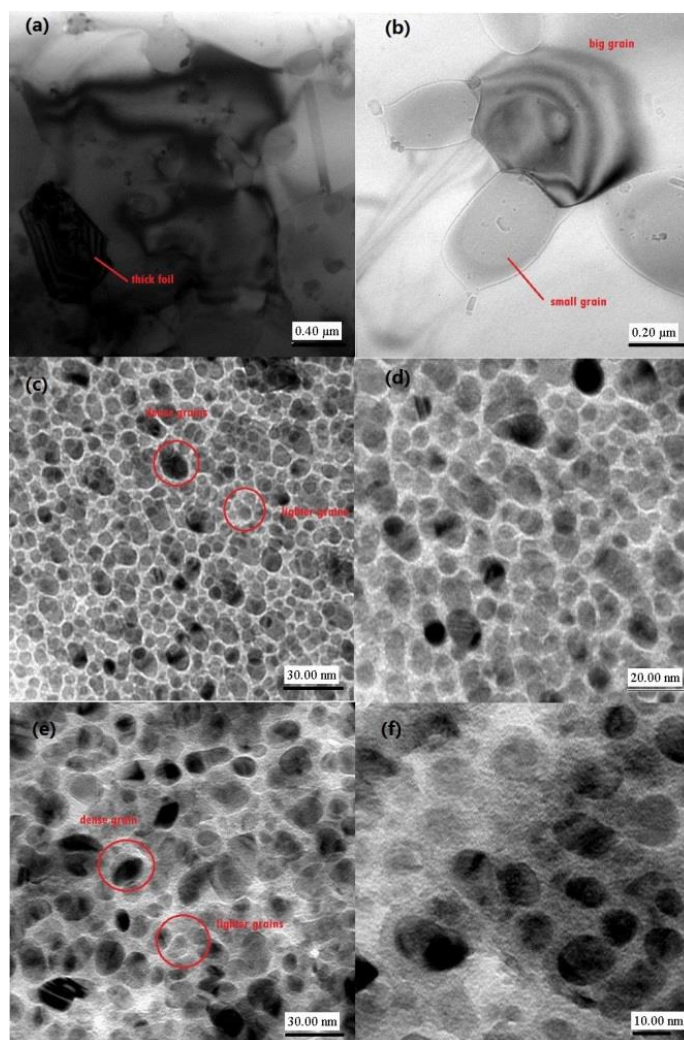


Figure 4-11 TEM images of SPS condensed $\text{Si}_{80}\text{Ge}_{20}\text{P}_2$ nanocomposites (BM for 5hours) with 0% YSZ (a)(b), 5% YSZ (c)(d) and 10% YSZ (e)(f) nanoparticles.

SPS consolidated samples were examined under TEM. As seen in Figure 4-11(a)(b), significant grain growth (from 10~30 nm before SPS to ~500 nm after SPS) was observed in the absence of

heterogeneous YSZ nanoparticles. However, once 5 vol.% YSZ nanoparticles were dispersed into $\text{Si}_{80}\text{Ge}_{20}\text{P}_2$ matrix, the grain size in condensed samples was found to be in the same range as that of corresponding nanopowders, as shown in Figure 4-11(c)(d), indicating nearly no grain growth at all. Similar phenomenon was also observed in the 10 vol.% YSZ dispersed $\text{Si}_{80}\text{Ge}_{20}\text{P}_2$ sample. While YSZ nanoparticles helped to effectively impede grain growth, their extremely wide band gap reduced the overall electrical conductivity; in order to weaken this negative effect, minimal volume fraction of YSZ nanoparticles should be used, as long as grain growth can be effectively impeded.

In a SiGe matrix with YSZ nanoparticles dispersion, as shown in figure 4-11(c)(d)(e)(f), both dense larger and light smaller grains were observed. To distinguish them, Energy Dispersive X-ray spectroscopy (EDS) scanning was applied. Zirconium has two characteristic energy peaks located at 2.2KeV (L_1M_2) and 15.8KeV (KL_3), while phosphorus has a single characteristic energy KM_1 peak located at 2.1KeV. As shown in Figure 4-12, the EDS scanning over the light grains circled in red in Figure 4-11(c) had two energy peaks at around 2KeV and 16KeV, matching with Zr characteristic peaks; while scanning over the dense grains only had a characteristic peak at about 2KeV. The results indicated that light grains were mostly Zr rich YSZ nanograins.

The reason for grain growth being effectively suppressed by heterogeneous nanophase may be stated as: the incoherent grain boundaries between YSZ and $\text{Si}_{80}\text{Ge}_{20}\text{P}_2$ nanoparticles must be too difficult to be overcome, even during the SPS consolidation process with high temperature and high pressure. Grain growth can also be suppressed by the novel core-shell structures which will be discussed in next section.

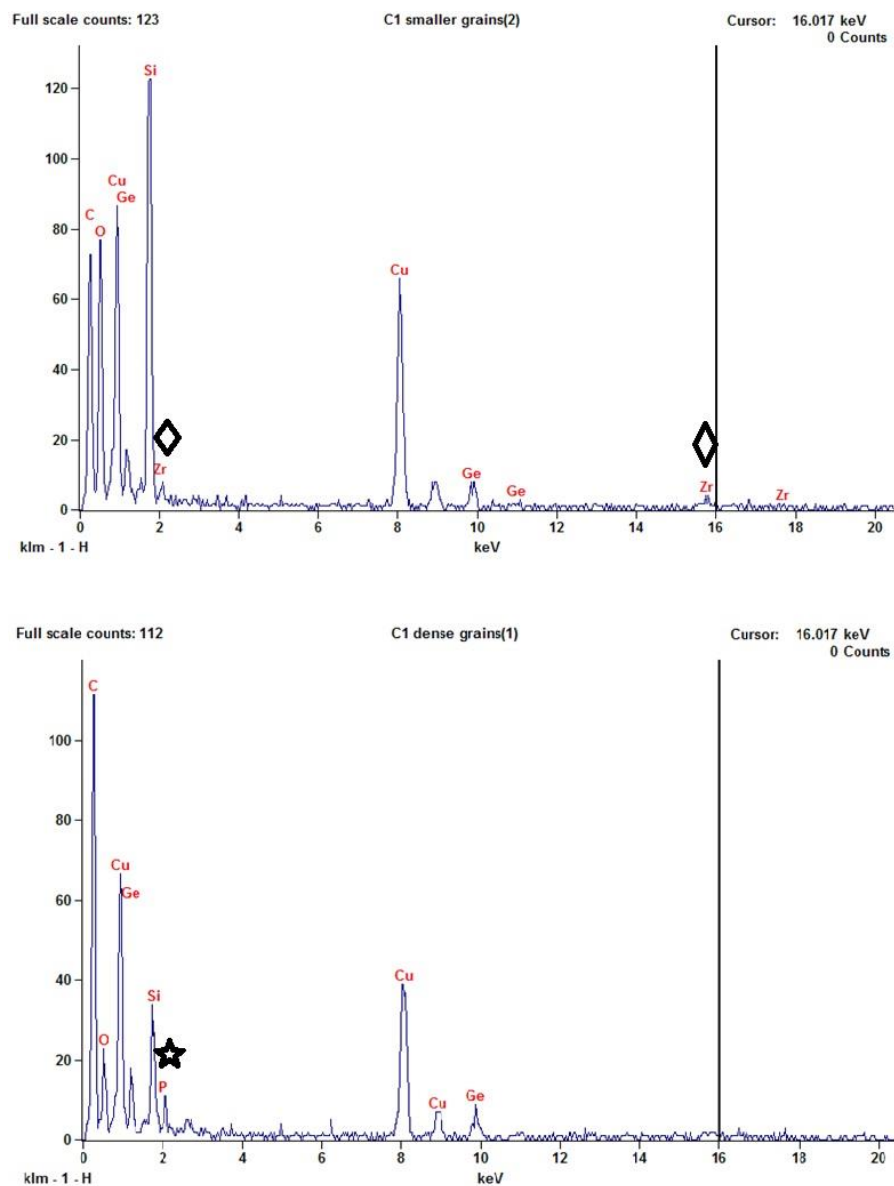


Figure 4-12 EDS scanning over light smaller and dense light grains for 5% YSZ dispersed $\text{Si}_{80}\text{Ge}_{20}\text{P}_2$, indicating the fact that light grains are YSZ, dense grains $\text{Si}_{80}\text{Ge}_{20}\text{P}_2$.

Unfortunately, the incorporation of 10% or even 5% YSZ nanoparticles in the SiGe matrix led to a dramatic increase in electrical resistivity, therefore an degradation in power factor, the overall ZT was found decreased over 15%.

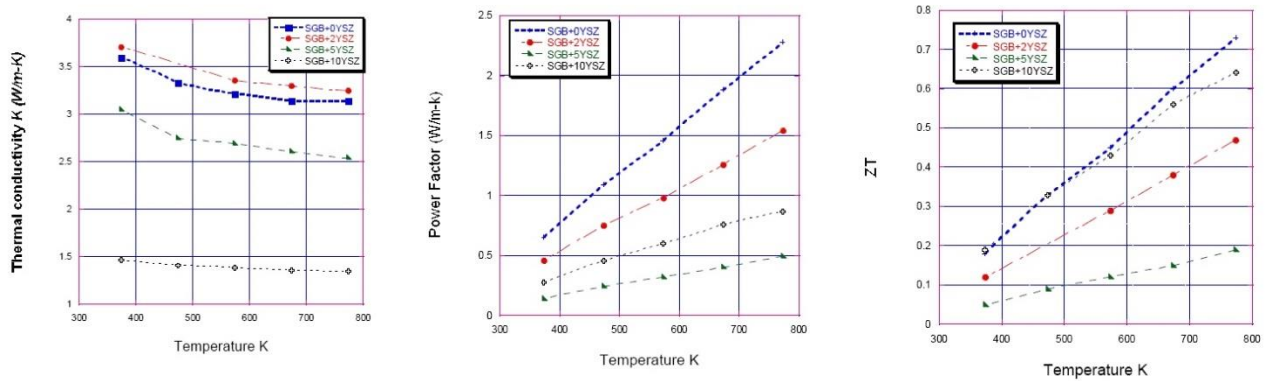


Figure 4-13 Thermal conductivity, power factor and figure of merit ZT of 0%, 2%, 5% and 10% YSZ nanoparticles dispersed Si₈₀Ge₂₀P₂.

4-6 Core-Shell nanostructure

Core-shell nanocrystals are a class of materials whose properties are intermediate between those of small, individual molecules and those of bulk, crystalline semiconductors. They are unique because of their easily modular properties, which are a result of their size. These nanocrystals are composed of a quantum dot core and a shell of a distinct material. Core-shell structure was originally used in

fluoroscopy, organically passivated quantum dots have low fluorescence quantum yield due to surface-related trap states. Core-shell nanocrystals address this problem because the shell increases quantum yield by passivating the surface trap states.[91] In addition, the shell provides protection against environmental changes and photo-oxidative degradation. Precise control of the size, shape, and composition of the core and shell enable the emission wavelength to be tuned over a wider range of wavelengths than either individual semiconductor. Applications for these materials have been found in both biological systems and optics.[92], [93]

The novel core-shell structures have also been applied to enhance thermoelectric materials both theoretically[94] and experimentally.[95] The benefit of nano-sized core-shell structures for TE materials can be summarized as follows:

(1) In this size regime (~20nm), quantum confinement effects lead to a size-dependent band gap with observable, quantized energy levels.[91] The quantized energy levels observed in quantum dots lead to electronic structures that are intermediate between single molecules, which have a single HOMO-LUMO gap, and bulk semiconductors, which have continuous energy levels within bands,[96] as shown in Figure 4-14. The enlarged band gap due to quantum confinement is crucial for a thermoelectric material in that a wider band gap tends to delay the thermal activation of minority carriers, and thus is able to achieve a higher thermopower at high temperatures.

(2) The incoherent boundaries between quantum dot cores and shell layers make grain growth extremely difficult. Core nanoparticles are localized and separated from each other by shell layers, while

layer material has to expel the core particles in order to grow thicker; both of these difficulties are almost impossible to be overcome during the consolidation processes.

(3) The shell layers can also act as energy barriers which can filter lower energy charge carriers that make negative contributions to the Seebeck coefficient.

The properties of semiconducting core-shell structures are based on the relative conduction and valence band edges alignment of the core and the shell; correspondingly, core-shell structures can be classified into three types, as shown in Figure 4-15:[91]

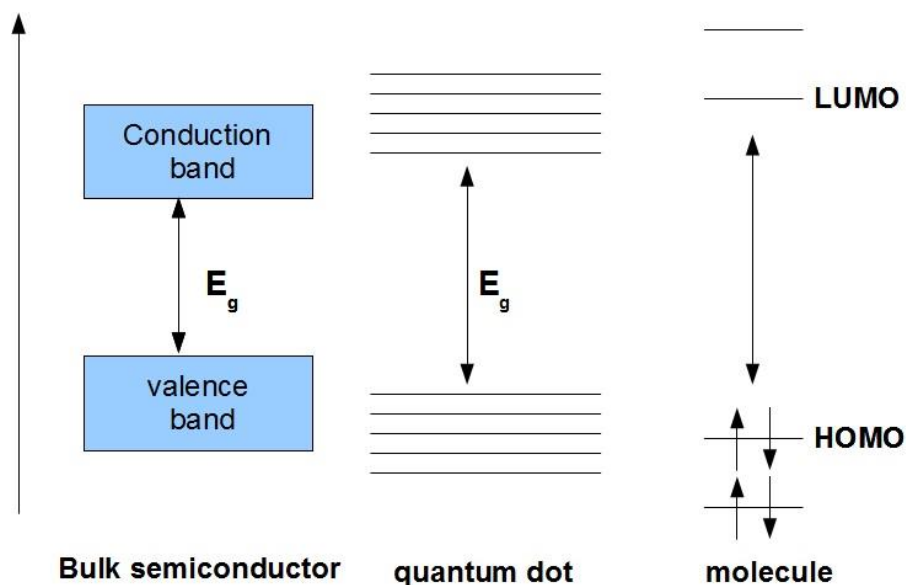


Figure 4-14 A enlarged band gap E_g of a quantum dot due to size effect, compared with its bulk counterpart and single molecule with LUMO-HOMO gap.

Type I: the band gap of the core is smaller than that of the shell. Both the conduction and valence band edges of the core lie within the band gap of the shell, this alignment confines both electrons and holes in the core, as can be seen in Figure 4-16(a). In this core-shell structure, the thermopower and electrical conductivity are dominated by the carriers' density of states (DOS) in CdSe core, while CdS shells act as energy filters.

Reverse Type I: the band gap of the shell is smaller than of the core, with both conduction and valence band edges of the shell lying within the band gap of the core; this alignment confines both electrons and holes in the shell. Therefore, the thermopower and electrical conductivity are determined by the carrier's DOS in the shell, while quantum dots of core serve as energy filters and phonon scattering centers.

Type II: the valence and conduction band edges of the core are either both lower or both higher than the band edges of the shell. An example of type II is shown in Figure 4-16(b), ZnTe (band gap~2.26eV)/CdSe (band gap~1.74eV). The effective band gap is thus reduced and counted from the conduction band edge of CdSe shell to the valence band edge of the ZnTe core.

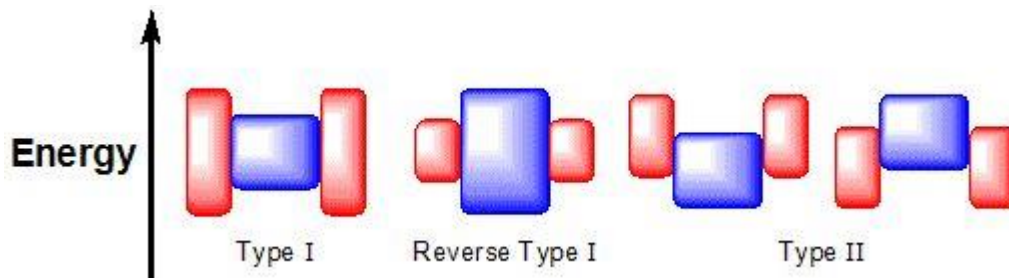


Figure 4-15 Core-shell structures of 3 different types classified by the relative position of conduction and valence band of the core and the shell, with blue and red blocks represent core and shell band structures individually.

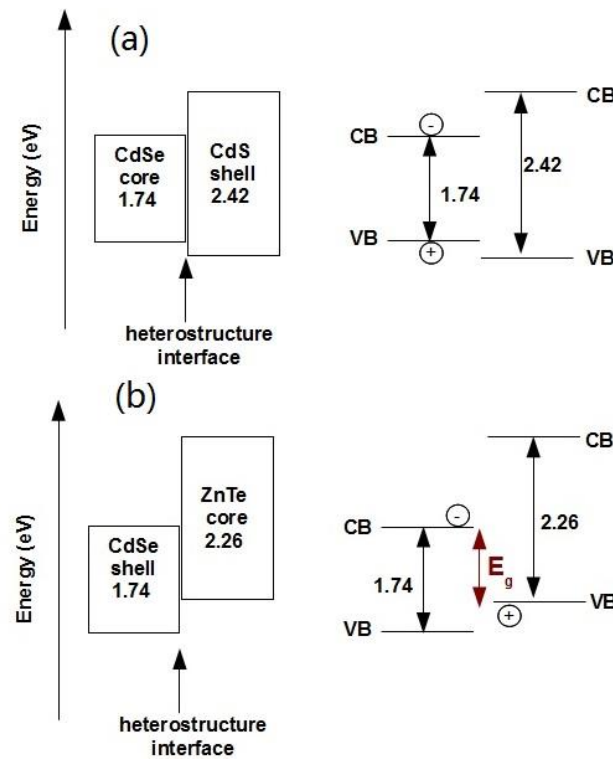


Figure 4-16 (a) Type I CdSe/CdS core/shell structure and (b) Type II CdSe/CdTe core-shell structure.

It is worth noting that the type II core-shell structure is not effective in improving TE properties, since the effective band gap of type II is smaller than the band gap of both the core and the shell. As well known, a narrow band gap is not favorable to achieve high thermopower because it makes the

thermal activation of minority charge carrier easier; it is known that minority charge carriers causes degradation of thermopower via bipolar diffusion.

Several wet chemical methods, such as chemical precipitation, sol-gel, microemulsion and inverse micelle formation, have been developed to synthesize core shell nanoparticles, with an emphasis on better control of size, shape, and size distribution. In our case, the sol-gel method was utilized to coat P-type $\text{Si}_{80}\text{Ge}_{20}\text{B}_{1.7}$ nanoparticles with Yttria stabilized Zirconia (YSZ), SiO_2 and TiO_2 . TEM image of consolidated YSZ coated $\text{Si}_{80}\text{Ge}_{20}\text{B}_{1.7}$ nanoparticles is shown in Figure 4-17, it was found that nanoscaled (10~30nm) $\text{Si}_{80}\text{Ge}_{20}\text{B}_{1.7}$ cores were separated from each other by the continuous medium consisting of smaller YSZ nano-grains. Although this configuration was not a core-shell structure in the strict sense, it succeeded in suppressing grain growth and filtering low energy carriers, as a real core-shell should.

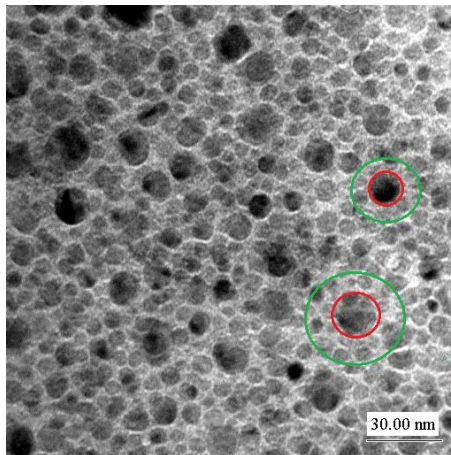


Figure 4-17 The pseudo core (red circle)/shell (green circle) structure of $\text{Si}_{80}\text{Ge}_{20}\text{B}_{1.7}/\text{YSZ}$ nanocomposite.

Provided that the $\text{Si}_{80}\text{Ge}_{20}\text{B}_{1.7}/\text{SiO}_2$ and $\text{Si}_{80}\text{Ge}_{20}\text{B}_{1.7}/\text{TiO}_2$ core-shell structures are presumed to have the same pseudo core-shell microstructures as $\text{Si}_{80}\text{Ge}_{20}\text{B}_{1.7}/\text{YSZ}$, their TE properties were discussed. As presented in Figure 4-18, the electrical resistivity ρ was significantly increased by introducing core-shell structures; the thermopower S was enhanced in the $\text{Si}_{80}\text{Ge}_{20}\text{B}_{1.7}/\text{SiO}_2$ core-shell but somewhat reduced in the $\text{Si}_{80}\text{Ge}_{20}\text{B}_{1.7}/\text{TiO}_2$ core-shell; and lattice thermal conductivity was reduced in the temperature range from 300K to 1100K in both core-shell structures. The behavior difference in thermopower S and electrical resistivity between SiO_2 and TiO_2 coated $\text{Si}_{80}\text{Ge}_{20}\text{B}_{1.7}$ can be attributed to their band gap alignment of shell and core.

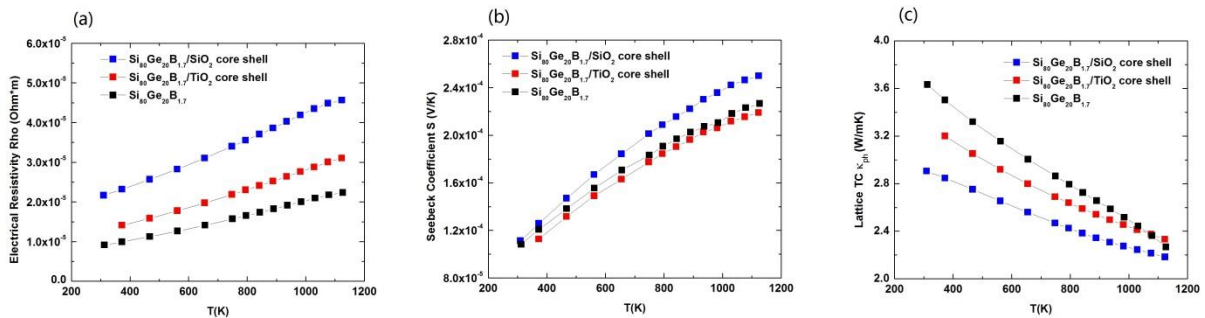


Figure 4-18 Comparison of thermoelectric properties of $\text{Si}_{80}\text{Ge}_{20}\text{B}_{1.7}/\text{SiO}_2$ (blue square) and $\text{Si}_{80}\text{Ge}_{20}\text{B}_{1.7}/\text{TiO}_2$ (red square) core-shell structures with $\text{Si}_{80}\text{Ge}_{20}\text{B}_{1.7}$ nanocomposite (black square).

The relative alignment of conduction and valence band edges of the core ($\text{Si}_{80}\text{Ge}_{20}\text{B}_{1.7}$) and the shell (SiO_2 and TiO_2) is presented in Figure 4-19. $\text{Si}_{80}\text{Ge}_{20}\text{B}_{1.7}/\text{SiO}_2$ belongs to type I core-shell structure as discussed above, with both valence and conduction band edges of SiGe core lying in the band gap of the SiO_2 shell; in contrast, $\text{Si}_{80}\text{Ge}_{20}\text{B}_{1.7}/\text{TiO}_2$ belongs to type II core-shell structure. The height of the energy

barriers are determined by the valence band edge difference between the core and the shell. It can be clearly seen that it is more difficult for holes in the $\text{Si}_{80}\text{Ge}_{20}\text{B}_{1.7}$ core to transport through the SiO_2 shell than through the TiO_2 shell, thus a more significant drop in the hole concentration and eventually a much higher electrical resistivity are expected in $\text{Si}_{80}\text{Ge}_{20}\text{B}_{1.7}/\text{SiO}_2$ than in $\text{Si}_{80}\text{Ge}_{20}\text{B}_{1.7}/\text{TiO}_2$. The effective band gap E_g of the type I $\text{Si}_{80}\text{Ge}_{20}\text{B}_{1.7}/\text{SiO}_2$ core-shell stays the same as core SiGe $\sim 0.8\text{eV}$, while for $\text{Si}_{80}\text{Ge}_{20}\text{B}_{1.7}/\text{TiO}_2$ of type II, the effective band gap is the separation between the valence band edge of the SiGe core and the conduction band edge of the TiO_2 shell, which is $< 0.8\text{eV}$, as shown in Figure 4-17. Although, low energy holes in SiGe core are filtered by the TiO_2 energy barriers, ideally leading to an enhanced thermopower, the reduced effective band gap make thermal activation of minority carriers much easier; these two effects together explains the thermopower reduction in $\text{Si}_{80}\text{Ge}_{20}\text{B}_{1.7}/\text{TiO}_2$. Introduced core-shell structures also increase the intensity of phonon scattering, regardless of their type, resulting in the reduction of lattice thermal conductivity, as presented in Figure 4-18(c).

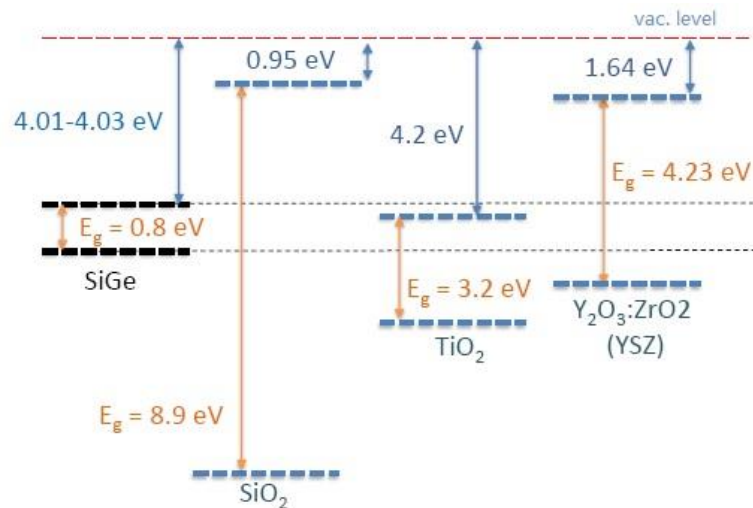


Figure 4-19 Conduction and valence bands alignment of SiGe core and SiO₂/TiO₂/YSZ shell.

Although grain growth was suppressed in the core-shell structures discussed above, however, the electrical resistivity was significantly increased since a decent number of charge carriers were filtered by the thick YSZ shells, the increase in electrical resistivity is so significant that the benefits gained in thermopower, thermal conductivity couldn't even compensate, eventually leading to a degradation in overall ZT as shown in Figure 4-20. The fabrication technique has to be improved to construct much thinner shells around core materials.

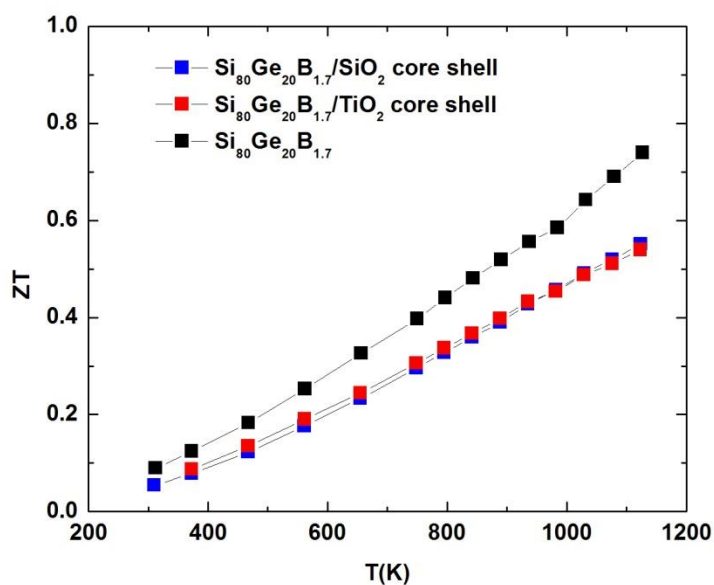


Figure 4-20 Figure of merit ZT in Si₈₀Ge₂₀B_{1.7}/SiO₂ and Si₈₀Ge₂₀B_{1.7}/TiO₂.

The discussions above suggest that core-shell structures which can be used to improve the TE properties should be limited to type I, and that the difference of conduction/valence band edges between the core and the shell needs to be restricted to a mild level; only in this circumstance, can enhancement in the thermopower, and reduction in the thermal conductivity be achieved simultaneously, eventually results in the enhancement in figure of merit ZT.

4-7 Conclusions and future work

N-type $\text{Si}_{80}\text{Ge}_{20}\text{P}_2$ and P-type $\text{Si}_{80}\text{Ge}_{20}\text{B}_{1.7}$ nanocomposites were synthesized using high energy vibrational ball mill method, followed by SPS consolidations. The dependence of the grain size of obtained nanopowders on ball mill time was investigated, and it was found that five hours was sufficient to obtain nanograins of 10~30nm; extended ball mill time did not show evidence of further reducing the grain size. During the SPS consolidation process, porosity due to insufficient sintering temperature was found to be fatal to TE performance; although thermopower S and thermal conductivity κ may be enhanced via energy filtering effect and enhanced phonon scattering respectively, the benefit gained in S and κ was not able to compensate for the significant loss in the electrical conductivity. It was also found that severe grain growth took place during the SPS consolidation process; the characteristic grain size in condensed SiGe bulk samples was as large as 500nm~1 μm , while it had been only 10~30nm in SiGe nanopowders before SPS consolidation. Despite the grain growth, we managed to obtain the figure of merit $ZT\sim 1.2$ in N-type $\text{Si}_{80}\text{Ge}_{20}\text{P}_2$ and $ZT\sim 0.75$ in P-type $\text{Si}_{80}\text{Ge}_{20}\text{B}_{1.7}$ both at 1123K. The significant

grain growth could be attributed to the relatively small mismatching potentials or coherent interfaces between SiGe nanograins; thus, we suggested suppressing grain growth by introducing incoherent grain boundaries. Heterogeneous nanophase as well as core-shell structures were performed at this point and both were proved to be capable of effectively suppress the grain growth in the SPS consolidation processes; moreover, enhanced phonon scattering intensity as well as energy filtering effects were also observed.

Significant degradations in electrical conductivity were observed upon using nano-sized oxides either as external phases or pseudo shell materials, due to the oxides' extremely wide band gaps. In the future, investigations should be performed in finding proper materials which have proper band structure alignments with $\text{Si}_{80}\text{Ge}_{20}$ host in order to introduce incoherent or semi-coherent interfaces to impede grain growth without affecting the charge carrier transport. Exploration in fabrication techniques to construct core-shell structures with much thinner shells should also be conducted.

5. Effective Medium Theory

To simulate the lattice thermal conductivity reduction effect due to nanoinclusions, deterministic solutions of phonon Boltzmann transport equation (BTE), [97], [98], [99], [100] Callaway model [57], [101] derived from BTE and Monte Carlo simulations with either frequency independent gray model [102] or the non-gray model [77] [103] have been developed. There are also first-principles calculations, using a Kubo-Greenwood style approach, accounting for disorder-induced scattering that many other models which are based on the Peierls-Boltzmann equation, coherent potential approximation, or atomic models failed to take into account. [21] [97] Nevertheless, even the most simplified ab-initio/first principles calculation requires extensive modeling and computing time, restricting its extensive applications. A phenomenological effective medium approach (EMA) by Nan *et al.* [104] [105] provided an alternative way to study two-phase heterogeneous systems. Incorporated within the average T-matrix approximation (ATA), Minnich and Chen [106] proposed the modified effective mean free path (MFP) for both matrix and second-phase materials. The modification came from phonons' independent particle scattering off embedded nanoparticles, in addition to thermal boundary resistance. However, this ATA was based on first-order T-matrix approximation, thus only applicable in small volume fractions. Poon *et al.* extended this effective medium approach to the whole volume fraction range from 0 to 1 by introducing a differential effective medium (DEM) method [107], [108] with multiple scattering that dominates at high volume fractions being inherently implemented.

Prior experiments[53], [85], [109] have indicated a dramatic reduction in lattice thermal conductivity κ_{ph} even with only a small volume fraction of nanoinclusions, which is unable to be well explained by various effective medium theories (EMT) mentioned above. The disagreement between models and experimental data strongly indicates that the grain boundary scattering effect was underestimated, especially at low volume fractions. One possible reason for this underestimation of interface scattering is that the scattering cross section of an embedded nanoparticle was believed to be the spherical particle's projected area $\pi(d/2)^2$ in previous works.[106], [107], [108] Inspired by Kim *et al.*,[110] we implemented the much more rigorously calculated effective scattering cross section σ_{eff} , as well as grain size dispersion, into DEM simulation to achieve a better agreement with both the MC simulation by Jeng[102] and the experimental results.[111]

5-1 Average T-Matrix Approximation (ATA) and Coherent Potential Approximation (CPA)

5-1-1 ATA

The effective medium theory is adopted to deal with the effective thermal conductivity in a heterogeneous system. Following Nan's work, the effective thermal conductivity k^* of a heterogeneous system can be deduced from the following set of equations:

$$k^* = k_0 + \langle T \rangle / (1 + \langle GT \rangle) \quad (5-1a)$$

$$T = \sum_n T_n + \sum_{m \neq n} T_n G T_m + \sum_{m \neq n \neq l} T_m G T_n G T_l + \dots \quad (5-1b)$$

$$T_n = \delta k_n \delta_n(\mathbf{r}) / (I - \delta k_n \delta_n(\mathbf{r}) G) \quad (5-1c)$$

$$\frac{k^* - k_0}{k^* + (D-1)k_0} = \sum_i f_i \frac{k_i - k_0}{k_i + (D-1)k_0} \quad (5-1d)$$

$$\sum_i f_i \frac{k_i - k_0}{k_i + (D-1)k_0} = 0 \quad (5-1e)$$

Where k_0 , a non-perturbation term, is the spatial invariant part of the thermal conductivity, and usually chosen as host's thermal conductivity k_h . The embedded nano-grain is labeled by index n . T is the transfer matrix, and has the same spatial dimension as the system. G is the Green's function matrix, and I is the unit matrix. δk_n is given by $\delta k_n = k_n(\mathbf{r}) - k_0$, representing the perturbation coming from the embedding of grain n . $\delta_n(\mathbf{r})$ is a set-on number, equal to 1 if \mathbf{r} (vector) is inside the grain n , otherwise zero. To make Eqn (5-1a) soluble, usually only the first order term in Eqn (5-1b) is retained; that is, $T \approx \sum_n T_n$. This estimation is named the independent particle approximation, with multiple-particle interaction terms being ignored. It is worth nothing that only when the concentration of the second phase is dilute can multiple scattering be ignored. Combining (5-1a, 5-1b and 5-1c), Eqn (5-1d) can then be obtained (D is system's dimension). For a two-phase system that the volume fraction of the second phase is small, replacing k_0 by k_h , f_i by corresponding volume fraction f of the second phase, and k_i by k_p^* , k^* then can be expressed as:

$$k^* = k_h \frac{(1+2f)k_p^* + 2(1-f)k_h}{(1-f)k_p^* + (2+f)k_h} \quad (5-2)$$

Considering the thermal barrier resistance at phase boundaries, k_p^* can be expressed as:

$$k_p^* = \frac{k_p}{1 + \frac{Rk_p}{d/2}} = \frac{k_p}{1 + \frac{\alpha k_p}{k_h}} \quad (5-3)$$

Where k_p is the thermal conductivity of the second phase, d is the grain size of embedded particle, R is the thermal barrier resistance, and α is the dimensionless thermal resistance parameter defined as $\alpha = Rk_h/(d/2)$. Substituting k_p^* of Eqn (5-3) into Eqn (5-2) gives the form of $k^*(\phi)_{ATA}$ in the following expression, with volume fraction f replaced by ϕ :

$$k^*(\phi)_{ATA} = k_h \frac{k_p(1+2\alpha(\phi)) + 2k_h + 2\phi(k_p(1-\alpha(\phi)) - k_h)}{k_p(1+2\alpha(\phi)) + 2k_h - \phi(k_p(1-\alpha(\phi)) - k_h)} \quad (5-4)$$

5-1-2 CPA

If letting $\langle T \rangle = 0$ in Eqn (5-1a), with the assumption that perturbation due to impurity phase is as small as possible (i.e., ~ 0), each grain of the second phase is equivalently embedded into the same self-consistent effective medium with the effective property k^* . For a two-phase heterogeneous system, within Eqn (5-1b) and Eqn (5-1c), adopting only the first-order approximation of T , Eqn (5-1e) is derived and the coherent potential approximation (CPA) gives:

$$2k_{CPA}^* - ((2-3\phi)k_h + (3\phi-1)k_p^*)k_{CPA}^* - k_h k_p^* = 0 \quad (5-5)$$

Both ATA and CPA account for the first order independent particle scattering and thus can only be applied in the system that the volume fraction of second phase is dilute. The difference between them is that CPA allows particle clusters, while ATA requires an even distribution of second-phase particles in the main matrix.

5-2 Differential Effective Medium (DEM) approach

The application of ATA is restricted to the systems where the second phase has low volume fractions, as seen from the deduction process discussed above. To extend ATA to the heterogeneous systems with higher volume fractions of second phase, the differential method, as discussed by Bruggeman,[112] is then implemented to Eqn (5-4). For convenience, the effective thermal conductivity k^* is replaced by k hereafter. The main idea of this differential approach is that, at volume fraction ϕ , k_h is updated to the instantaneous effective thermal conductivity $k(\phi/(1-d\phi))$, since the volume $d\phi$ to be occupied by the added particles does not contribute to $k_h(\phi)$, as shown in Figure 5-1; upon adding $d\phi$ of particles to the new host, the overall effective thermal conductivity is then $k(\phi+d\phi)$. $k(\phi/(1-d\phi))$ can be expanded into $k(\phi) + k'(\phi)d\phi$, or $k(\phi) + \phi dk(\phi)$ with first-order approximation. The updated host conductivity is expressed as:

$$k_h(\phi) \rightarrow k(\phi) + \phi dk(\phi) \quad (5-6)$$

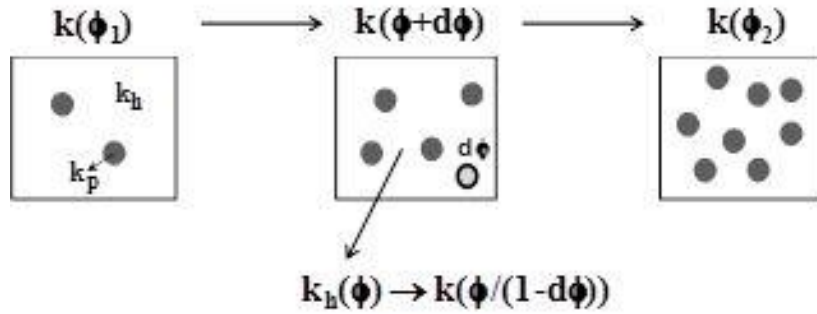


Figure 5-1 Configuration of adding $d\phi$ of second phase in DEM regime.

Upon introducing the second-phase nanoparticles, the effective mean free path (MFP) of host and second phase has to be modified as follows:[106]

$$\begin{cases} \frac{1}{L_{eff,host}} = \frac{1}{L_{bulk,host}} + \frac{1}{L_{sct}} \\ \frac{1}{L_{eff,np}} = \frac{1}{L_{bulk,np}} + \frac{1}{d} \end{cases} \quad (5-7)$$

Where $L_{sct} = V/\sigma_{eff} = \pi d^3/(6\phi\sigma_{eff})$, V is the mean volume containing only one nanoparticle, d is the mean diameter of the spherical nanoparticles, ϕ is the volume fraction of nanoparticles, and σ_{eff} is the effective scattering cross section of the nanoparticle. For hard sphere scattering in the independent-particle approximation, σ_{eff} is assumed to be the spherical particle's projected area $\pi d^2/4$; thus, the host's thermal conductivity is given by the renormalized function $k_h(\phi_f) = k_h/(1+3L_h\phi_f/2d)$, where ϕ_f is the targeted filling fraction. In the differential approach, $k_h(\phi+d\phi) = k_h(\phi)/(1+3L_h(\phi)d\phi/2d) =$

$k_h(\phi)/(1+(3L_h(\phi)\phi_f/2d)(d\phi/\phi_f))$. For other forms of phonon-particle scattering other than independent-particle scattering, the scattering function $3\phi/2$ can be replaced by $F(\phi)$; $k_h(\phi)$ may then be written as $k_h(\phi)=k_h/(1+L_hF(\phi)/d)$ in the first-order approximation and the updated thermal conductivity of the new host:

$$k_h(\phi+d\phi) = k_h(\phi)/(1+L_h(\phi)F(\phi_f)(d\phi/\phi_f)/d) \quad (5-8)$$

Substituting Eqn (5-6) in (5-8), keeping only the first order terms and replacing $L_h(\phi)$ by $L(\phi)$, which is $3k(\phi)/(v_g c_p)$, where v_g is the average group velocity, and $k_h(\phi+d\phi)$ can be written as:

$$k_h(\phi + d\phi) \rightarrow k(\phi) + \phi dk(\phi) - k(\phi) \frac{L(\phi) F(\phi_f)}{d \phi_f} d\phi \quad (5-9)$$

Upon adding $d\phi$ particles to the composite, $k(\phi+d\phi)$ can be written like Eqn (5-4):

$$k(\phi + d\phi) = k_h(\phi + d\phi) \frac{k_p(1+2\alpha(\phi+d\phi))+2k_h(\phi+d\phi)+2d\phi(k_p(1-\alpha(\phi+d\phi))-k_h(\phi+d\phi))}{k_p(1+2\alpha(\phi+d\phi))+2k_h(\phi+d\phi)-d\phi(k_p(1-\alpha(\phi+d\phi))-k_h(\phi+d\phi))}$$

$$(5-10)$$

Substituting Eqn (5-6) and Eqn (5-9) into Eqn (5-10), keeping only the first order term, $k(\phi+d\phi)$ becomes:

$$k(\phi + d\phi) = k(\phi) + \phi dk(\phi) - k(\phi) \frac{L(\phi) F(\phi_f)}{d \phi_f} d\phi + 3k(\phi)d\phi \frac{k_p(1-\alpha(\phi))-k(\phi)}{k_p(1+2\alpha(\phi))+2k(\phi)}$$

(5-11)

Rearranging the terms, the following differential form of $k(\phi)$ is obtained:

$$dk(\phi) = \frac{3k(\phi)d\phi}{1-\phi} \left\{ \frac{k_p(1-\alpha(\phi))-k(\phi)}{k_p(1+2\alpha(\phi))+2k(\phi)} - \frac{L(\phi)F(\phi_f)}{3d\phi_f} \right\} \quad (5-12)$$

The effective thermal conductivity obtained by this method is named $k^*(\phi)_{\text{DEM}}$ in this chapter. The authenticity of this differential expression is straightforward if one considers only independent-particle scattering; if we let $F(\phi)=3\phi/2$, Eqn (3) in reference 107 is obtained. The DEM approach is a decent improvement over ATA, not only because it extends ATA to the full volume fraction range from 0 to 1, but also it is able to inherently implement multiple scattering with well selected $F(\phi)$, as to be discussed later.

5-3 Comparison between DEM and ATA

As discussed above, ATA is derived from small perturbation theory: the embedded particle in consideration is taken as a small perturbation, while matrix material is considered a homogeneous effective medium without considering the effect from other embedded particles; therefore, ATA only hold physical meanings at low volume fractions of the second phase. For DEM, again, the embedded particle in consideration is taken as a perturbation; however, in this case the effective medium is the

combination of host and previously embedded second phase. Thus, the small perturbation holds true for all the volume fractions from 0 to 1 in DEM. At dilute volume fractions, ATA and DEM do not have much difference; when the volume fraction ϕ increases to the extent that the small perturbation in ATA no longer holds, the difference between DEM and ATA will arise.

Without losing generality, independent-particle scattering $F(\phi)=3\phi/2$ is adopted in this section. The average mean free path ℓ (MFP) can be deduced via the customary method of $\ell=3k/c_p v_g$, where v_g is the average group velocity, c_p is the specific heat. At room temperature and above, most phonons are populated close to the Brillouin zone boundary, where acoustic phonons' group velocities are significantly smaller than the speed of sound v_s . [113] In this case, a characteristic group velocity is estimated by averaging $v_g=v_s \cos(qa/2)$, where q is the wavenumber and a is the crystal lattice constant, over the phonon spectrum, [107], [108] yielding approximately $0.38v_s$. Considering the difficulty of obtaining a complete series of parameters for a certain composite, some estimated equations are also utilized to figure out unknown parameters.

Debye Temperature θ_D : [114]

$$\theta_D = \frac{h v_s}{k} \left(\frac{3n}{4\pi V} \right)^{\frac{1}{3}} \quad (5-13)$$

Sound velocity v_s :

$$\begin{cases} 3v_s^{-2} = 2v_{trans}^{-2} + v_{long}^{-2} \\ v_{trans} = \sqrt{G/\rho} \\ v_{long} = \sqrt{E/\rho} \end{cases} \quad (5-14)$$

Where h is the Plank constant, k is the Boltzmann constant, n is the number of atoms in unit cell, V is the volume of unit cell, G and E are shear and Young's modulus, respectively, and ρ is the mass density.

Table 5-1 The parameters used in nanocomposite calculations for DEM and ATA. [86], [115], [116], [117], [118]

composites	Debye θ_D (K)	κ_{bulk} (W/(m*K))	C_p (10^6 J/m ³ K)	V_s (m/s)	V_g (m/s)	MFP(nm)
YSZ/CoSb ₃	527/307	1.8/14.5	3.27/1.79	3737/2998	1420/1139	1.16/21.3
CoSb ₃ /CoSb ₃	307/307	14.5/14.5	1.79/1.79	2998/2998	1139/1139	21.3/21.3

DEM and ATA calculations are performed on two nanocomposites; one is inert Yttria Stabilized Zirconia (YSZ) nanoparticles embedded in skutterudite CoSb₃, and the other is a fictional nanostructure with CoSb₃ nanoparticles being embedded in a CoSb₃ matrix. The grain sizes of nanoparticles in both nanocomposites are varying from 50 nm to 5 nm.

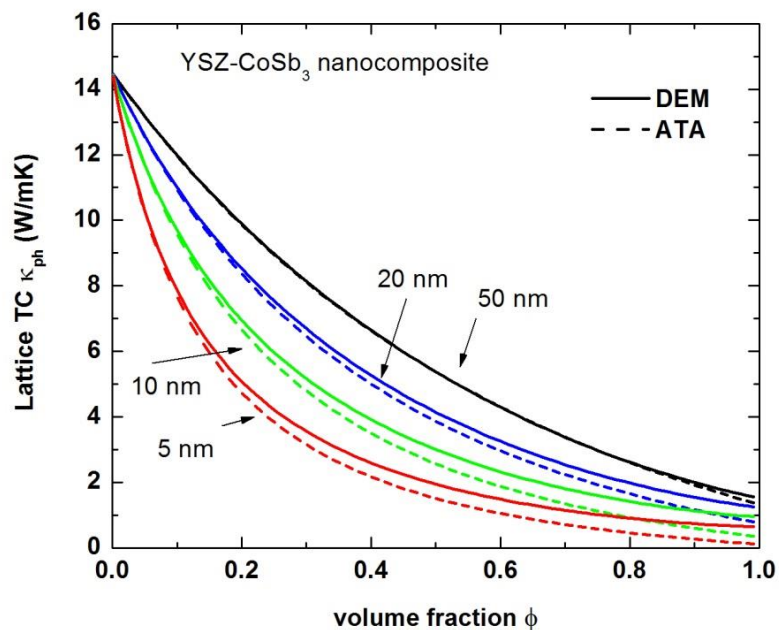


Figure 5-2 Dependence of lattice thermal conductivity κ_{ph} in YSZ/CoSb₃ nanoparticle/matrix system on volume fraction ϕ at 300K, with DEM (solid lines) and ATA (dash lines) calculations; the grain size of YSZ nanoparticles are set to be 50, 20, 20, 5 nm separately.

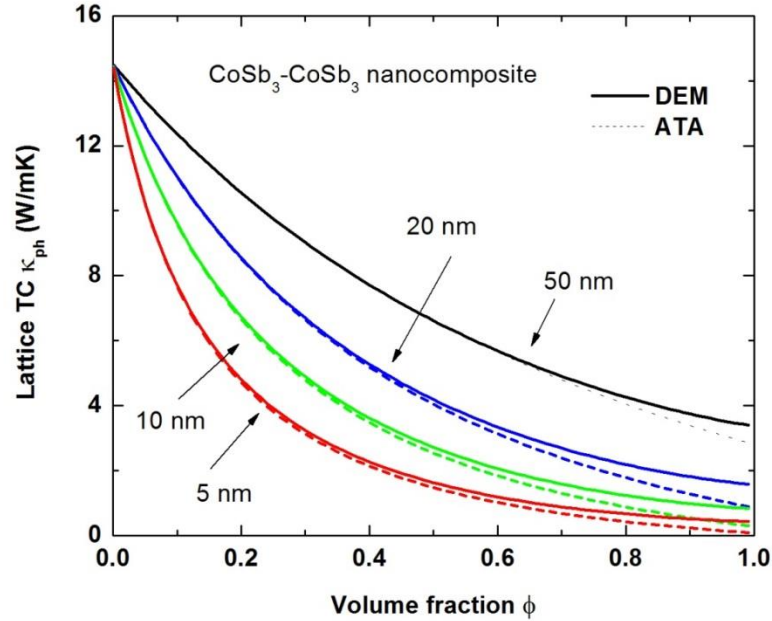


Figure 5-3 Dependence of lattice thermal conductivity κ_{ph} in a CoSb₃/CoSb₃ nanoparticle/matrix system on volume fraction ϕ at 300K, with DEM (solid lines) and ATA (dash lines) calculations; the grain size of YSZ nanoparticles are set to be 50, 20, 20, 5 nm separately.

It can be seen from Figure 5-2 and Figure 5-3 that, for both ATA and DEM, as the volume fraction ϕ of nanoparticles increases, the lattice thermal conductivity decreases significantly. At the same volume fraction, nanoparticles of smaller size have a better effect on obstruct phonon transport, because a smaller particle size corresponds to a higher interface density and lower effective phonon MFP, thus a lower effective lattice thermal conductivity. Indeed, nanostructuring is an impressive way to reduce lattice thermal conductivity; at $d=5\text{nm}$, with only 20% YSZ nanoparticles embedment, κ_{ph} is reduced by 60%. As discussed above, ATA actually holds physical meaning only at low volume fractions; as long

as small perturbation theory is valid, there should be little difference between ATA and DEM. The calculations shown in both figures at various grain sizes confirm this deduction; in both nanocomposites, only when volume fraction ϕ exceeds 10%, will considerable differences arise between ATA and DEM. In the YSZ/CoSb₃ system, at grain size 50 nm, the DEM calculation does not start to diverge from ATA until ϕ is over 80%!

It is interesting to see that, the smaller the grain size d is, the lower is the volume fraction ϕ needed to observe the divergence of DEM and ATA. The divergence arises at a threshold where small perturbation theory cannot apply, as previously discussed. This threshold is evaluated in term of volume fraction, however, considering that the lattice thermal conductivity reduction actually comes from interface scattering, it is more plausible to use interface density instead of volume fraction.[106] At the same volume fraction, smaller grains result in higher interface density, thus more intense phonon interface scattering. A re-plot of lattice thermal conductivity vs. interface density in the YSZ/CoSb₃ nanocomposite system is presented in Figure 5-4, in which the interface density Φ is calculated in the case of spherical particles:

$$\Phi = \frac{4\pi(d/2)^2\phi}{\frac{4}{3}\pi(d/2)^3} = \frac{3\phi}{2d} \quad (5-15)$$

It can be seen that the divergence of DEM and ATA starts at more or less the same interface density Φ , as marked with an olive vertical dash line, indicating that the interface density instead of the volume fraction is the determinate factor of evaluating the intensity of grain boundary scattering.

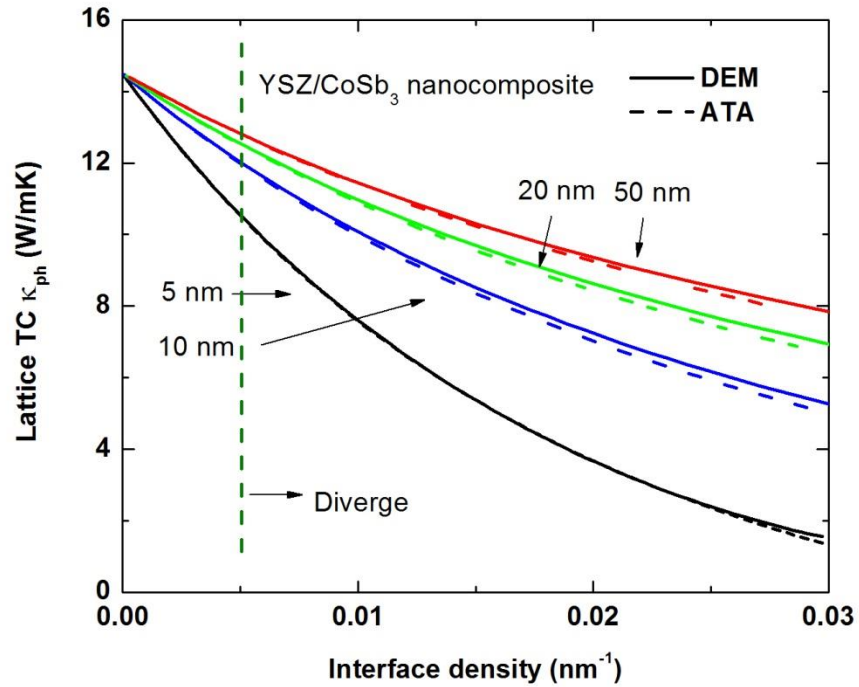


Figure 5-4 Lattice thermal conductivity dependence on interface density Φ , in YSZ/CoSb₃ nanocomposite at 300K, the grain size is equal to 50,20,10 and 5 nm separately.

Both ATA and DEM discussed above deal only with independent-particle scattering, without considering multiple scattering effect, as shown in Figure 5-5. As the volume fraction ϕ of second phase increases, modification has to be made to account for the important multiple scattering effect.

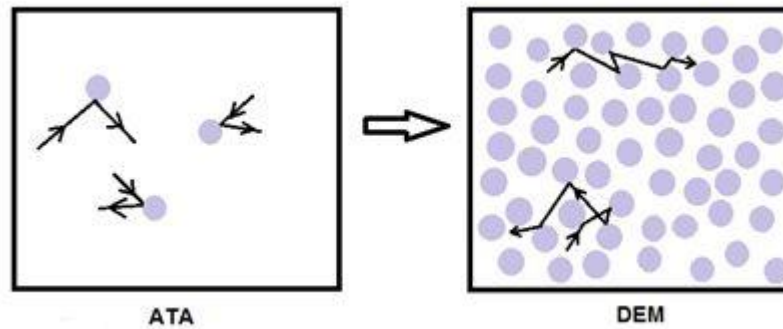


Figure 5-5 Independent-particle scattering in low volume fractions vs. multiple scattering in high volume fractions.

5-4 DEM with inherently implemented multiple scattering

Presented in Figure 5-5 are configurations of independent scattering at dilute volume fractions and multiple scattering at high volume fractions. At high volume fractions, the configuration can be taken as the core-shell structure as discussed in chapter 4. The core-shell configuration can be formulated by replacing the host materials with nano-inclusions gradually. As the amount of these nano-inclusions increases, the matrix material eventually behaves like shells surrounding the nanoparticles.

The average thickness of the shells is evaluated by the parameter t , which is defined as $t = d(1 - \phi^{1/3})/\phi^{1/3}$. This definition comes from the approximate volume fraction of the spherical nano-inclusions $\phi = (d/(d+t))^3$. As the volume fraction ϕ increases, the average thickness t of the shells decreases; phonon-

particle scattering in the host thus occurs more often within the inter-particle region. At this point, multiple phonon-particle scattering has to be considered and the relevant length scale that determines the scattering rate then changes from d to t . Qualitatively, there exists a crossover volume fraction ϕ_0 , above which $1/d < 1/t$. For $\phi \ll \phi_0$, the scattering is mostly independent-particle scattering and $F(\phi)$ is $3\phi/2$. For $\phi > \phi_0$, inter-particle boundary scattering becomes important. Setting $t=d$, ϕ_0 is found to be ~ 0.125 . Detailed calculation based on the spatial occupancy of particles and particle shape yields ϕ_0 in the range from ~ 0.1 for polyhedral dispersoids to ~ 0.2 for spherical dispersoids[107]. Considering experimental systems, it is feasible to adopt $\phi_0 \sim 0.15$ as a decent approximation. As ϕ keeps increasing and t becomes smaller than the phonon wavelength λ_h , the host no longer plays a significant role. This discussion allows for the alteration of the scattering function $F(\phi)$ to the following form.

$$F(\phi) = \left[\frac{3}{2} \cdot \phi \cdot e^{-\frac{\phi}{\phi_0}} + \frac{d}{t} \left(1 - e^{-\frac{\phi}{\phi_0}} \right) \right] \left(1 - e^{-\left(\frac{t(\phi)}{\lambda_h} \right)^2} \right) \quad (5-16)$$

This expression maintains the initial independent-particle scattering mechanism of $F(\phi)=3\phi/2$ at low volume fractions, changes to $F(\phi)=d/t$ beyond the crossover point ϕ_0 , and approaches zero as $\phi \rightarrow 1$. Figure 5-6 shows the comparison between $F(\phi)$ in the form of Eqn (5-16) and the independent-particle scattering of $3\phi/2$ for Si/ZrO₂ core-shell with particle size $d \sim 10$ nm. It can be expected that multiple phonon-particle scattering shall have a better suppression effect on lattice thermal conductivity than independent-particle scattering approximation, at both intermediate and high volume fractions.

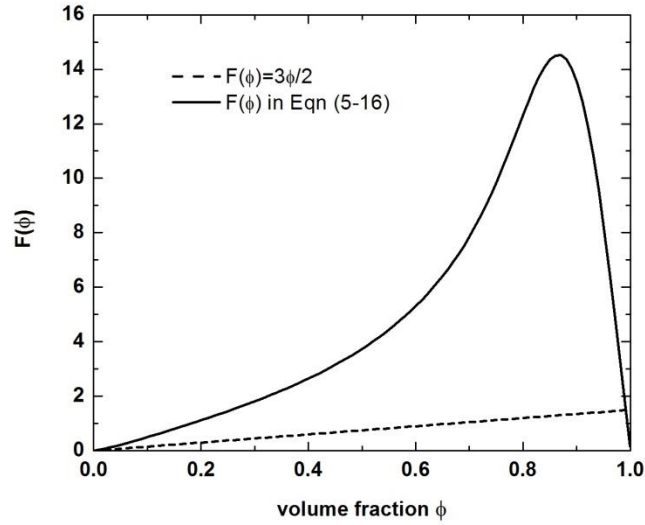


Figure 5-6 Comparison between multiple scattering and independent-particle scattering $3\phi/2$.

In Eqn (5-16), the characteristic wavelength λ_h was introduced to discuss the phonon scattering at the point when the length scale t is comparable with the phonon wavelength of the host. In the gray model, λ_h is independent on phonon frequency, considering $\omega \sim \sin(qa/2)$, $v_g \sim v_s \cos(qa/2)$, density of states $D(q) \sim 4\pi q^2$, and the characteristic phonon wavelength of the host can be estimated over the phonon spectral function as follows:

$$\langle \lambda \rangle = \frac{\int_0^{\pi/a} dq \frac{2\pi q}{e^{\hbar\omega/kT} - 1}}{\int_0^{\pi/a} dq \frac{q^2}{e^{\hbar\omega/kT} - 1}} \approx \frac{\int_0^{\pi/a} dq \frac{2\pi q}{\sin(\frac{qa}{2})}}{\int_0^{\pi/a} dq \frac{q^2}{\sin(\frac{qa}{2})}} = 1.18\pi a \text{ (for } kT \gg \hbar\omega) \quad (5-17)$$

Where a is the lattice constant, and the typical characteristic wavelength of the host is around 2 nm.

It is straightforward for one to choose the core and the shell materials so that they are chemically stable at operating temperatures and not soluble in each other. ZrO₂ and Yttria-stabilized-Zirconia (YSZ) are extremely unreactive and therefore are widely used as core or shell material. It is worth noting that these embedded nano-inclusions not only serve as phonon particle scattering centers but also play a significant role in suppressing grain growth of the host materials.

Effective lattice thermal conductivity of Si/ZrO₂ and Si₈₀Ge₂₀/YSZ core-shell nanostructures are presented in Figure 5-7 and Figure 5-8. Solid lines are DEM calculation with $F(\phi)$ in Eqn (5-16), which inherently incorporates multiple scattering, while dashed lines indicate DEM calculation with $F(\phi)=3\phi/2$, with independent-particle scattering assumption. The scattering intensity of Eqn (5-16) is compared with that of independent scattering as shown in Figure 5-6, at most volume fractions except the ending point where $\phi \sim 1$, multiple scattering should be more effectively than single particle scattering. Closely packed core particles provide the configuration for multiple particle scattering, and hence cause more remarkable reduction in lattice thermal conductivity than the independent particle scattering approximation. Indeed, as shown in Figure 5-7 and Figure 5-8, DEM calculation with inherently implemented multiple scattering effects always has lower lattice thermal conductivity than its counterpart with $F(\phi)=3\phi/2$. As ϕ increases from 0 to $\phi_0 \sim 0.15$, the concentration of nano-inclusions is still dilute, only independent-particle scattering needs to be considered. As ϕ keeps increasing, the distance between embedded particles decreases and multiple phonon-particle scattering starts to dominate, as represented by the term $(1-\exp(-\phi/\phi_0))$. It is interesting to observe a minimum value of thermal conductivity close to the point of $\phi \sim 1$. The scattering can be assumed to be hard-sphere scattering as long as the width of the inter-particle distance t and the particle size d satisfy $t \gg \lambda_h$ and $d \gg \lambda_h$.

However, as the scattering length scale (t or d) decreases to the point where phonons with wavelength λ_h can no longer penetrate, the thermal conductivity will vanish,[119] which unfortunately conflicts with realistic physical observations; the last factor $1-\exp(-(t/\lambda_h)^2)$ in Eqn (5-16) was thus introduced to avoid this contradiction. At different particle size d , the minimum lattice thermal conductivities correspond to different volume fractions ϕ , but they are all at almost the same shell thickness t , as shown in Figure 5-7 and Figure 5-8. This indicates that, at this region, it is the length scale t that determines the scattering mechanism. When the length scale of the system is even smaller than the average phonon wavelength, hard-sphere scattering is no longer valid, and the scattering mechanism will approach Rayleigh scattering regime. The authenticity of this introduced factor $1-\exp(-(t/\lambda_h)^2)$ is still pending, but it provided an intuitive picture that a minimal lattice thermal conductivity can be reached at some shell thickness t close to λ_h . Rigorous calculations must be conducted in the future to ascertain the scattering mechanism at this length scale.

Table 5-2 Parameter used in the core-shell systems of Si/ZrO₂ and Si₈₀Ge₂₀/YSZ, at T=1100K.

composites	Debye θ_D (K)	κ_{bulk} (W/(m*K))	C_p (10 ⁶ J/m ³ K)	V_s (m/s)	V_g (m/s)	MFP(nm)
Si/ZrO ₂ [103], [108]	645/590	31.2/2.2	2.07/3.58	5961/3591	2265/1365	19.96/1.35
Si ₈₀ Ge ₂₀ /YSZ[108], [115], [116], [117]	586.8/527	2.6/1.7	2.14/3.27	5166/3737	1963/1420	1.86 /1.10

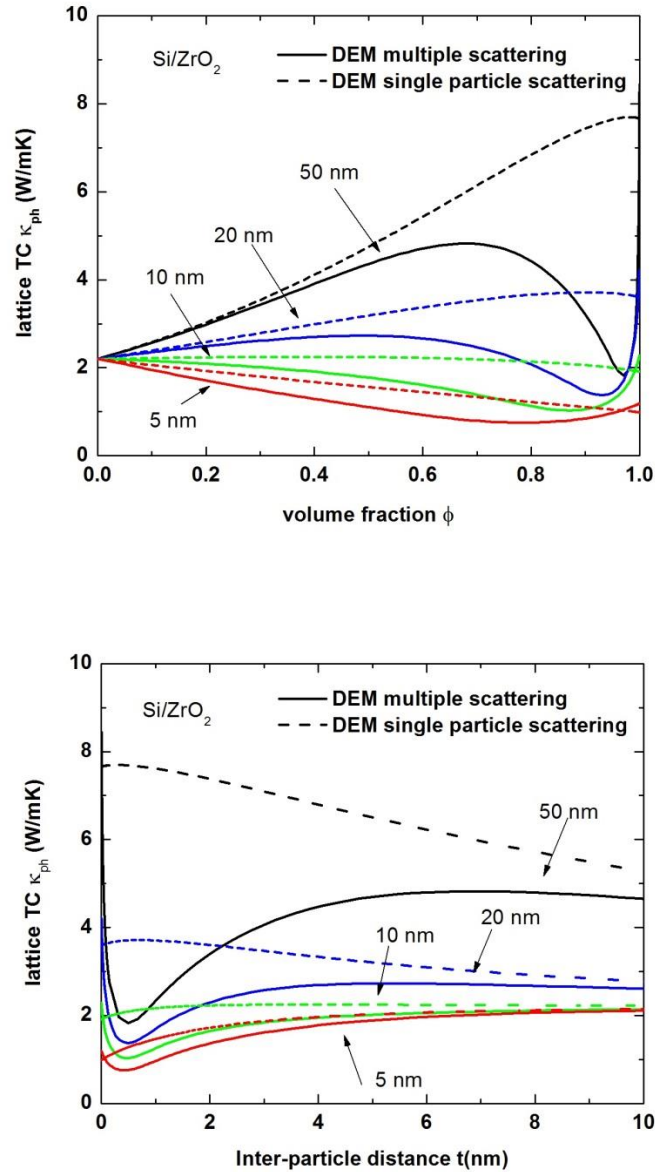


Figure 5-7 DEM Calculated lattice thermal conductivity $k^*(\phi)_{DEM}$ with $F(\phi)$ in Eqn (5-16)-multiple scattering and $F(\phi)=3\phi/2$ -independent particle scattering in core-shell structure of Si/ZrO₂ at grain size $d=50, 20, 10$ and 5 nm.

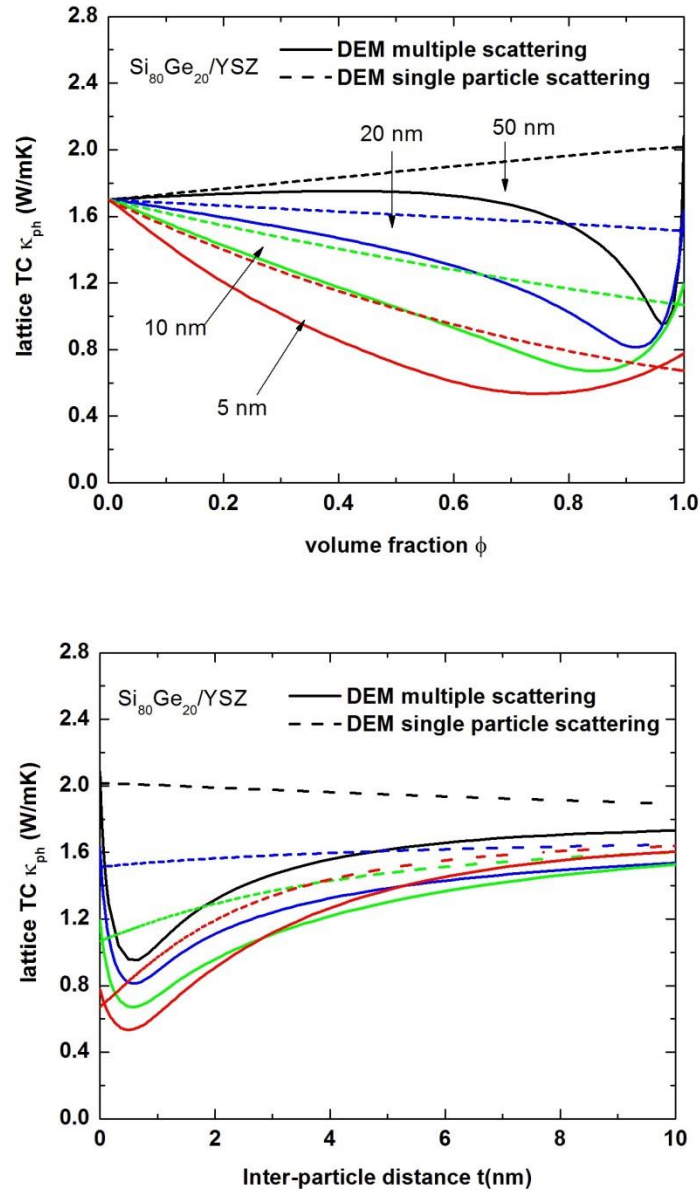


Figure 5-8 DEM Calculated lattice thermal conductivity $k^*(\phi)_{\text{DEM}}$ with $F(\phi)$ in Eqn (5-16)-multiple scattering and $F(\phi)=3\phi/2$ -independent particle scattering in core-shell structure of $\text{Si}_{80}\text{Ge}_{20}/\text{YSZ}$ at grain size $d=50, 20, 10$ and 5 nm.

At the ending point where $\phi=1$, a monolithic nanostructure composed solely of core nanoparticles is formed; the exact value of its effective lattice thermal conductivity can then be derived from Eqn (5-12). The different ending points in DEM using multiple scattering function and independent particle scattering can be explained as follows. As $\phi \rightarrow 1$, in the case of multiple scattering $F(\phi)=\text{Eqn (5-16)}$, the second term in the parentheses diminishes. The convergence of $dk(\phi)$ at $\phi=1$ then requires the numerator of the first term in the parentheses to be zero:

$$k_p(1 - \alpha(1)) - k(1) = 0 \quad (5-18)$$

Where $k_p=k_{p0}/(1+l_p/d)$, and thermal resistance parameter $\alpha(1)=k_h(1)R(1)/(d/2)$. Considering $\phi=1$, $k_h(1)=k(1)$, $R(1)=4(c_p v_p + c_p v_p)/c_p v_p c_p v_p = 8/c_p v_p = 8l_p/3k_{p0}$, [113] Eqn (5-18) can then be written as:

$$\frac{k_{p0}}{1 + \frac{l_p}{d}} \left(1 - \frac{k(1)}{k_{p0}} \frac{16 l_p}{3 d} \right) = k(1) \quad (5-19)$$

With the terms arranged, $k(\phi)$ at $\phi=1$ can eventually be obtained:

$$k(1) = \frac{k_{p0}}{1 + \frac{19 l_p}{3 d}} \quad (5-20)$$

The lattice thermal conductivity of the monolithic nanostructure has nothing to do with the host materials, and it decreases monotonically as the grain size d decreases.

For independent particle scattering, when $F(\phi)=3/2$ at $\phi=1$, similar calculations give the ending point of the monolithic nanostructure as:

$$k(1) = \frac{\sqrt{\left(1 + \frac{41l_p}{6d}\right)^2 + 4\frac{l_p}{d}\left(1 + \frac{19l_p}{3d}\right) - \left(1 + \frac{41l_p}{6d}\right)}}{\frac{2l_p}{d}\left(1 + \frac{19l_p}{3d}\right)} k_{p0} \quad (5-21)$$

Although the novel core-shell structure helps to suppress the lattice thermal conductivity of TE materials by increasing the phonon-boundary scattering, the existence of the heterogeneous phase and associated defects can also impede charge carriers' transport, resulting in an increased electrical resistivity and might eventually leading to a reduced overall ZT. One possible solution is to use the same material for both cores and shells; that is, to construct the nanocomposite with a mixture of nano-sized grains with different grain sizes. An alternative is to generate in-situ nanoparticles via phase segregation, since in-situ formed nanophase has close electrical and thermal properties to those of the matrix material; in this case, the effect of incoherent boundaries between the core and the shell to impede charge carriers' transport is thus weakened. Examples of in-situ formed Full Heusler/Half Heusler and PbSe/PbS nanocomposites will be discussed in the next section.

5-5 Effective scattering cross section

The prerequisite of hard particle scattering assumption is that the scattering length scale (t or d) is much larger than the characteristic wavelength λ_h ($\sim 2\text{nm}$); based on this assumption, the scattering cross-section of an embedded spherical nanoparticle is its projected area $\pi d^2/4$. Corresponding calculations are presented in the last sections, both in independent-particle scattering regime and multiple scattering regime. However, the dramatic drop in lattice thermal conductivity observed in experiments, especially at low volume fractions of a second phase, doesn't match the simulations above very well; thus, phonon scattering must still be underestimated to some extent. Inspired by Kim *et al.*, [110] we implemented the much more rigorously calculated effective scattering cross section σ_{eff} , as well as grain size dispersion, into the DEM simulation to achieve a better agreement with both the MC simulation by Jeng [102] and the experimental results. [111]

5-5-1 Scattering cross section

The Mie solution to Maxwell's equation [120], [121] depicts that when electromagnetic waves encounter spherical particles the scattering cross section varies from $\sim \omega^4$ of Rayleigh regime to frequency independent geometric regime (Rayleigh-Gans-Debye scattering) as size factor $\chi = qR$ (R is the wave number, and R the particle radius) changes from one extreme of $\chi \ll 1$ to the other of $\chi \sim \infty$. Ying and Truell *et al.* [122], [123] extended this treatment and derived the scattering cross section of a phonon wave off spherical particles in a solid. Despite the relative simple form of cross sections σ_{eff} for the two extreme cases, it is fairly difficult to establish relationships between σ_{eff} and the scattering parameters in a more general case, where particle size d is comparable with the incoming wavelength λ ,

due to the mathematical complexity. Majumdar[124] bridged the scattering cross section of two extremes and proposed the effective cross-section σ_{eff} for the intermediate χ to be :

$$\sigma_{\text{eff}} = \pi \left(\frac{d}{2} \right)^2 \frac{\chi^4}{\chi^4 + 1} \quad (5-22)$$

As the size factor $\chi \rightarrow 0$, and the particle size $d \ll$ incoming wavelength λ , Eqn (5-22) becomes $\sigma_{\text{sct}} \rightarrow \pi(d/2)^2 \chi^4 \sim \omega^4$, which is exactly the Rayleigh scattering; while $\chi \rightarrow \infty$, and $\lambda \ll d$, resulting in a frequency independent cross-section $\sigma_{\text{sct}} \rightarrow \pi(d/2)^2$ in the near geometric scattering regime. This method is correct in describing the two extreme cases, but insufficient to depict the vibration behavior of scattering cross section at an intermediate size factor χ . Kim and Majumdar, in a later work,[110] rigorously calculated scattering cross section in two extreme regimes and suggested to bridge them together as:

$$\sigma_{\text{total}}^{-1} = \sigma_{\text{Rayleigh}}^{-1} + \sigma_{\text{near geometric}}^{-1} \quad (5-23)$$

The effective cross section in the Rayleigh regime σ_{Rayleigh} is shown to be proportional to χ^4 with the magnitude determined by mass and force difference ($\Delta M/M$ and $\Delta K/K$ respectively) between embedded and host materials and, when χ approaches 0, $\sigma_{\text{Rayleigh}} \sim \chi^4 \rightarrow 0$, as the Rayleigh limit does. The second term $\sigma_{\text{near-geometric}}$ accounts for the near geometric regime scattering, and its strength is proportional to $2\pi(d/2)^2$ multiplied by an oscillating factor, which approaches 1 when $\chi \gg 1$. Scattering in the near geometric regime was first well studied by van de Hulst[121] for electromagnetic waves. The total effective scattering cross section σ_{total} , determined by the inverse sum of cross sections at two

extreme regimes, approaches 0 when χ is infinitesimal and increases to a certain value before starting to oscillate with χ . The oscillating factor then fades away as χ increases and eventually σ_{total} retains around $2\pi(d/2)^2$. A more intuitive plot is well presented by Kim and Majumdar,[110] which is validated by our calculation. It is worth noting that the scattering cross section reaches twice the projected area of a spherical nanoparticle at $\chi \rightarrow \infty$, which can be understood in the sense that scattering always occurring at the edges of the nanoparticles enlarges the scattering cross section due to diffraction.[120]

To calculate the effective scattering cross section at certain particle size factor χ , the wavenumber $q=\chi/d$ needs to be evaluated. For acoustic phonon branch, the group velocity is given by $v_g \sim v_s \cos(qa/2)$ and the frequency $\omega \sim \sin(qa/2)$, where v_s is sound speed at $q=0$ and a is the lattice constant. The average wavenumber in host material can then be estimated by averaging v_g over the phonon spectrum $D(q)$ or spectral function $D(q)\langle n \rangle \sim q^2/(\exp(\hbar\omega/kT)-1)$, where $D(q)=4\pi q^2$ is the phonon density of states and $\langle n \rangle = 1/(\exp(\hbar\omega/kT)-1)$ the phonon distribution function:

$$\left\{ \begin{array}{l} \langle q \rangle = \frac{\int_0^{\pi/a} dq q^3 \frac{1}{e^{\hbar\omega/kT}-1}}{\int_0^{\pi/a} dq q^2 \frac{1}{e^{\hbar\omega/kT}-1}} \approx \frac{\int_0^{\pi/a} dq \frac{q^3}{\sin(\frac{qa}{2})}}{\int_0^{\pi/a} dq \frac{q^2}{\sin(\frac{qa}{2})}} = \frac{2.19}{a} \quad (\text{for } kT \gg \hbar\omega) \\ \langle q \rangle = \frac{\int_0^{\pi/a} dq q^3}{\int_0^{\pi/a} dq q^2} \approx \frac{2.36}{a} \end{array} \right. \quad (5-24)$$

Calculated average wavenumbers ($q \sim 2.25/a$) for several composites are listed in Table I. In realistic systems, acoustic phonons, which dominate heat transfer at temperature of interests (300~1200K), bear a characteristic wavelength $\lambda \sim 2$ nm. The relative small value of λ when compared with the nanoparticle size (generally greater than 3~5 nm), eventually yields $\sigma_{\text{eff}} \approx \sigma_{\text{near-geometric}}$, as a fair approximation.

5-5-2 Grain size dispersion

Experiments have shown that nanoparticle sizes in most nanocomposites spread from a few to hundreds of nanometers[125], [126] rather than being fixed at constant value as used in models. In theory, a system of nanoparticles containing a wide size dispersion is capable of scattering off phonons of different wavelengths over the spectrum thus rendering it more effective than its counterpart with a constant grain size.[11] Jeng *et al.* [102] argued that further randomness of grain size distribution doesn't help to reduce lattice thermal conductivity with MC simulations, which is fairly true to some extent, however, in later simulations, scattering cross section increases at a larger grain size standard deviation, eventually leads to a considerably lower κ_{ph} . The effective scattering cross section with a normalized grain size distribution function $F(x)$ can be expressed as:[110]

$$\sigma_{eff} = \int_{d_{min}}^{d_{max}} \sigma_{total}(x)F(x)dx \quad (5-25)$$

where d_{min} and d_{max} are the lower limit and upper limit of grain size individually. Presented in Table II are 5 distribution functions and their corresponding effective scattering cross sections. F_1 is for nanoparticles with a constant diameter, F_2 and F_3 are even distributions over different ranges, F_4 and F_5 are normalized Gamma distributions with $ab = \text{mean diameter } d_0$ and $a^{1/2}b = \text{standard deviation}$ (shape parameter $a=12$, scale parameter $b=d_0/12$ in F_4 ; $a=3$, $b=d_0/3$ in F_5). F_2 and F_3 are presented in order to show that it is universal that grain size dispersion results in increased effective scattering cross section. In this article, Gamma distributions of F_4 and F_5 are adopted without losing generality.

Table 5-3 – Size dispersion function dependence effective scattering cross section for ErAs/In_{0.53}Ga_{0.47}As nanocomposite with average ErAs grain size $d_0=10\text{nm}$. F_1 is a delta function, F_2 and F_3 are even distributions, and F_4 and F_5 are Gamma distributions with shape parameter $a=12$, scale parameter $b=d_0/12$ and $a=3$, $b=d_0/3$ respectively. ^(a) Numerical calc. by Eqn(5-25), ^(b) simplified σ_{eff}^* in Eqn(5-26).

Distribution Function $F(x)$	diameter size range	stdev	numerical calc. ^(a) $\sigma_{\text{eff}}/(\pi d^2/4)$	Simplified ^(b) $\sigma_{\text{eff}}^*/(\pi d^2/4)$	Percentage difference (%)
$F_1(x)=\delta(x-d)$	d	0	1.89	2	5.5
$F_2(x)=\frac{1}{d}$	$d/2\sim 3d/2$	$\frac{d}{2\sqrt{3}}$	2.31	13/6	6.6
$F_3(x)=\frac{2}{3d}$	$d/4\sim 7d/4$	$\frac{d}{\sqrt{3}}$	2.46	19/8	3.6
$F_4(x)=\frac{x^{a-1}e^{-x/b}}{b^a\Gamma(a)}$	$0\sim\infty$	$\frac{d}{2\sqrt{3}}$	2.16	13/6	0.3
$F_5(x)=\frac{x^{a-1}e^{-x/b}}{b^a\Gamma(a)}$	$0\sim\infty$	$\frac{d}{\sqrt{3}}$	2.56	8/3	4.0

The explicit form of Eqn(5-25) is unlikely to be derived due to the complexity of σ_{total} depending on spherical particle diameter d or size factor χ , resulting in the inevitability of numerical calculations. However, for systems whose related parameters (force constants for instance) are unavailable, a simplification shall then be made to estimate the effective scattering cross section. In most realistic cases, the lower limit of obtainable grain size is around 3~5nm, with the characteristic average wavenumber q assumed to be 4 nm^{-1} (refer to table I), thus χ always lies above 15~20. This lower limit of size factor falls into the region where scattering efficiency $\sigma_{\text{sct}}/\pi(d/2)^2$ weakly oscillates around 2,[110] hence the

approximation of $\sigma_{\text{sct}} = \sigma_{\text{near-geometric}} = \pi d^2/2$ won't result in a significant deviation from rigorous calculation via Eqn (5-25). Estimated effective cross section σ_{eff}^* can then be derived from the simplified integration:

$$\sigma_{\text{eff}}^* = \int_{d_{\text{min}}}^{d_{\text{max}}} \frac{1}{2} \pi x^2 F(x) dx \quad (5-26)$$

The authenticity of this approximation is validated by comparing explicit integration of Eqn (5-26) with numerical calculation of Eqn (5-25) in ErAs/In_{0.53}Ga_{0.47}As system discussed by Kim *et.al.*, [110] and the differences are found to be within 6%, as shown in Table II. The tiny difference between simplified and rigorous integrations indicates that near geometric scattering dominates phonon scattering for nanoscaled grains. It is also shown that increasing grain size dispersion tends to result in enlarged effective scattering cross section, and thus reduced lattice thermal conductivity. A calculation within Callaway model has depicted similar features. [101]

5-5-3 Validation of effective scattering cross section treatment in DEM

Here, we present the DEM approach with the updated effective scattering cross section calculated by Eqn (5-26), and show that the calculated results turn out to have a better fit with Jeng *et al.* gray model MC simulation.

Parameters used in the DEM calculation are listed in Table 5-1. Presented in Figure 5-9 are comparisons of various simulations on Si nanoparticles ($d_0=10\text{nm}$) embedded Ge bulk matrix. It can be concluded that (1) Nan's EMA gives highest effective lattice thermal conductivity, due to not

considering grain size effect on interface scattering, (2) DEM simulations with the effective scattering cross sections discussed above result in faster drops of κ_{ph} at low volume fractions, compared with Minnich's EMA model which utilizes spherical nanoparticle's projected area $\pi d^2/4$ as scattering cross section, (3) DEM simulations with the effective scattering cross sections agree well with Jeng's gray model MC simulations, which is supported by experimental results,[127] (4) 15% decrease in κ_{ph} at $\phi=0.1$ is found in DEM simulations, as the standard deviation of grain size increases from 0 to 5.77nm, which strongly indicates that nanoinclusions with larger grain size dispersion are more effective in blocking thermal transfer in a solid.

Table 5-3 Parameters of different composites used in this work, at room temperature T=300K.

composites	Bulk κ (W/mK)	Debye T θ_D (K)	c_p (10^6 J/m ³ K)	v_s (m/s)	Avg. v_g (m/s)*	MFP (nm)*	$\langle q \rangle_{host}$ (nm ⁻¹)*	Lattice a(nm)
Si/Ge[113], [128]	150/51.7	645/360	1.66/1.67	6400/3900	2432/1482	110.4/64.1	3.99	0.565
PbS/PbSe[54], [111], [129]	2.4/1.9	145/141	1.58/1.44	2040/1910	775/726	5.88/5.45	3.67	0.612
FH/HH[130], [131], [132]	7.2 ^a /10.1	318/390	2.29/2.03	2639 [#] /3498	1003/1329	10.4/11.3	3.68	0.611

FH=ZrNi₂Sn, HH=ZrNiSn. * represent calculated values, ^a is estimated by $\kappa \sim 1/\rho$ (this approximated relationship is derived from experimental data in Ref. [47], [133]).

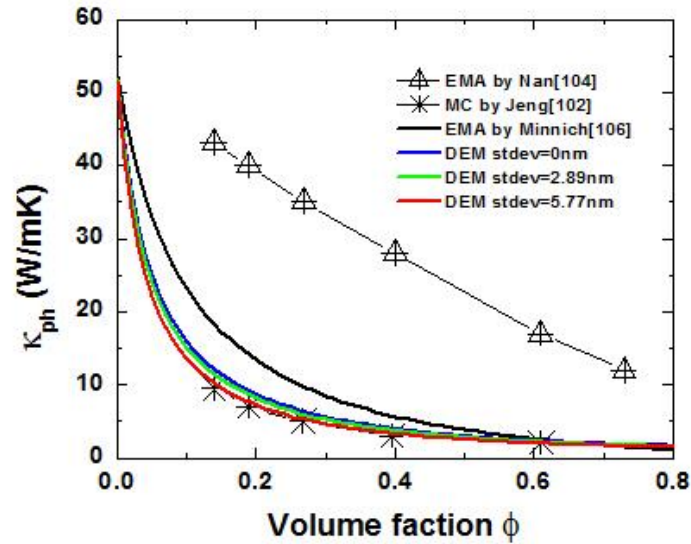


Figure 5-9 Lattice thermal conductivity κ_{ph} of Si/Ge nanocomposite dependence on Si nanoparticles' volume fraction ϕ at 300K, with an average grain size of $d_0=10\text{nm}$. DEM simulations with different grain size dispersions (blue-fixed grain size $d=d_0$, green-standard deviation of $0.289d_0$ and red-standard deviation of $0.577d_0$) are compared with Nan's EMA (triangles), Minnich's EMA (black solid line) and Jeng's MC simulation (asterisks).

5-5-4 Comparison with PbS-PbSe nanocomposite

Lead chalcogenides, PbTe, PbSe and PbS, have been extensively studied over the past decades as promising TE materials, mainly due to the unique features of outstanding electrical transport properties and unusually low thermal conductivities at high temperature. In-situ phase separation process of these

Lead chalcogenides systems via post-annealing was well studied and able to be manipulated, meanwhile, the reduction effect on lattice thermal conductivity in in-situ formed nanocomposite was found more pronounced than in its solid solution analogue.[134]

Androulakis *et al.*[111] presented a systematic study on lattice thermal conductivity of PbS-PbSe binary with PbS concentration up to 16%, the observed lattice thermal conductivity at room temperature was about 15% lower than calculation based on Klemens-Drabble (KD) theory for solid solution.[50], [52] The extra reduction in lattice thermal conductivity was explained by nanostructured morphology of in-situ generated PbS nanoparticles (~5nm) in PbSe solid solution. Lattice thermal conductivity of PbS/PbSe nanocomposite calculated with DEM for distribution function $F(x)=F_5(x)$ is compared with KD theory and experimental data, as depicted in Figure 5-10. DEM presents consistently lower lattice thermal conductivity than KD theory, indicating nanoparticle interface scattering is much more effective in reducing thermal conductivity than point defect scattering of solid solution alloying. The measured data lie in between KD theory for solid solution and DEM calculation for complete nanocomposite, indicating incomplete phase separation, which was observed both on samples that were quenched and those post-annealed at 900K.

It is worth noting that the DEM was introduced as a frequency (wavelength) independent gray model, and when extended to atom scale to account for the point defect scattering, would cause a significant deviation in scattering effectiveness. When the grain size is much larger than the characteristic wavelength λ (~1nm), frequency independent near-geometric scattering dominates, and gray model assumption does hold in this circumstance. However, as the grain size decreases to the scale

of λ , Rayleigh scattering, which strongly depends on phonon frequency, becomes the determining factor, therefore, the frequency independent gray model is no longer a reasonable assumption. In order to accurately capture the phonon scattering features at this scale, a frequency (wavelength) dependent non-gray model is eventually necessary. A possible strategy utilizing DEM to handle the incomplete phase separation in PbS/PbSe system could be: take the solid solution of host PbSe and dissolved PbS as a “new host”, whose lattice thermal conductivity can either be obtained from experimental results or KD theory; meanwhile, treat the undissolved PbS nanoparticles as phonon scattering centers as usual, but of a smaller volume fraction (total volume fraction subtracts the dissolved portion). Unfortunately, this strategy is not feasible to be performed in this article, since neither the PbS dissolution ratio nor its dependence on total PbS volume fraction and temperature is available.

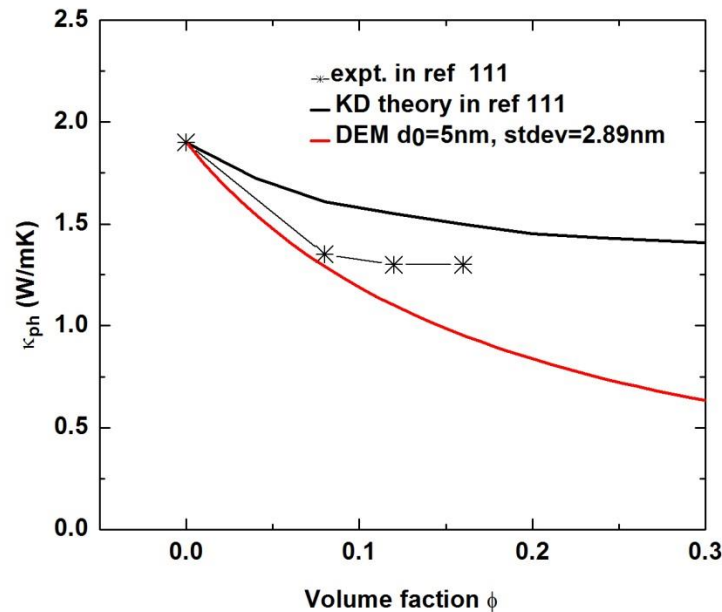


Figure 5-10 Lattice thermal conductivity κ_{ph} of PbS/PbSe nanocomposite dependence on PbS nanoparticles' volume fraction ϕ at 300K, the comparisons are performed among experimental data (black asterisks), KD theory for solid solutions (black line) and DEM simulations with grain size distribution function $F_5(x)$ (red line).

While it is comprehensible that incomplete phase separation happens in quenched samples, which to a great extent retain the solid solution state at high temperature, post-annealed process at a temperature as high as 900K may cause PbS to partially re-dissolve in PbSe matrix on the other hand. Similar temperature sensitive re-dissolving process was reported for PbS-PbTe system.[135] Based on the discussion, post-annealing at a proper temperature to allow thorough phase separation is necessary to form in-situ nanostructures which can effectively scatter acoustic phonons, leading to reduction in thermal conductivity and therefore enhancement in dimensionless figure of merit ZT. Further increase of the second phase, however, won't lead to a continuous reduction of thermal conductivity, since above certain volume fraction (for instance, >30% for PbTe/PbS system), nanoparticles of second phase tend to aggregate into microscale or even larger precipitates,[135], [136] which is not favored for effective phonon scattering.

5-5-5 Prediction on ZrNi₂Sn/ZrNiSn Full Heusler-Half Heusler nanocomposite

Similar to the lead chalcogenides systems,[129] Half Heusler(HH) alloys are also a well-studied series of TE materials with decent performance at high temperature[40], [41], besides, they are low-cost and nontoxic. The thermoelectric performance of Half Heusler is mainly limited by its comparably high

thermal conductivity. Recently, several interesting works showed improvement on Seebeck coefficient, electrical conductivity as well as reduction on lattice thermal conductivity by introducing nano-sized Full Heusler(FH) particles into HH host.[137], [138], [139] However, due to the difficulty in controlling phase separation in experiments, these researches did not show a systematic reduction in lattice thermal conductivity as the content of FH phase increases.

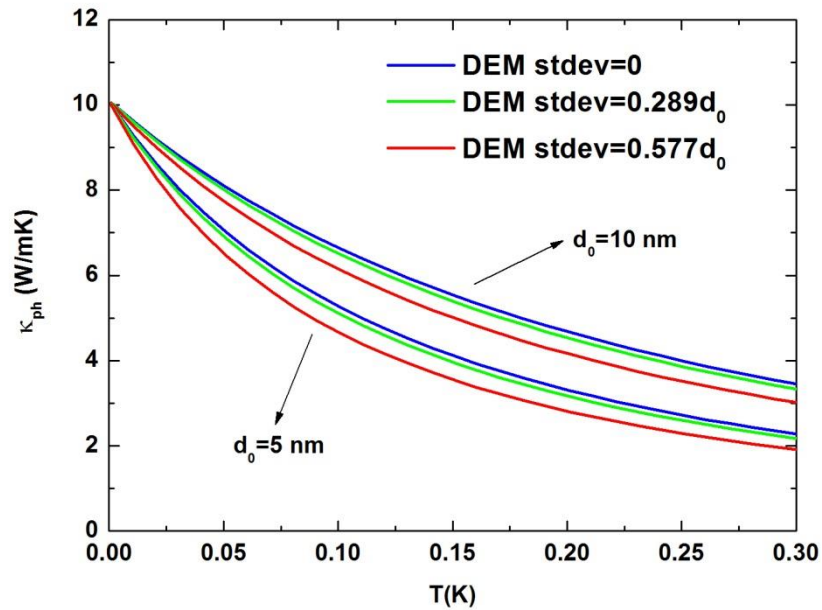


Figure 5-11 Dependence of lattice thermal conductivity κ_{ph} of ZrNi₂Sn/ZrNiSn nanocomposite on ZrNi₂Sn nano phase's volume fraction ϕ at 300K. Two series of plots are presented corresponding to average grain size $d_0=5$ nm and 10 nm individually, DEM simulations for different grain size dispersions are distinguished by colors (blue-fixed grain size, green-standard deviation of $0.289d_0$ and red-standard deviation of $0.577d_0$).

A prediction based on DEM calculation is presented herein to help quantitatively analyze the reduction on lattice thermal conductivity one might earn from in-situ nano FH generation in HH matrix, as shown in Figure 3. Host HH material is chosen to be ZrNiSn, and FH phase ZrNi₂Sn, corresponding parameters used in calculation are listed in Table I. Gamma distribution is utilized to simulate grain size dispersion with standard deviation of $0.289d_0$ and $0.577d_0$ separately, with mean grain sizes d_0 set to be 5nm and 10nm. Over 50% reduction on lattice thermal conductivity can be achieved by introducing only 10% ZrNi₂Sn nano phases with mean grain size d_0 of 5nm, and 40% reduction by $d_0=10$ nm. Meanwhile, electrical conductivity could be enhanced since embedded metallic FH phases also acts as carrier suppliers. What is more, enhancement on Seebeck coefficient may be gained[137], [138] from the so-called energy filter effect, specifically, low energy carriers which are believed to be detrimental to Seebeck coefficient tend to be trapped at the interfaces between nanoparticles and main matrix[140]. Similar trend of reduction on lattice thermal conductivity in TiNi₂Sn/TiNiSn nanocomposites was reported by Birkel *et al.*[138]

5-5-6 Conclusions

A modified differential effective medium (DEM) calculation with effective scattering cross section proposed by Kim and Majumdar was conducted to simulate the dramatic lattice thermal conductivity reduction when nanoparticles are evenly embedded into bulk host materials. It was then validated by comparing with Monte-Carlo simulation[102] of Si/Ge nanocomposite. The form $2^*K_{DEM}-K_{EMA}$, which inherently includes 2nd order phonon scattering, was recommended to replace the conventional single particle scattering at low volume fractions. The simulation was then performed on in-situ formed

PbS/PbSe nanocomposite, and the calculation was found to be in agreement with reported experimental results.[111] Finally, prediction on lattice thermal conductivity of ZrNi₂Sn(FH)/ZrNiSn(HH) nanocomposite was made in order to reveal the great promise of reducing lattice thermal conductivity via introducing secondary FH nanophase.

5-6 Summary and future work of effective medium approach

As an alternative to ab-initio simulations which require extensive computing time, effective medium approach (EMA), a phenomenological method, is widely used to evaluate the lattice thermal conductivity of heterogeneous two-phase systems. The derivations of Average T-matrix Approach (ATA) and Coherent Potential Approximation (CPA) were reviewed. Considering ATA and CPA both being limited to low volume fractions, a differential effective medium (DEM) was developed to enable calculation in the full range of second-phase concentrations from 0~1. Furthermore, multiple scattering, which dominates the high volume fraction region, was inherently implemented in DEM to replace the previous independent-particle scattering by utilizing scattering mechanism function $F(\phi)$ =Eqn (5-16) instead of $F(\phi)=3\phi/2$. This treatment led to an interesting minimal lattice thermal conductivity at ϕ close to 1. The physical meaning was then discussed. Hard particle scattering with scattering cross section as the projected area of spherical grain $A=4\pi(d/2)^2$ was widely used, because embedded particles' grain sizes were much larger than characteristic wavelength of phonons of host in most cases; however, as the grain size decreases to be comparable with phonon wavelength in host, scattering cross section A

needs to be reconsidered. A modification based on rigorous calculations of effective scattering cross-section was suggested, and the corresponding calculations were found to be close to Monte-Carlo simulation and experimental results. Some inspiring predictions on in-situ formed Full Heusler/Half Heusler nanocomposites were proposed to demonstrate the obtainable reduction of lattice thermal conductivity via nanostructuring technique.

Although DEM with multiple scattering inherently considered is taken as an improvement over DEM with independent particle scattering, the treatment of phonon scattering at volume fraction $\phi \sim 1$ in Eqn (5-16) still needs further investigation. It is mainly the gray model assumption that phonon wavelength or frequency is constant causing the inefficiency of DEM in explaining the scattering when inter-particle distance is extremely small. For future work, a non-gray model shall be implemented into the DEM calculation, according the frequency dependent scattering cross section; by evaluating the effective contribution from each frequency via DEM, the total thermal conductivity can be obtained by integrating over all frequencies provided that the frequency distribution function and phonon dispersion relations are available.

6. Conclusions

Nanostructuring techniques have been utilized to effectively reduce the relatively high lattice thermal conductivity and to enhance the thermopower in Half Heusler and SiGe alloys. The mechanisms have been discussed and attributed to the enhanced phonon scattering intensity and the energy barrier filtering effect respectively. Nanocomposites have been synthesized with high energy mechanic alloying followed by Spark Plasma Sintering (SPS) consolidations. To conclude, figure of merit $ZT=1.0$ at 850K and $ZT=0.85$ at 1050K were achieved in nanostructured Half Heusler alloys of N-type and P-type respectively, while $ZT=1.2$ at 1050K and $ZT=0.75$ at 1123K were obtained in nanostructured SiGe alloys of N-type and P-type individually. Severe grain growth might arise during the pulsed direct current internal heating SPS process, embedding foreign nanophases and constructing core-shell structures are both proven to be effective means to suppress grain growth, due to introduced incoherent grain interfaces; however, significant degradation in electrical conductivity arises because the embedded nanophases are insulating. To solve the problems, our future work can be expanded as follows:

The existence of a foreign nanophase is favorable to achieve low lattice thermal conductivity; however, direct mixing foreign nanoparticles into the host thermoelectric material usually leads to an uneven dispersion; specifically, most foreign nanoparticles tend to aggregate at matrix grain boundaries and can't effectively scatter acoustic phonons, which dominate heat transport in most temperatures of interest. Even dispersion of second phase can be achieved by in-situ phase segregations in a solid

solution. Like lead chalcogenides (PbTe/PbSe/PbS) systems, in which phase segregation can be well manipulated by proper post-annealing processes, in-situ Full Heusler(FH)/Half Heusler(HH) nanocomposites can also be synthesized via post-annealing processes. Due to the semi-incoherent interfaces between FH and HH phases, the novel nanostructures should have the promise of reducing lattice thermal conductivity via grain boundary scattering and enhancing the thermopower via preferentially scattering the lower energy charge carriers, without highly degrading the electrical conductivity.

Nanocomposites with core-shell structures are also proven to effectively reduce lattice thermal conductivity and enhance thermopower via incoherent boundary scatterings and energy filtering effect. It was observed that Si nanopowders became oxidized and thus coated with SiO_x thin layers, whose thicknesses were determined by the exposure time and temperature to oxygen. Other composites with similar core-shell structures could also be constructed with a wet chemical method. Using this method, core nanoparticles should be dipped into a certain chemical solution; reactions will then take place on the highly reactive surfaces of the nanoparticles. With well selected composite of the shell material (the conduction and valence band edges of core materials should lay well within the band gap of the shell) and adjustable shell thickness, reduced lattice thermal conductivity and enhanced thermopower can be achieved simultaneously without compensating on the electrical conductivity.

A phenomenological method of differential effective medium (DEM) was developed on the basis of conventional average T-matrix approximation (ATA), and utilized to evaluate the lattice thermal conductivity of heterogeneous two-phase systems, specifically nanocomposite systems (monolithic,

foreign nanophase embedded matrix and core-shell structures). The advantage of DEM over ATA is that DEM not only expands the applicability of the effective medium approach from small volume fractions to the whole volume range from 0 to 1, but also inherently includes the multiple scattering effect which dominates at high volume fractions but wasn't well considered in ATA with independent-particle scattering. The function used to account for multiple scattering stays valid till when the inter-particle distance between nanoinclusions decreases to the extent that is comparable with the incoming wavelength, after which point, the hard particle scattering assumption no longer holds, a modification has to be made in the future to better demonstrate the scattering at this region, most likely via the frequency dependent scattering. A revised effective scattering cross-section and the grain size dispersion effect have also been discussed in the regime of DEM, leading to a better agreement in lattice thermal conductivity with Monte-Carlo simulation and experiments in other groups.

This work has introduced the widely used nanostructuring techniques in thermoelectric materials fabrication. The dependence of thermoelectric properties on synthesis details was discussed. To avoid significant grain growth in the consolidation processes, nano-sized second-phase embedment and core-shell structures were performed and proved to be feasible. Improvements in figure of merit ZT due to reduced lattice thermal conductivity and enhanced thermopower were obtained, and the physical explanations were justified. Future work could be focused on fabricating in-situ formed nanophases in bulk TE materials and constructing in-situ core-shell nanostructures with adjustable shell thickness in order to realize the full potential of nanostructuring techniques in improving the thermoelectric performance.

7. Acknowledgements

The author owes his gratitude to Dr. S. J. Poon for the scientific guidance and financial support throughout these years, which are crucial for the author to complete his study and research. He also wishes to express his sincere thanks to his dissertation committee, Dr. S. Wolf, Dr. J. Lu, and Dr. E. Kolomeisky. He wishes to thank Dr. J.W. Simonson for his training on sample synthesis and usage of other laboratory utilities. He wishes to acknowledge S. Zhu, A. Lahwal, A. Mehdizadeh for their tremendous work in thermal conductivity and specific heat measurements, and A.S. Petersen, L. Chen for alloys synthesis. He would like to give the special thanks to Dr. T. M. Tritt for the generous support on lab facilities.

Reference

- [1] A. L. Rockwood, "Relationship of thermoelectricity to electronic entropy", *Physical Review A*, vol. 30, no. 5, pp. 2843–2844, 1984.
- [2] S. R. De Groot, *Thermodynamics of Irreversible Processes*. Amsterdam: North Holland, 1951.
- [3] H. B. A. Sommerfeld, *Elektronentheorie der Metalle*. Heidelberg: Springer Verlag, 1933.
- [4] G. Borelius, W. H. Keesom, C. H. Johansson, and J. O. Linde, *Proc. Acad. Sic. Amst.*, vol. 35, no. 10, 1932.
- [5] N. W. Ashcroft and N. D. Mermin, *Solid State Physics*. Philadelphia: Saunders, 1976.
- [6] E. Altenkirch, *Phys. Zeits.*, vol. 10, p. 560, 1909.
- [7] E. A. Altenkirch, *Phys. Zeits.*, vol. 12, p. 920, 1911.
- [8] T. M. Tritt and M. A. Subramanian, "Thermoelectric Materials, Phenomena, and Applications: A Bird's Eye View" *MRS Bull.*, vol. 31, no. 3, pp. 188–194, 2006.
- [9] J. P. Heremans, V. Jovovic, E. S. Toberer, A. Saramat, K. Kurosaki, A. Charoenphakdee, S. Yamanaka, and G. J. Snyder, "Enhancement of thermoelectric efficiency in PbTe by distortion of the electronic density of states," *Science (New York, N.Y.)*, vol. 321, no. 5888, pp. 554–7, Jul. 2008.
- [10] Y. Pei, H. Wang, and G. J. Snyder, "Band engineering of thermoelectric materials," *Advanced materials (Deerfield Beach, Fla.)*, vol. 24, no. 46, pp. 6125–35, Dec. 2012.
- [11] K. Biswas, J. He, I. Blum, and C. Wu, "High-performance bulk thermoelectrics with all-scale hierarchical architectures," *Nature*, vol. 489, no. 7416, pp. 414–8, Sep. 2012.
- [12] B. Poudel, Q. Hao, Y. Ma, Y. Lan, A. Minnich, B. Yu, X. Yan, D. Wang, A. Muto, D. Vashaee, X. Chen, J. Liu, M. S. Dresselhaus, G. Chen, and Z. Ren, "High-thermoelectric performance of nanostructured bismuth antimony telluride bulk alloys," *Science (New York, N.Y.)*, vol. 320, no. 5876, pp. 634–8, May 2008.
- [13] J. Androulakis, K. F. Hsu, R. Pcionek, H. Kong, C. Uher, J. J. D'Angelo, a. Downey, T. Hogan, and M. G. Kanatzidis, "Nanostructuring and High Thermoelectric Efficiency in p-Type $\text{Ag}(\text{Pb}_{1-y}\text{Sn}_y)\text{mSbTe}_{2+m}$," *Advanced Materials*, vol. 18, no. 9, pp. 1170–1173, May 2006.

- [14] C. Wood, *Rep. Prog. Phys.*, vol. 51, pp. 459–539, 1988.
- [15] G. S. Nolas, J. Sharp, and J. Goldsmid *Thermoelectrics-Basic principles and New materials development*. Springer, 2001.
- [16] M. Rowe, *CRC Handbook of Thermoelectrics*. Boca Raton: CRC, 1995.
- [17] X. W. Wang, H. Lee, Y. C. Lan, G. H. Zhu, G. Joshi, D. Z. Wang, J. Yang, a. J. Muto, M. Y. Tang, J. Klatsky, S. Song, M. S. Dresselhaus, G. Chen, and Z. F. Ren, “Enhanced thermoelectric figure of merit in nanostructured n-type silicon germanium bulk alloy,” *Applied Physics Letters*, vol. 93, no. 19, 193121, 2008.
- [18] X. Yan, G. Joshi, W. Liu, Y. Lan, H. Wang, S. Lee, J. W. Simonson, S. J. Poon, T. M. Tritt, G. Chen, and Z. F. Ren, “Enhanced thermoelectric figure of merit of p-type half-Heuslers.,” *Nano letters*, vol. 11, no. 2, pp. 556–60, Feb. 2011.
- [19] G. Zeng, J. M. O. Zide, W. Kim, J. E. Bowers, A. C. Gossard, Z. Bian, Y. Zhang, A. Shakouri, S. L. Singer, and A. Majumdar, “Cross-plane Seebeck coefficient of ErAs:InGaAs/InGaAlAs superlattices,” *Journal of Applied Physics*, vol. 101, no. 3, 034502, 2007.
- [20] K. Kishimoto, M. Tsukamoto, and T. Koyanagi, “Temperature dependence of the Seebeck coefficient and the potential barrier scattering of n-type PbTe films prepared on heated glass substrates by rf sputtering,” *Journal of Applied Physics*, vol. 92, no. 9, 5331, 2002.
- [21] G. Joshi, H. Lee, Y. Lan, X. Wang, G. Zhu, D. Wang, W. Ryan, D. C. Cuff, M. Y. Tang, M. S. Dresselhaus, G. Chen, Z. Ren, and R. W. Gould, “Enhanced Thermoelectric Figure-of-Merit in Nanostructured p-type Silicon,” *Nano. Lett.*, vol. 8, p. 4670, 2008.
- [22] Y. Ma, Q. Hao, B. Poudel, Y. Lan, B. Yu, D. Wang, G. Chen, and Z. Ren, “Enhanced thermoelectric figure-of-merit in p-type nanostructured bismuth antimony tellurium alloys made from elemental chunks.,” *Nano letters*, vol. 8, no. 8, pp. 2580–4, Aug. 2008.
- [23] H. Kim, T. Oh, and D. Hyun, “Thermoelectric properties of the p-type Bi₂Te₃-Sb₂Te₃-Sb₂Se₃ alloys fabricated by mechanical alloying and hot pressing,” *Journal of Physics and chemistry of solids*, vol. 61, pp. 743–749, 2000.
- [24] J. Yang, Q. Hao, H. Wang, Y. Lan, Q. He, A. Minnich, D. Wang, J. Harriman, V. Varki, M. Dresselhaus, G. Chen, and Z. Ren, “Solubility study of Yb in n-type skutterudites Yb_xCo₄Sb₁₂ and their enhanced thermoelectric properties,” *Physical Review B*, vol. 80, no. 11, 115329, Sep. 2009.

- [25] W. S. Liu, B. P. Zhang, J. F. Li, H. L. Zhang, and L. D. Zhao, "Enhanced thermoelectric properties in $\text{CoSb}_{3-x}\text{Te}_x$ alloys prepared by mechanical alloying and spark plasma sintering," *Journal of Applied Physics*, vol. 102, no. 10, 103717, 2007.
- [26] Q. He, Q. Hao, X. W. Wang, J. Yang, Y. C. Lan, X. Yan, B. Yu, Y. Ma, B. Poudel, G. Joshi, D. Z. Wang, G. Chen, and Z. F. Chen, "Nanostructured Thermoelectric Skutterudite $\text{Co}_{1-x}\text{Ni}_x\text{Sb}_3$ Alloys," *J. Nanosci. Nanotechnol.*, vol. 8, p. 4003, 2008.
- [27] R. Song, T. Aizawa, and J. Sun, "Synthesis of $\text{Mg}_2\text{Si}_{1-x}\text{Sn}_x$ solid solutions as thermoelectric materials by bulk mechanical alloying and hot pressing," *Materials Science and Engineering: B*, no. 136, p. 111, 2007.
- [28] R. Song, Y. Z. Liu, and T. Aizawa, "Thermoelectric properties of p-type $\text{Mg}_2\text{Si}_{0.6}\text{Ge}_{0.4}$ fabricated by bulk mechanical alloying and hot pressing," *Phys. Status. Solidi RRL*, no. 1, p. 226, 2007.
- [29] G. Joshi, X. Yan, H. Z. Wang, W. S. Liu, G. Chen and Z. F. Ren, "Enhancement in Thermoelectric Figure-Of-Merit of an N-Type Half-Heusler Compound by the Nanocomposite Approach," *Advanced Energy Materials*, vol. 1, pp. 643–647, 2011.
- [30] S. J. Poon, D. Wu, S. Zhu, W. Xie, T. M. Tritt, P. Thomas, and R. Venkatasubramanian, "Half-Heusler phases and nanocomposites as emerging high-ZT thermoelectric materials," *Journal of Materials Research*, vol. 26, no. 22, pp. 2795–2802, Nov. 2011.
- [31] F. J. DiSalvo, "Thermoelectric cooling and power generation," *Science*, vol. 285, no. 6, pp. 703–706, 1999.
- [32] W. Xie, X. Tang, Y. Yan, Q. Zhang, and T. M. Tritt, "Unique nanostructures and enhanced thermoelectric performance of melt-spun BiSbTe alloys," *Applied Physics Letters*, vol. 94, no. 10, 102111, 2009.
- [33] W. Xie, J. He, H. J. Kang, X. Tang, S. Zhu, M. Laver, S. Wang, J. R. D. Copley, C. M. Brown, Q. Zhang, and T. M. Tritt, "Identifying the specific nanostructures responsible for the high thermoelectric performance of $(\text{Bi,Sb})_2\text{Te}_3$ nanocomposites," *Nano letters*, vol. 10, no. 9, pp. 3283–9, Sep. 2010.
- [34] P. Zhang, Z. Wang, H. Chen, H. J. Yu, and L. Zhu, and Z. Y. Jian, *Journal of Electronic Materials*, vol. 39, no. 10, pp. 2251–2254, 2010.
- [35] D. M. Hulbert, A. Anders, D. V. Dudina, J. Andersson, D. Jiang, C. Unuvar, U. Anselmi-Tamburini, E. J. Lavernia, and A. K. Mukherjee, "The absence of plasma in 'spark plasma sintering'," *Journal of Applied Physics*, vol. 104, no. 3, 033305, 2008.

- [36] S. R. Culp, "Complex Half Heusler Phases as High Temperature Thermoelectric Materials," PhD thesis, University of Virginia, 2006.
- [37] W.J.Parker, R.J.Jenkins, C.P.Butler, and G. L. A. Flash, *J.Appl.Phys.*, vol. 32, p. 1679, 1966.
- [38] R.E.Tylor, *Critical evaluation of flash method for measuring thermal diffusivity*, Report PRF. Springfield, Virginia: National Science Technical Information Service, 1973.
- [39] "Molecular Biology," *Molecular Biology*, vol. 6, pp. 7–33, 1975.
- [40] S. R. Culp, J. W. Simonson, S. J. Poon, V. Ponnambalam, J. Edwards, and T. M. Tritt, "(Zr,Hf)Co(Sb,Sn) half-Heusler phases as high-temperature (>700 °C) p-type thermoelectric materials," *Applied Physics Letters*, vol. 93, no. 2, 022105, 2008.
- [41] Y. Kimura, H. Ueno, and Y. Mishima, "Thermoelectric Properties of Directionally Solidified Half-Heusler (M_{0.5}a, M_{0.5}b)NiSn (Ma, Mb = Hf, Zr, Ti) Alloys," *Journal of Electronic Materials*, vol. 38, no. 7, pp. 934–939, Feb. 2009.
- [42] G. D. Mahan and J. O. Sofo, "The best thermoelectric.," *Proceedings of the National Academy of Sciences of the United States of America*, vol. 93, no. 15, pp. 7436–9, Jul. 1996.
- [43] S. Ogut and K.M. Rabe, *Physical Review B*, no. 51, 10443, 1995.
- [44] J. W. Simonson, "Electronic Structure Properties and a Bonding Model of thermoelectric Half Heusler and Boride Phases," PhD thesis, University of Virginia, 2009.
- [45] C. Uher, J. Yang, S. Hu, D. Morelli, and G. Meisner, "Transport properties of pure and doped MNiSn (M= Zr, Hf)," *Physical Review B*, vol. 59, no. 13, pp. 8615–8621, 1999.
- [46] S. J. Poon, *Semiconductors and semimetals*. New York: Academic, 2001, p. 37.
- [47] H. Hohl, A.P. Ramirez, C. Goldmann, and G. Ernst, "Efficient dopants for ZrNiSn-based thermoelectric materials Efficient dopants for ZrNiSn-based thermoelectric materials," *J. Phys.: Condens. Matter*, vol. 11, p. 1697, 1999.
- [48] D. Vashaee and A. Shakouri, "Improved Thermoelectric Power Factor in Metal-Based Superlattices," *Physical Review Letters*, vol. 92, no. 10, 106103, Mar. 2004.
- [49] W. J. Xie, X. Tang, and Q. Zhang "Fast preparation and thermal transport property of TiCoSb based half-Heusler compounds," *Chinese Physics*, vol. 16, no. 11, 2007.

- [50] J. Yang, G.P. Meisner, and L. Chen, "Strain field fluctuation effects on lattice thermal conductivity of ZrNiSn-based thermoelectric compounds," *Applied Physics Letters*, vol. 85, no. 7, p. 1140, 2004.
- [51] C. Yu, T.-J. Zhu, R.-Z. Shi, Y. Zhang, X.-B. Zhao, and J. He, "High-performance half-Heusler thermoelectric materials $\text{Hf}_{1-x}\text{Zr}_x\text{NiSn}_{1-y}\text{Sb}_y$ prepared by levitation melting and spark plasma sintering," *Acta Materialia*, vol. 57, no. 9, pp. 2757–2764, May 2009.
- [52] T. Irie, "Lattice Thermal Conductivity of Disordered Alloys of Ternary Compound Semiconductors $\text{Cu}_2(\text{Sn, Ge})(\text{Se, S})_3(\text{Ag, Pb, Sb})\text{Te}_2$, and $(\text{Ag, Sn, Sb})\text{Te}_2$," *Jpn. J. Appl. Phys.*, vol. 5, p. 854, 1966.
- [53] S. Fan, J. Zhao, Q. Yan, J. Ma, and H. H. Hng, "Influence of Nano-inclusions on Thermoelectric Properties of n-Type Bi_2Te_3 Nanocomposites," *Journal of Electronic Materials*, vol. 40, no. 5, pp. 1018–1023, Jan. 2011.
- [54] S. Johnsen, J. He, and J. Androulakis, "Nanostructures boost the thermoelectric performance of PbS," *Journal of the American Chemical Society*, pp. 3460–3470, 2011.
- [55] X. Yan, W. Liu, H. Wang, S. Chen, J. Shiomi, K. Esfarjani, H. Wang, D. Wang, G. Chen, and Z. Ren, "Stronger phonon scattering by larger differences in atomic mass and size in p-type half-Heuslers $\text{Hf}_{1-x}\text{TixCoSb}_{0.8}\text{Sn}_{0.2}$," *Energy & Environmental Science*, vol. 5, no. 6, p. 7543, 2012.
- [56] W. Xie, A. Weidenkaff, X. Tang, Q. Zhang, J. Poon, and T. Tritt, "Recent Advances in Nanostructured Thermoelectric Half-Heusler Compounds," *Nanomaterials*, vol. 2, no. 4, pp. 379–412, Nov. 2012.
- [57] J. Callaway, "Model for Lattice Thermal Conductivity at Low Temperatures," *Physical Review*, vol. 113, no. 4, 1959.
- [58] J. Wu, W. Shan, and W. Walukiewicz "Band anticrossing in highly mismatched III–V semiconductor alloys," *Semicond. Sci. Technol.*, vol. 17, pp. 860–869, 2002.
- [59] J. H. Lee, J. Wu, and J. C. Grossman, "Enhancing the Thermoelectric Power Factor with Highly Mismatched Isoelectronic Doping," *Physical Review Letters*, vol. 104, no. 1, 016602, Jan. 2010.
- [60] M. Cutler and N.F. Mott, "Observation of Anderson Localization in an Electron Gas," *Physical Review B*, vol. 181, p. 1336, 1969.
- [61] J. W. Simonson, D. Wu, W. J. Xie, T. M. Tritt, and S. J. Poon, "Introduction of resonant states and enhancement of thermoelectric properties in half-Heusler alloys," *Physical Review B*, vol. 83, no. 23, 235211, Jun. 2011.

- [62] J. W. Simonson and S. J. Poon, “Electronic structure of transition metal-doped XNiSn and XCoSb (X = Hf,Zr) phases in the vicinity of the band gap,” *Journal of Physics: Condensed Matter*, vol. 20, no. 25, 255220, Jun. 2008.
- [63] P. Qiu, J. Yang, X. Huang, X. Chen, and L. Chen, “Effect of antisite defects on band structure and thermoelectric performance of ZrNiSn half-Heusler alloys,” *Applied Physics Letters*, vol. 96, no. 15, 152105, 2010.
- [64] B. R. K. Nanda and I. Dasgupta, “Electronic structure and magnetism in doped semiconducting half-Heusler compounds,” *Journal of Physics: Condensed Matter*, vol. 17, no. 33, pp. 5037–5048, Aug. 2005.
- [65] V. A. Romaka, M. G. Shelyapina, Y. K. Gorelenko, D. Fruchart, Y. V. Stadnyk, L. P. Romaka, and V. F. Chekurin, “Special features of conductivity mechanisms in heavily doped n-ZrNiSn intermetallic semiconductors,” *Semiconductors*, vol. 40, no. 6, pp. 655–661, Jun. 2006.
- [66] V.I. Fistul, *Heavily doped Semiconductors*. New York: Plenum, 1969.
- [67] M. S. Dresselhaus, G. Chen, M. Y. Tang, R. G. Yang, H. Lee, D. Z. Wang, Z. F. Ren, J. P. Fleurial, and P. Gogna, “New Directions for Low-Dimensional Thermoelectric Materials,” *Advanced Materials*, vol. 19, no. 8, pp. 1043–1053, Apr. 2007.
- [68] G. Chen and A. Shakouri, *J. Heat Transfer*, vol. 124, no. 242, 2002.
- [69] L. D. Hicks. and M. S. Dresselhaus, “Thermoelectric figure of merit of a one-dimensional conductor,” *Phys .Rev. B*, vol. 47, no. 24, pp. 8–11, 1993.
- [70] T. M. Tritt, *Recent trends in Thermoelectric materials research III, in Semiconductors and Semimetals*. Academic press, 2001.
- [71] R. Venkatasubramanian, E. Siivola, T. Colpitts, and B. O’Quinn, “Thin-film thermoelectric devices with high room-temperature figures of merit.,” *Nature*, vol. 413, no. 6856, pp. 597–602, Oct. 2001.
- [72] T. C. Harman, P. J. Taylor, M. P. Walsh, and B. E. LaForge, “Quantum dot superlattice thermoelectric materials and devices.,” *Science (New York, N.Y.)*, vol. 297, no. 5590, pp. 2229–32, Sep. 2002.
- [73] A. I. Hochbaum, R. Chen, R. D. Delgado, W. Liang, E. C. Garnett, M. Najarian, A. Majumdar, and P. Yang, “Enhanced thermoelectric performance of rough silicon nanowires.,” *Nature*, vol. 451, no. 7175, pp. 163–7, Jan. 2008.

- [74] A.I. Boukai, Y. Bunimovich, J. Tahir-Kheli, J.K. Yu, W.A. Goddard, and J. R. Heath, "Silicon nanowires as efficient thermoelectric materials," *Nature*, vol. 451, no. 7175, pp. 168–71, Jan. 2008.
- [75] W. Kim, J. Zide, A. Gossard, and D. Klenov, "Thermal conductivity reduction and thermoelectric figure of merit increase by embedding nanoparticles in crystalline semiconductors," *Physical Review Letters*, vol. 96, no. 4, 045901, Feb. 2006.
- [76] J. M. O. Zide, J.-H. Bahk, R. Singh, M. Zebarjadi, G. Zeng, H. Lu, J. P. Feser, D. Xu, S. L. Singer, Z. X. Bian, a. Majumdar, J. E. Bowers, a. Shakouri, and a. C. Gossard, "High efficiency semimetal/semiconductor nanocomposite thermoelectric materials," *Journal of Applied Physics*, vol. 108, no. 12, 123702, 2010.
- [77] A. Popescu and L. M. Woods, "Enhanced thermoelectricity in composites by electronic structure modifications and nanostructuring," *Applied Physics Letters*, vol. 97, no. 5, 052102, 2010.
- [78] B. Moyzhes and V. Nemchinsky, *11th Int. Conf. thermoelectrics*. Texas: University of Texas press, 1992, p. 232.
- [79] Y.Nishio and T.Hirano, "Discussion of barrier heights and separation on Seebeck.pdf," *Jpn. J. Appl. Phys.*, vol. 36, pp. 170–174, 1997.
- [80] K. Kishimoto, K. Yamamoto, and T. Koyanagi, "Influences of Potential Barrier Scattering on the Thermoelectric Properties of Sintered n-Type PbTe with a Small Grain Size," *Japanese Journal of Applied Physics*, vol. 42, no. Part 1, No. 2A, pp. 501–508, Feb. 2003.
- [81] N. Neophytou, X. Zianni, M. Ferri, a. Roncaglia, G. F. Cerofolini, and D. Narducci, "Nanograin Effects on the Thermoelectric Properties of Poly-Si Nanowires," *Journal of Electronic Materials*, Feb. 2013.
- [82] B. Moyzhes and V. Nemchinsky, "Thermoelectric figure of merit of metal–semiconductor barrier structure based on energy relaxation length," *Applied Physics Letters*, vol. 73, no. 13, p. 1895, 1998.
- [83] Y. Nishio and T. Hirano, "Thermoelectric properties of multi-layered system," *ICT 98. XVII International Conference*, pp. 111–114, 1998.
- [84] S. D. Peacor, R.A. Richardson, F. Nori, and C. Uher, "Theoretical analysis of the thermal conductivity of YBa₂Cu₃O_{7-x} single crystals," *Phys. Rev. B.*, vol. 44, p. 9508, 1991.
- [85] L. D. Chen, X. Y. Huang, M. Zhou, X. Shi, and W. B. Zhang, "The high temperature thermoelectric performances of Zr[0.5]Hf[0.5]Ni[0.8]Pd[0.2]Sn[0.99]Sb[0.01] alloy with nanophase inclusions," *Journal of Applied Physics*, vol. 99, no. 6, 064305, 2006.

- [86] J. L. Mi, X.B. Zhao, and T.J. Zhu, "Thermoelectric properties of nanostructured skutterudite-related compounds," *2007 26th International Conference on Thermoelectrics*, vol. 2, pp. 16–20, Jun. 2007.
- [87] P. Klemens, "The thermal conductivity of dielectric solids at low temperatures (theoretical)," *Proceedings of the Royal Society A*, vol. 208, no. 1092, pp. 108–133, Aug. 1951.
- [88] N. Mingo, D. Hauser, N.P. Kobayashi, M. Plissonnier, and A. Shakouri, "' Nanoparticle-in-Alloy ' Approach to Efficient Thermoelectrics : Silicides in SiGe," 2009.
- [89] C. Vining and W. Laskow and J. Hanson and R. Van der Beck and P. Gorsuch, "Thermoelectric properties of pressure - sintered Si_{0.8}Ge_{0.2} thermoelectric alloys," *J. Appl. Phys.*, vol. 69, 4333, 1990.
- [90] J. I. Langford and A. J. C. Wilson, "Scherrer after Sixty Years: A Survey and Some New Results in the Determination of Crystallite Size," *J. Appl. Cryst.*, vol. 11, pp. 102–113, 1978.
- [91] P. Reiss, M. Protière, and L. Li, "Core/Shell semiconductor nanocrystals," *Small (Weinheim an der Bergstrasse, Germany)*, vol. 5, no. 2, pp. 154–68, Feb. 2009.
- [92] M. Bruchez Jr., "Semiconductor Nanocrystals as Fluorescent Biological Labels," *Science*, vol. 281, no. 5385, pp. 2013–2016, Sep. 1998.
- [93] A. Makhal, H. Yan, P. Lemmens, and S. K. Pal, "Light Harvesting Semiconductor Core–Shell Nanocrystals: Ultrafast Charge Transport Dynamics of CdSe–ZnS Quantum Dots," *The Journal of Physical Chemistry C*, vol. 114, no. 1, pp. 627–632, Jan. 2010.
- [94] R. Yang, G. Chen, and M. S. Dresselhaus, "Thermal conductivity modeling of core-shell and tubular nanowires," *Nano letters*, vol. 5, no. 6, pp. 1111–5, Jun. 2005.
- [95] G. Zhang, W. Wang, and X. Li, "Enhanced Thermoelectric Properties of Core/Shell Heterostructure Nanowire Composites," *Advanced Materials*, vol. 20, no. 19, pp. 3654–3656, Oct. 2008.
- [96] C. J. Murphy and J. L. Coffey, "Quantum Dots: A Primer," *Quantum Dots: A Primer. Appl. Spectrosc.*, vol. 56, p. 16A–27A, 2002.
- [97] R. Yang and G. Chen, "Thermal conductivity modeling of periodic two-dimensional nanocomposites," *Physical Review B*, vol. 69, no. 19, 195316, May 2004.
- [98] C. Dames, "Theoretical phonon thermal conductivity of Si/Ge superlattice nanowires," *Journal of Applied Physics*, vol. 95, no. 2, p. 682, 2004.

- [99] R. Yang, G. Chen, M. Laroche, and Y. Taur, "Simulation of Nanoscale Multidimensional Transient Heat Conduction Problems Using Ballistic-Diffusive Equations and Phonon Boltzmann Equation," *Journal of Heat Transfer*, vol. 127, no. 3, p. 298, 2005.
- [100] R. Yang, G. Chen, and M. Dresselhaus, "Thermal conductivity of simple and tubular nanowire composites in the longitudinal direction," *Physical Review B*, vol. 72, no. 12, 125418, Sep. 2005.
- [101] W. Kim, S. Singer, A. Majumdar, and J. Zide, "Reducing thermal conductivity of crystalline solids at high temperature using embedded nanostructures," *Nano. Lett.*, pp. 6–8, 2008.
- [102] M. Jeng, R. Yang, D. Song, and G. Chen, "Modeling the thermal conductivity and phonon transport in nanoparticle composites using Monte Carlo simulation," *Journal of Heat Transfer*, vol. 130, no. 4, 042410, 2008.
- [103] S. K. Bux, R. G. Blair, P. K. Gogna, H. Lee, G. Chen, M. S. Dresselhaus, R. B. Kaner, and J.-P. Fleurial, "Nanostructured Bulk Silicon as an Effective Thermoelectric Material," *Advanced Functional Materials*, vol. 19, no. 15, pp. 2445–2452, Aug. 2009.
- [104] C. W. Nan, "Effective medium theory of piezoelectric composites," *J.Appl.Phys.*, vol. 76, p. 1155, 1994.
- [105] C. W. Nan, R. Birringer, D. R. Clarke, and H. Gleiter, "Effective thermal conductivity of particulate composites with interfacial thermal resistance," *Journal of Applied Physics*, vol. 81, no. 10, p. 6692, 1997.
- [106] A. Minnich and G. Chen, "Modified effective medium formulation for the thermal conductivity of nanocomposites," *Applied Physics Letters*, vol. 91, no. 7, 073105, 2007.
- [107] S. J. Poon and K. Limtragool, "Nanostructure model of thermal conductivity for high thermoelectric performance," *Journal of Applied Physics*, vol. 110, no. 11, 114306, 2011.
- [108] S. Poon, A. Petersen, and D. Wu, "Thermal conductivity of core-shell nanocomposites for enhancing thermoelectric performance," *Applied Physics Letters*, vol. 102, no. 17, 173110, 2013.
- [109] Z. Zamanipour and D. Vashaee, "Comparison of thermoelectric properties of p-type nanostructured bulk $\text{Si}_{0.8}\text{Ge}_{0.2}$ alloy with $\text{Si}_{0.8}\text{Ge}_{0.2}$ composites embedded with CrSi_2 nano-inclusions," *Journal of Applied Physics*, vol. 112, no. 9, 093714, 2012.
- [110] W. Kim and A. Majumdar, "Phonon scattering cross section of polydispersed spherical nanoparticles," *Journal of applied physics*, vol. 99, no. 8, 084306, 2006.

- [111] J. Androulakis, I. Todorov, J. He, D. Chung, V. Dravid, and M. Kanatzidis, "Thermoelectrics from Abundant Chemical Elements : High-Performance Nanostructured PbSe-PbS," pp. 10920–10927, 2011.
- [112] D. A. G. Bruggeman, "Berechnung verschiedener physikalischer Konstanten von heterogenen Substanzen. I. Dielektrizitätskonstanten und Leitfähigkeiten der Mischkörper aus isotropen Substanzen," *Ann. Phys.*, vol. 24, p. 636, 1935.
- [113] G. Chen, "Thermal conductivity and ballistic-phonon transport in the cross-plane direction of superlattices," *Physical Review B*, vol. 57, no. 23, pp. 958–973, 1998.
- [114] O. L. Anderson, "A simplified method for calculating the debye temperature from elastic constants," *J. Phys. Chem. Solids.*, vol. 24, pp. 909–917, 1963.
- [115] L. Jin, Q. Yu, A. Rauf and C. Zhou, "Elastic, electronic and thermal properties of YSZ from first principles," *solid state sci.*, vol. 14, p. 106, 2012.
- [116] C. Degueldre, P. Tissot, H. Lartigue and M. Pouchon "Specific heat capacity and Debye temperature of zirconia and its solid solution," *Thermochim. Acta.*, vol. 403, p. 267, 2003.
- [117] K. Schlichting, N. Padture, and P. Klemens, "Thermal conductivity of dense and porous yttria-stabilized zirconia," *Journal of materials science*, vol. 6, pp. 3003–3010, 2001.
- [118] P. N. Alboni, X. Ji, J. He, and N. Gothard, "Synthesis and Thermoelectric Properties of 'Nano-Engineered' CoSb₃ Skutterudite Materials," *Journal of electronic materials*, vol. 36, no. 7, pp. 711–715, Jun. 2007.
- [119] S. Poon and A. Petersen, "Effective medium approach to thermal conductivity: applying to core-shell nanocomposites," *Emerging Materials Research*, pp. 1–6, 2012.
- [120] C. F. Bohren and D. R. Huffman, *Absorption and Scattering of Light by Small Particles*. New York: Wiley, 1998.
- [121] H. C. van de Hulst, *Light Scattering by Small Particles*. New York: Dover, 1981.
- [122] C. F. Ying and R. Truell, "Scattering of a Plane Longitudinal Wave by a Spherical Obstacle in an Isotropically Elastic Solid," *Journal of Applied Physics*, vol. 27, no. 9, p. 1086, 1956.
- [123] N. G. Einspruch, E. J. Witterholt, and R. Truell, "Scattering of a Plane Transverse Wave by a Spherical Obstacle in an Elastic Medium," *Journal of Applied Physics*, vol. 31, no. 5, p. 806, 1960.

- [124] A. Majumdar, "Microscale Heat Conduction in lelectnc Thin Films," *ASME J. Heat Transfer*, vol. 115, no. 7, 1993.
- [125] H. Li, X. Tang and Q. Zhang, *J. Electronic Materials*, vol. 38, no. 7, 2009.
- [126] Y. Lan, A. J. Minnich, G. Chen, and Z. Ren, "Enhancement of Thermoelectric Figure-of-Merit by a Bulk Nanostructuring Approach," *Advanced Functional Materials*, vol. 20, no. 3, pp. 357–376, Feb. 2010.
- [127] H. Lee, MS thesis, MIT, 2005.
- [128] Z. Wang, J. E. Alaniz, W. Jang, J. E. Garay, and C. Dames, "Thermal Conductivity of Nanocrystalline Silicon : Importance of Grain Size and Frequency-Dependent Mean Free Paths," pp. 2206–2213, 2011.
- [129] Y. Pei and Y. Liu, "Electrical and thermal transport properties of Pb-based chalcogenides: PbTe, PbSe, and PbS," *Journal of Alloys and Compounds*, vol. 514, pp. 40–44, 2012.
- [130] M. A. S. Boff, G. L. F. Fraga, D. E. Brand ão, A. A. Gomes, and T. A. Grandi, "Specific Heat of Ni₂TSn (T = Ti, Zr, Hf) Heusler Compounds," *Physica Status Solidi (a)*, vol. 154, no. 2, pp. 549–552, Apr. 1996.
- [131] H. Özişik, K. Çolakoğlu, and H. B. Özişik, "ab-initio first principles calculations on Half-Heusler NiYSn(Y=Zr,Hf) compounds part 1: structural, lattice dynamical and thermo dynamic properties," *Fizika*, vol. 16, no. 2, pp. 154–157, 2010.
- [132] H. Muta, T. Kanemitsu, K. Kurosaki, and S. Yamanaka, "Substitution Effect on Thermoelectric Properties of ZrNiSn Based Half-Heusler Compounds," vol. 47, no. 6, pp. 1453–1457, 2006.
- [133] W. Jeitschko, *Metall. Trans. A*, vol. 1, p. 3179, 1970.
- [134] S. N. Girard, J. He, C. Li, S. Moses, G. Wang, C. Uher, V. P. Dravid, and M. G. Kanatzidis, "In Situ Nanostructure Generation and Evolution within a Bulk Thermoelectric Conductivity," *Nano. Lett.*, vol. 10, pp. 2825–2831, 2010.
- [135] S. N. Girard, K. Schmidt-Rohr, T. C. Chasapi, E. Hatzikraniotis, B. Njelic, E. M. Levin, A. Rawal, K. M. Paraskevopoulos and M. G. Kanatzidis, "Analysis of Phase Separation in High Performance PbTe–PbS Thermoelectric Materials," *Advanced Functional Materials Functional Materials*, no. 23, pp. 747–757, 2013.
- [136] B. J. He, S. N. Girard, M. G. Kanatzidis, and P. Dravid, "Microstructure-Lattice Thermal Conductivity Thermoelectric Materials," *Advanced Functional Materials*, vol. 20, pp. 764–772, 2010.

- [137] J. P. A. Makongo, D. K. Misra, J. R. Salvador, N. J. Takas, G. Wang, M. R. Shabetai, A. Pant, P. Paudel, C. Uher, K. L. Stokes, and P. F. P. Poudeu, "Thermal and electronic charge transport in bulk nanostructured $Zr_{0.25}Hf_{0.75}NiSn$ composites with full-Heusler inclusions," *Journal of Solid State Chemistry*, vol. 184, no. 11, pp. 2948–2960, Nov. 2011.
- [138] C. S. Birkel, J. E. Douglas, B. R. Lettiere, G. Seward, N. Verma, Y. Zhang, and T. M. Pollock, "half-Heusler $TiNiSn$ through inclusion of a second," pp. 6990–6997, 2013.
- [139] Y. Wang Chai and Y. Kimura, "Nanosized precipitates in half-Heusler $TiNiSn$ alloy," *Applied Physics Letters*, vol. 100, no. 3, 033114, 2012.
- [140] A. Minnich and M. Dresselhaus, "Bulk nanostructured thermoelectric materials: current research and future prospects," *Energy & Environmental Science*, vol. 2, no. 5, p. 466, 2009.